

Measuring MRP1 Transport Activity in SECM Feedback Mode

Sebastian Amland Skånvik

Department of Chemistry, McGill University

Montreal, Canada

June 2019

A thesis submitted to McGill University
in partial fulfillment of the requirements of the degree of
Master of Science

© Sebastian Amland Skånvik, 2019. All rights reserved.

Table of Contents

List of Figures	v
List of Tables	vii
List of Equations	viii
Abstract	x
Resumé	xii
Abbreviations	xiv
Symbols	xvi
Author Contributions	xviii
Acknowledgments	xix
1 Introduction	1
1.1 The Role of MRP1 in Multidrug Resistance	1
1.2 Measuring MRP1 Transport	5
1.2.1 Vesicles	5
1.2.2 Live Cells	6
1.2.3 GSH as an MRP1 Substrate	6
1.3 Scanning Electrochemical Microscopy	7
1.4 SECM Feedback Mode	10
1.4.1 Negative Feedback	11
1.4.2 Positive Feedback	11
1.4.3 Intermediate Kinetics	12

1.5	Finite Element Modeling	12
1.6	Studies of Multidrug Resistance by SECM	14
1.7	Project Aims	17
2	Evaluating the Performance of a Dual Redox Mediator Approach in SECM	
	Feedback Mode: Fitting Over Flat and Curved Substrates	19
2.1	Contributions	19
2.2	Introduction	20
2.3	Experimental	23
2.4	Single-Point L -Fitting over Flat Substrates	25
2.5	κ -Fitting over Flat Substrates	27
2.6	Single-Point κ -Fitting over Flat Substrates	30
2.7	Applying the Single-Point κ -Fitting to Line Scans	31
2.8	Single-Point L -Fitting over Curved Substrates	33
2.9	κ -Fitting over Curved Substrates	34
2.10	Single-Point κ -Fitting over Curved Substrates	35
2.11	Evaluation of Extraction Methods and Simulations	37
2.12	Conclusions	39
2.13	Appendix	40
	2.13.1 Single-Point L -Fitting over Flat Substrates	40
	2.13.2 κ -Fitting over Flat Substrates	41
	2.13.3 κ -Fitting over Curved Substrates	42
	2.13.4 Single-Point κ -Fitting over Curved Substrates	43
3	Quantifying MRP1 Transport Activity of HEK293 and HEKMRP1 Cells	45
3.1	Contributions	45
3.2	Introduction	46
3.3	Experimental	48

3.3.1	Western Blotting	48
3.3.2	GSH Quantification	49
3.3.3	SECM Approach Curves Over Cell Layer	50
3.3.4	Electrochemical Measurements	51
3.4	Effects of MRP1 Overexpression	51
3.5	Applying the Feedback Method	52
3.6	Evaluating the Feedback Method	56
3.7	The EC' Model for GSH Detection with FcMeOH	57
3.8	Regeneration of Other Ferrocene Derivatives	59
3.9	Applying the Chronoamperometry Method	60
3.10	Conclusions	61
3.11	Appendix	63
3.11.1	Light Sensitivity of FcCOOH	63
3.11.2	Electrode Fouling in the Presence of GSH	64
3.11.3	Current Stability in SECM Imaging	65
3.11.4	Western Blotting Solutions	66
4	Conclusions and Future Work	67
4.1	Summary and Contributions to Original Knowledge	67
4.2	Future Works	68
	References	86

List of Figures

1.1	Structure of MRP1	2
1.2	Physiological Relevant Reactions of GSH	3
1.3	Transport Mechanisms of MRP1	4
1.4	Schematic of SECM Instrumentation.	8
1.5	Overview of Electrochemistry at the μm Scale.	9
1.6	Overview of SECM Feedback Mode.	10
1.7	Discretization and Numerical Simulations.	14
1.8	SECM Study of Thiodione Efflux.	15
1.9	Effect of FcMeOH on Intracellular GSH Levels	16
1.10	SECM Imaging and Decoupling of Feedback Responses for HeLa and HeLa-R Cells.	17
2.1	Overview of Tip-to-Substrate Distance Calibration in SECM.	21
2.2	Mechanisms of Dual Mediator Systems.	22
2.3	Simulation Variables and Geometries.	24
2.4	L -fitting over Flat Substrates.	27
2.5	Approach Curve Fitting over Flat Substrates.	29
2.6	Single-Point κ -Fitting over Flat Substrates.	31
2.7	κ -Fitting of Line Scans.	32
2.8	L -Fitting over Curved Substrates.	34
2.9	κ -Fitting over Curved Substrates.	35

2.10	Single-Point κ -Fitting over Curved Substrates.	36
2.11	Evaluation of Fitting Procedures.	37
2.12	Single-Point κ -Fitting over Curved Substrates with L_{true}	43
3.1	Effects of MRP1 Overexpression	52
3.2	Activity and Topography Fitting of SECM Images.	54
3.3	Examples of High Variance in κ	55
3.4	Evaluation of the Feedback Method.	56
3.5	CVs with and Without GSH.	57
3.6	GSH Calibration Curve with Chronoamperometry.	58
3.7	Screening of Ferrocene Derivatives for GSH Oxidation.	59
3.8	Light Sensitivity of FcCOOH.	63
3.9	Electrode Fouling in the Presence of GSH	64
3.10	Current Stability in SECM Imaging.	65
4.1	Au/SiO ₂ Substrates.	69
4.2	Constant Flux Model.	71

List of Tables

2.1	Simulation Parameters.	25
2.2	Single-Point κ -Fitting over Flat Substrates.	31
2.3	Single-Point L -Fitting over Flat Substrates.	40
2.4	κ -Fitting over Flat Substrates.	41
2.5	κ -Fitting over Curved Substrates.	42
3.1	Response Factors Obtained with Chronoamperometry Method.	61

List of Equations

Equation 1.1	Steady-State Current at a Microelectrode in Bulk Solution.....	9
Equation 1.2	Approximation of β -Coefficient.....	9
Equation 1.3	Negative Feedback Analytical Approximation.....	11
Equation 1.4	Positive Feedback Analytical Approximation.....	11
Equation 1.5	Approximation of α -Coefficient.....	12
Equation 1.6	Intermediate Kinetics Analytical Approximation.....	12
Equation 1.7	Fick's Second Law of Mass Transport.....	13
Equation 1.8	Fick's Second Law of Mass Transport, Discretized.....	13
Equation 1.9	Boundary Condition at the Electrode.....	13
Equation 1.10	Simulated Current at Electrode.....	13
Equation 1.11	Boundary Condition at Substrate.....	13
Equation 2.1	Reaction Occurring at the Electrode.....	23
Equation 2.2	Vector Notation of Approach Curves.....	26
Equation 2.3	Single-Point L -Fitting.....	26
Equation 2.4	Definition of Error in Tip-to-Substrate Distance.....	26
Equation 2.5	Definition of Error in κ	27
Equation 2.6	Single-Mediator k -Fitting.....	28
Equation 2.7	Dual-Mediator k -Fitting.....	28
Equation 2.8	Single-Mediator Single-Point k -Fitting.....	30

Equation 2.9	Dual-Mediator Single-Point k -Fitting.....	30
Equation 2.10	Definition of Current Error.....	38
Equation 3.1	Description of the EC' Mechanism.....	47
Equation 3.2	EC' Mechanism for the Oxidation of GSH by $FcMeOH^+$	48
Equation 3.3	Definition of Response Factor.....	60
Equation 4.1	Relationship Between Constant Flux and Concentration.....	70
Equation 4.2	Complementary Error Function	70
Equation 4.3	Hill Equation	70

Abstract

Multidrug resistance can impede chemotherapeutic treatment and reduce cancer patient survival rates. Active transport of drugs out of cancerous cells is one way cancer cells protect themselves. Multidrug resistance-associated protein 1 (MRP1) is a transmembrane transporter that is expressed in most tissues. Its overexpression in cancerous cells can contribute to this detrimental drug efflux and measuring its transport activity remains challenging. Sound evaluation of MRP1 transport activity can improve the assessment of multidrug resistance modulators in living systems. Here, scanning electrochemical microscopy (SECM) is used to tackle this problem due to its noninvasiveness and high sensitivity.

This thesis discusses the validity of previously reported SECM feedback mode analytical approximations when negative and intermediate feedback behaviours are deconvoluted. Experimentally, this is the case when a reactive feature is surrounded by an insulating region or when a dual-mediator system is used, which is when one mediator probes substrate reactivity and the other probes tip-to-substrate distance. Dual-mediator systems are advantageous as they eliminate the need of more complicated experimental setups. Alternatively, the microelectrode can be intentionally crashed into the substrate to calibrate tip-to-substrate distance. However, this is not always possible for biological or fragile samples. Furthermore, dual-mediator systems can be used to fit SECM parameters in the horizontal plane from current images as opposed to standard approach curve experiments. The extraction of kinetic

parameters in the horizontal plane requires fitting a series of single point to the analytical approximations.

The validity of the analytical approximations while using a dual-mediator system is studied using numerically simulated reference data. For low RG s, a geometric electrode parameter, the dual-mediator method outperforms fitting to the true tip-to-substrate distance, for entire approach curves. The accuracy of the single-point fitting was found to be excellent for small to moderate tip-to-substrate distances over flat substrates. Accurate kinetic fitting is also possible for curved substrates, albeit with a smaller range of substrate reactivity. A dual-mediator system was applied HEK293 and HEKMRP1 cells to assess MRP1 transport activity.

Resumé

La multi-résistance peut entraver le traitement chimiothérapeutique et réduire les taux de survie des patients atteints de cancer. Le transport actif des médicaments hors des cellules cancéreuses est un moyen pour ces cellules de se protéger. MRP1 est l'un des contributeurs à cet efflux de médicament préjudiciable. Mesurer son activité de transport reste difficile. Une meilleure évaluation de l'activité de transport de MRP1 peut améliorer l'évaluation des modulateurs de la résistance multiple aux médicaments dans les systèmes vivants. Ici, la microscopie ' electrochimique ' a balayage (SECM) est utilisée pour résoudre ce problème en raison de son caractère non invasif et de sa grande sensibilité.

Cette thèse discute de la validité des approximations analytiques SECM précédemment rapportées lorsque les comportements de rétroaction négatifs et intermédiaires sont découplés. Expérimentalement, c'est le cas lorsqu'une caractéristique réactive est entourée d'une région isolante ou lorsqu'un système à double médiateur est utilisé, c'est-à-dire lorsqu'un médiateur sonde la réactivité de surface et l'autre sonde la distance de la pointe par rapport au substrat. Ces systèmes à double médiateurs sont avantageux car ils éliminent le besoin de trouver la distance pointe-substrat par d'autres moyens, ce qui nécessite des configurations expérimentales plus complexes. Alternativement, la microélectrode peut être mise en contact avec le substrat pour calibrer la distance pointe-substrat, ce qui n'est pas toujours possible pour des échantillons biologiques ou fragiles. De plus, les systèmes à double médiateur peuvent être utilisés pour ajuster les paramètres SECM dans le plan horizontal, par opposition

aux expériences de courbe d'approche standard. L'ajustement d'une série de points uniques aux approximations analytiques est alors requis.

La validité de l'utilisation des approximations analytiques est étudiée à l'aide de données de référence simulées numériquement. Pour des faibles RG , un paramètre d'électrode géométrique, la méthode à double médiateurs est plus performante que l'adaptation à la distance réelle entre la pointe et le substrat lors de l'ajustement des courbes d'approche. Pour les substrats plats, la précision de l'ajustement en un point s'est révélée excellente pour des distances pointe-substrat faibles à modérées. Un ajustement cinétique précis est également possible pour les substrats incurvés, mais avec une fenêtre de réactivité plus petite. Un système à double médiateurs a été appliqué aux cellules HEK293 et HEKMRP1 pour évaluer l'activité de transport de la protéine 1 associée à la multi-résistance aux médicaments.

Abbreviations

ABC-transporter	ATP-Binding Cassette Transporter
AC	Alternating Current
AFM	Atomic Force Microscopy
ATP	Adenosine Triphosphate
BCA	Bicinchoninic Acid
BCRP	Breast Cancer Resistance Protein
BSA	Bovine Serum Albumin
CMFDA	5-Chloromethylfluorescein Diacetate
CV	Cyclic Voltammogram
D	Dimension
DNA	Deoxyribonucleic Acid
FEM	Finite Element Modeling
GAPDH	Glyceraldehyde 3-Phosphate Dehydrogenase
GSH	Glutathione
GSSG	Glutathione Disulfide
HEK	Human Embryonic Kidney
IC	Intermittent Contact
LSF	Least Squares Fit
MDR	Multidrug Resistance
MRP	Multidrug Resistance-Associated Protein

MSD	Membrane Spanning Domain
NBD	Nucleotide Binding Domain
mRNA	Messenger Ribonucleic Acid
PBS	Phosphate-Buffered Saline
P-gp	P-Glycoprotein 1
R	Reduced Form of Redox Mediator
Rt	Room Temperature
Ruhex	Hexaammineruthenium(III) Chloride
SECM	Scanning Electrochemical Microscopy
O	Oxidized Form of Redox Mediator

Symbols

Symbol	Explanation	Unit(s)
α	Geometric Coefficient in SECM Feedback Mode Analytical Approximations	—
β	Geometric Electrode Coefficient	—
κ	Normalized Heterogeneous Kinetic Constant	—
a	Radius of the Active Area of a Disk Microelectrode	m
A	Surface Area	m ²
C	Concentration	mol m ⁻³
C^*	Concentration in Bulk Solution	mol m ⁻³
d	Tip-to-Substrate Distance	m
D_R	Diffusion Coefficient of R	m ² s ⁻¹
f	Mass Transport Flux	mol m ⁻² s ⁻¹
F	Faraday's Constant	C mol ⁻¹
h	Height	m
H	Normalized Height	m
i	Current Recorded at a Microelectrode	A
IC_{50}	Concentration Which Reduces Response by 50%	—
i_∞	Steady-State Current at a Microelectrode in Bulk Solution	A
k	Heterogeneous Kinetic Constant	m s ⁻¹
L	Normalized Tip-to-Substrate Distance	—
L_0	Zero Tip-to-Substrate Distance	—
L_{err}	Normalized Tip-to-Substrate Distance Error	—

n	Sample Size	—
z	Stoichiometric Coefficient of the Electron	—
Ni	Normalized Current at a Microelectrode	—
Ni_{app}	Approximated Normalized Current at a Microelectrode	—
Ni_{sim}	Simulated Normalized Current at a Microelectrode	—
Ni^{con}	Normalized Current Over a Conductor	—
Ni^{ins}	Normalized Current Over an Insulator	—
r	Tip Radius of the Insulating Sheath of a Disk Microelectrode	m
R_z	Radius of Electrolyte Solution in 2D-Axisymmetric Simulation	m
R_f	Response Factor	—
RG	Ratio of Glass to Active Radius of a Microelectrode	—
t	Time	s
w	Width	m
W	Normalized Width	—

Author Contributions

All presented work was supervised by Professor Janine Mauzeroll.

Chapter 1

Sebastian Skånvik (SS) performed the literature search and wrote the chapter.

Chapter 2

SS wrote the chapter except for the section related to simulation meshing, which was written by Lise Stephens (LS). All figures were generated by the author except Figure 1.3B and C), which was generated by LS. The simulations were carried out by LS. All data treatment/analysis was performed by SS.

Chapter 3

Chapter 3 was written by SS. Zeonor substrates were fabricated by Matthias Geissler (MG). Experimental data was acquired by SS, with the exception of the data presented in Figure 3.5C, which was acquired by Nicholas Payne (NP) and SS. Data was treated by SS.

Acknowledgments

I would first and foremost like to thank Janine Mauzeroll for her excellent supervision, support and for introducing me to the beauty of electrochemistry. I will benefit from everything you have taught me for the rest of my career. I am also grateful to have such a supportive and engaged collaborator, Matthias Geissler. The work in this thesis would not have been possible without you.

I'm very glad to have worked in a lab with such skilled and motivated people. You have all really made an impact on my stay at McGill. I would firstly like to thank Lisa for being a great colleague and friend. You create such a positive work environment and you are mostly constructive in our daily scientific debates; no, the answer is not always 42! I would also like to thank Jeremy for creating a good atmosphere in the office. Nick, thank you for always being there to talk about research and for everything you have taught me. It is a lot. I would like to thank Isabelle for all your help the cell work and flow cytometry experiments. Thank you Samantha for proofreading my thesis and for helping me stay motivated during the writing of this thesis.

I would also like to thank my family and friends, in Montreal and Norway, for their love and encouragement.

This page is intentionally left blank

Chapter 1

Introduction

1.1 The Role of MRP1 in Multidrug Resistance

Multidrug resistance (MDR) occurs when cancer cells exhibit resistance towards chemotherapeutic treatment. Three major mechanisms for multidrug resistance have been identified: reduced drug uptake, lowered drug efficacy, and increased drug efflux.¹ Active transport of hydrophilic compounds into cells can decrease, *e.g.* cisplatin.^{2,3} For intracellular drugs, several mechanisms reduce their efficacy, including cell cycle changes, upregulated DNA repair and increased drug metabolism.^{1,4} The intracellular drug concentration is reduced by enhanced efflux via ATP-binding cassette (ABC)-transporters^{5,6} such as P-glycoprotein 1 (P-gp),⁷ breast cancer resistance protein (BCRP)⁸ and the multidrug resistance-associated protein (MRP) family member, MRP1.⁹

MRP1 is a 190kD transmembrane transporter encoded by the ABCC1 gene. It was first cloned in 1992 from the doxorubicin-selected lung cancer cell line, H69AR,¹⁰ a multidrug resistant cell line that does not overexpress P-gp. MRP1 confers resistance to doxorubicin, danorubicin, epirubicin, mitixantrone, flutamide, and methotrexate.¹¹ MRP1 has three membrane spanning domains (MSDs) for substrate binding and two nucleotide binding domains

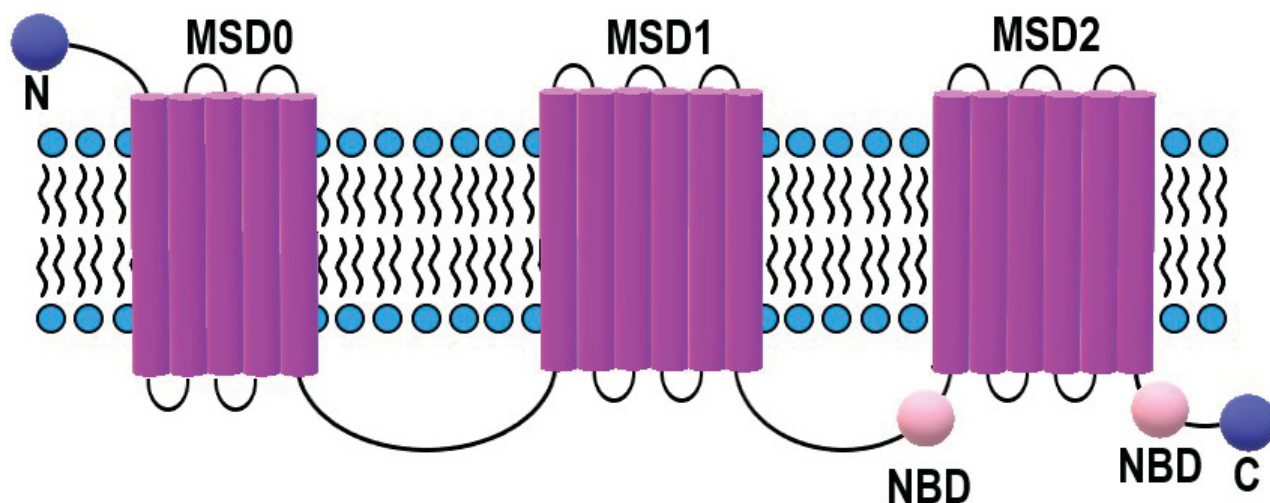


Figure 1.1: Scheme of the structure of MRP1. N and C denotes N- and C-terminus.

(NBDs, Figure 1.1).¹² Substrate binding to the MSD produces a conformational change that enables the two NBDs to dimerize and hydrolyze ATP, which expels the substrate to the extracellular environment. The broad substrate scope of MRP1 stems from multiple binding configurations for both hydrophilic and hydrophobic substrate moieties. Furthermore, rearrangement at the binding site further aid the binding of diverse substrates.¹³ MRP1 protects critical sites in the body from xenobiotics (*e.g.* the blood-cerebrospinal fluid and blood-placental barrier). *ABBC1(-/-)* knock-out mice show hypersensitivity to etoposide (a good MRP1 substrate) These mice also show reduced inflammatory response¹⁴, although the role of MRP1 in inflammation remains unclear, as discussed in Section 1.2.

In contrast to P-gp and BCRP, MRP1-mediated efflux has a complicated relationship to glutathione (GSH). GSH is the most abundant intracellular non-protein thiol. It is present in concentrations ranging from 0.5-10 mM and is present in both the cytosol and organelles.¹⁵ It is a tripeptide composed of glutamate, cystein and glycin, where the glutamate and cystein is bound by a γ linkage. GSH serves many physiological roles. Arguably, it is most famous for its antioxidative properties that protects cells from oxidative stress by sacrificially being oxidized to GSSG (Figure 1.2A). The GSH/GSSG-ratio is consequently indicative of

oxidative stress. GSH also serves as a first step in the detoxification of xenobiotics through its conjugation. For instance, conjugation to menadione yielding thiodione. This process can be catalyzed by glutathione transferases or occur spontaneously¹⁶ (Figure 1.2B). GSH chelates to heavy metals like cadmium as the first step its detoxification process¹⁷ (Figure 1.2C).

The different transport mechanisms of MRP1 are shown in Figure 1.3. For instance, conjugation to GSH is sometimes necessary for transport, some compounds are only transported in the presence of GSH, and others are co-transported with GSH¹⁸ (Figure 1.3). The mechanistic explanations for the varying transport mechanisms are not clear. However, the stimulation of release of GSH is essential to this thesis as it is the mechanism for the measurements of

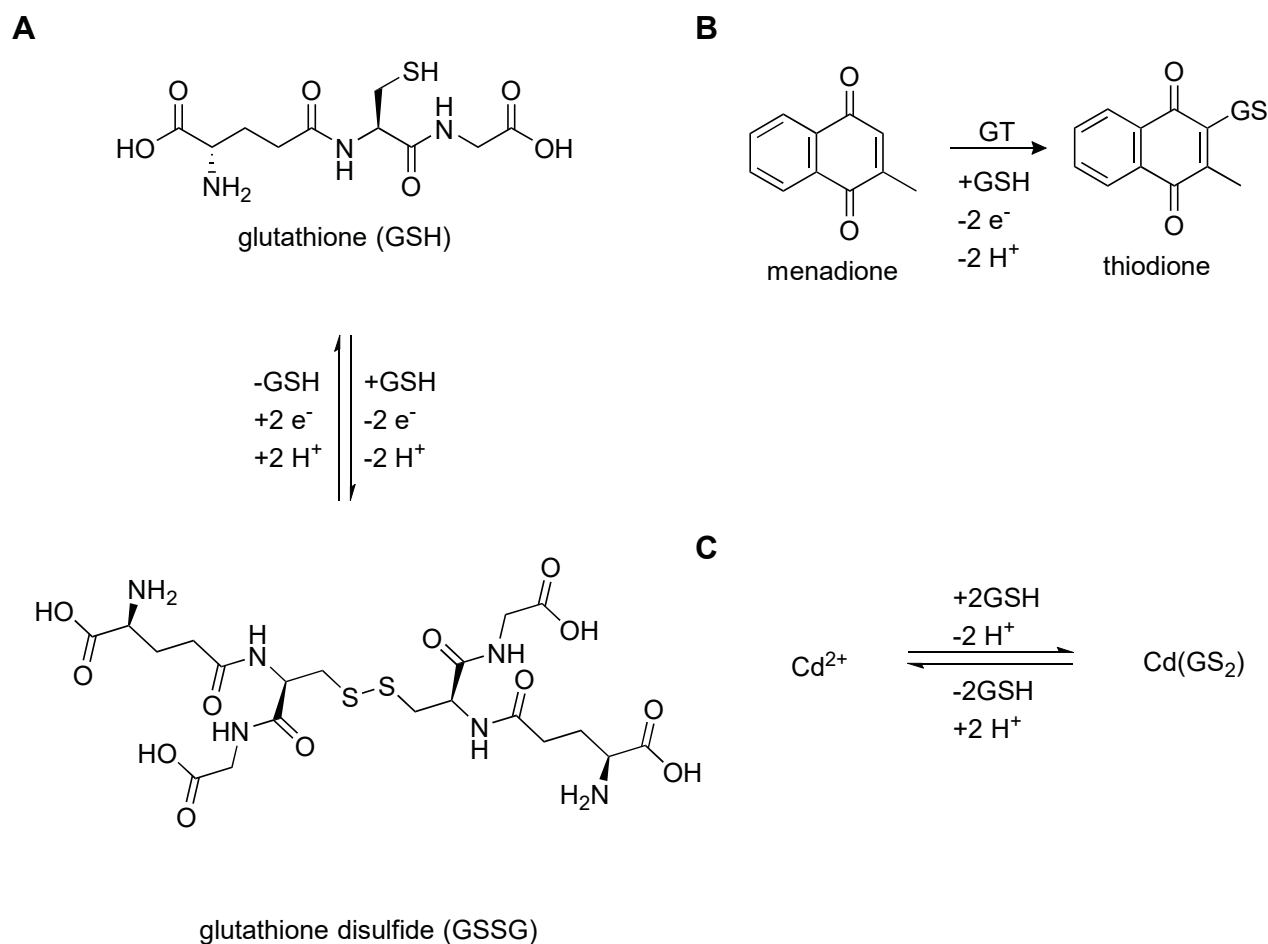


Figure 1.2: **A:** Oxidation of GSH to GSSG. **B:** GT-catalyzed GSH conjugation to xenobiotics. **C:** Chelation of GSH to cadmium.

MRP1 transport activity, as discussed in Section 1.6. Another difference between MRP1 and the other ABC-transporters involved in MDR is its preference towards transporting organic anions like GSH-, glucuronate-, and sulfate-conjugates, giving MRP1 a broad substrate scope (Figure 1.3).

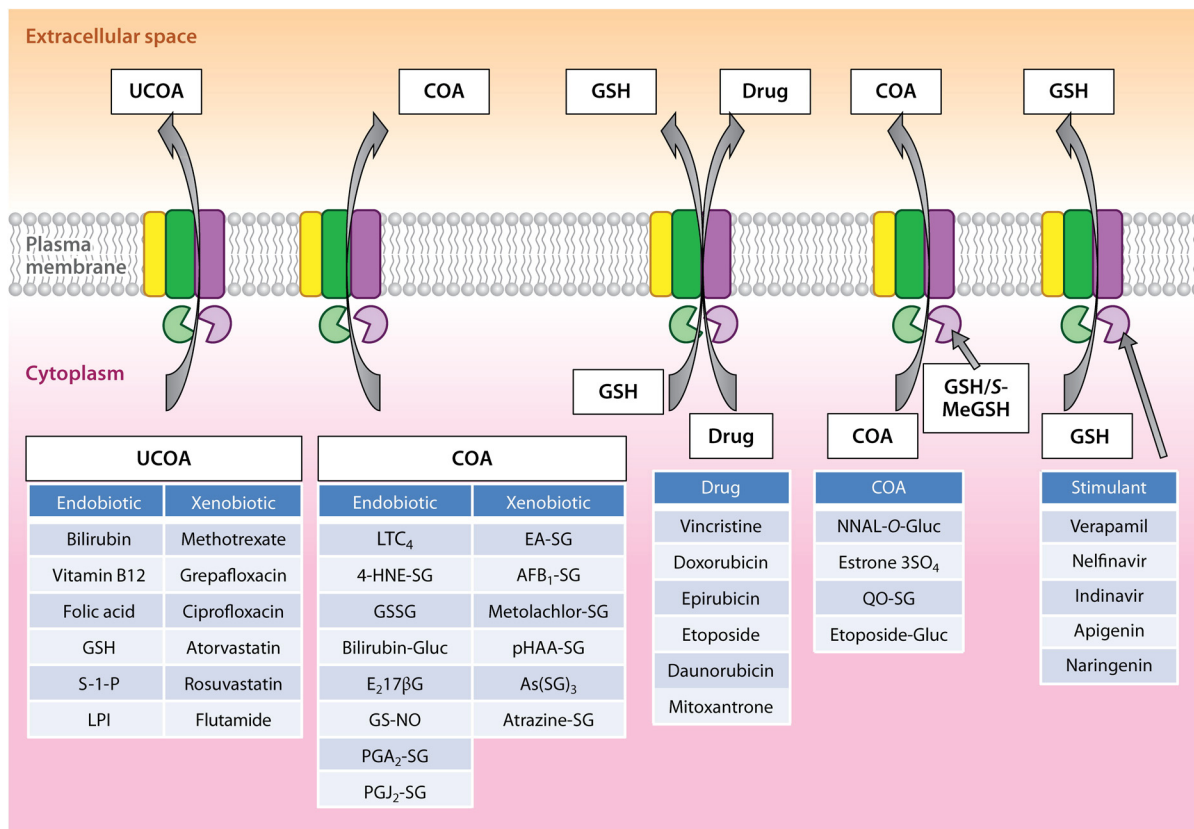


Figure 1.3: Transport mechanisms of multidrug resistance protein 1 (MRP1). Shown are representative examples of the endo- and xenobiotics (and organic anion metabolites) effluxed from cells by MRP1 in either a glutathione (GSH)-independent or GSH-dependent manner. Shown also on the far right is a diagram of MRP1-mediated transport of GSH that is stimulated by xenobiotics that are not themselves transported. Abbreviations: 4-HNE-SG, GSH conjugate of 4-hydroxy-2,3-trans-nonanal; AFB₁-SG, GSH conjugate of aflatoxin B₁-epoxide; COA, conjugated organic anion; E₂17βG, 17β-estradiol 17-(β-D-glucuronide); EA-SG, GSH conjugate of ethacrynic acid; GS-NO, S-nitrosoglutathione; GSSG, glutathione disulfide; LPI, lysophosphatidylinositol; LTC₄, leukotriene C₄; NNAL-O-Gluc, β-O-glucuronide conjugate of 4-(methylnitrosamino)-1-(3-pyridyl)-1-butanol; PGA₂-SG, GSH conjugate of prostaglandin A₂; PGJ₂-SG, GSH conjugate of 15-deoxy-Δ^{12,14}-prostaglandin J₂; pHAA-SG, GSH conjugate of acetaminophen; QO-SG, GSH conjugate of 4-nitroquinoline 1-oxide; S-1-P, sphingosine 1-phosphate; S-MeGSH, S-methyl GSH; UCOA, unconjugated organic anion. ©2014, with permission from Annual Reviews [11].

The prognostic significance of MRP1 expression in cancer patient survival is unclear. For instance, two reverse transcription polymerase chain reaction studies on the relationship between MRP1 mRNA expression and lymphoblastic-leukemia prognosis found no prognostic significance,^{19,20} while another study came to the opposite conclusion.²¹ There are also conflicting results regarding whether relapsing lymphoblastic-leukemia patients show increased MRP1 expression in cancerous tissue.^{19,22} Although MRP1 expression has in some cases been correlated to cancer patient prognosis, transport activity measurements are underdeveloped and therefore will be the focus of this thesis.

1.2 Measuring MRP1 Transport

1.2.1 Vesicles

The uptake of radiolabeled substrates into membrane vesicles is one of the primary ways of studying MDR proteins. The intravesicular concentration is determined by scintillation counting of filters with captured vesicles. These vesicles are produced from cell lines overexpressing MDR proteins by nitrogen cavitation cell lysis.²³ Early studies found an increased uptake of drugs like vinblastine in membrane vesicles from multidrug-resistant cell lines.^{24,25} Vesicular uptake studies lead to the discovery of many MRP1 substrates.^{26,27} When it was found that several leukotrienes (particularly LTC₄) and the GSH-conjugated prostaglandins A₁ and A₂²⁸ were substrates of MRP1,²⁹⁻³¹ it was proposed that MRP1 plays a role in inflammatory response.³² By studying the uptake of the inflammatory mediator [³H]LTC₄ in the presence and absence of ATP, it was found that MRP1 is an ATP-dependent transporter.^{30,31}

Leukotriene [³H]LTC₄,³³⁻³⁶ [³H]17 β -glucuronide estradiol,³⁵⁻³⁷ and [³H]estrone 3-sulfate^{36,37} are well established MRP1 model substrates, enabling the measurement of the inhibition of MRP1 in membrane vesicles. As a result, MRP1 inhibitors like MK571,^{36,38} verapamil,³³ cy-

closporin A,³¹ and tricyclic isoxazoles^{37,39-41} were identified. MRP1 inhibitors are clinically relevant due to their potential for reversing MDR. Most of these inhibitors are, unfortunately, non-specific to MRP1. Prior to the discovery of MRP1, MK571 was found to be a high-affinity LTC₄ receptor antagonist⁴² and to alleviate bronchoconstriction.^{43,44} It also inhibits MRP2,^{45,46} MRP4⁴⁷ and OATP1B3.⁴⁵ Although MK571 has been shown to reverse MRP1-mediated MDR *in vitro*,⁴⁸ the lack of specificity might be the reason why no single-target MRP1 modulator has made it to clinical trials.¹¹

1.2.2 Live Cells

Vesicular uptake studies have provided valuable information about the kinetics of MRP1 transport and inhibition. However, such measurements are not necessarily representative of cultured cells, and even less so for humans. The efflux of Calcein-AM, a fluorescent MRP1 substrate, is used to measure MRP1 transport activity.^{49,50} Low dye retention indicates high efflux, and therefore high MRP1 transport activity. This assay is not specific to MRP1; Calcein-AM is a substrate of P-gp and BCRP as well.⁵¹

Akin to the calcein-AM assay, retention of radiolabeled substrates in live cells can represent their efflux. In the case of [³H]verapamil, no active transport by MRP1 was found.³³ The uptake of etoposide decrease for MRP1- and P-glycoprotein-overexpressing leukemic cells.⁵² The relationship between cell death and drug exposure is typically measured using dose-response methods where cell viability is measured colorimetrically.⁵³

1.2.3 GSH as an MRP1 Substrate

Despite finding that MRP1 transports some GSH-conjugated inflammatory mediators, the physiological role of MRP1 remains unclear due to the lack of specific mechanistic explanations. The physiological role of MRP1 in GSH transport and regulation has been evaluated *ABCC1* (-/-) knock-out mice. These studies found lower GSH levels in several

MRP1-expressing tissues (*e.g.* lung, kidney, heart and testes) in control mice relative to *ABCC1* (-/-) knock-out mice.^{54,55} Lowered GSH levels can also be found in transfected MRP1-overexpressing HeLa cells,⁵⁶ but no clear trend is found for drug-selected MRP1-overexpressing cell lines.^{52,57–59}

Even though MRP1 expression affects the intracellular concentration of GSH in tissues and cultured cells, GSH was found in vesicular uptake studies to be a poor MRP1 substrate.^{33,38,60} However, MRP1-mediated vesicular uptake of GSH is induced by the cardiovascular drug verapamil,³³ chemotherapeutic drug vincristine⁶⁰ and flavon apigenin.⁶¹ When MRP1-overexpressing baby hamster kidney-21 cells are treated with verapamil, GSH depletion is induced through MRP1-efflux.³⁴ This opens up the possibility that there is an endogenous species that regulates MRP1-mediated GSH transport *in vivo*.

Since the intracellular concentration of GSH is high and its MRP1-mediated efflux can be induced by external stimuli, the extracellular GSH concentration could provide a basis for evaluating MRP1 activity. In fact, MRP1-transfected non-small cell lung cancer cells have been shown to release twice the amount of GSH into the extracellular environment as the non-transfected variant.⁶² SECM is a well suited technique for studying localized processes, and is emerging as a useful tool in live cell studies, due to its noninvasive nature.⁶³ The small probe size allows for single-cell analysis and could identify cancer heterogeneity, something that is challenging with the previously discussed methods.

1.3 Scanning Electrochemical Microscopy

SECM was introduced by Bard⁶⁴ and Engstrom⁶⁵ in 1989. SECM is a scanning probe method—a technique in which a probe moves across a surface of interest, measuring a local property—that allows for electrochemical measurements with high spatial resolution by us-

ing a microelectrode and a position control system.⁶³ Typical investigated systems include solid-liquid interfaces such as metals submerged in ionically conductive media.

Microelectrodes have at least one dimension $\leq 25 \mu\text{m}$.⁶⁶ In a typical SECM setup, at least one working electrode (usually a microelectrode), one reference electrode and one counter electrode is connected to a potentiostat (Figure 1.4). At the working electrode, the electrochemical reaction occurs. The reference electrode has a poised potential consistent with the Nernst equation. The counter electrode balances current flow in the electrochemical cell. The potentiostat and position control system are connected through a data acquisition system. In certain SECM instruments, an optical microscope is integrated to facilitate electrode positioning and surface visualization.^{63,67}

When a large overpotential is applied, the current recorded at the microelectrode (i) reaches a steady state indicative of mass-transport limitations (Figure 1.5A). This steady-state current is unique to microelectrodes and is caused by hemispherical mass transport to the electrode. In contrast, linear mass transport is commonly seen for macroelectrodes (typically mm-sized)

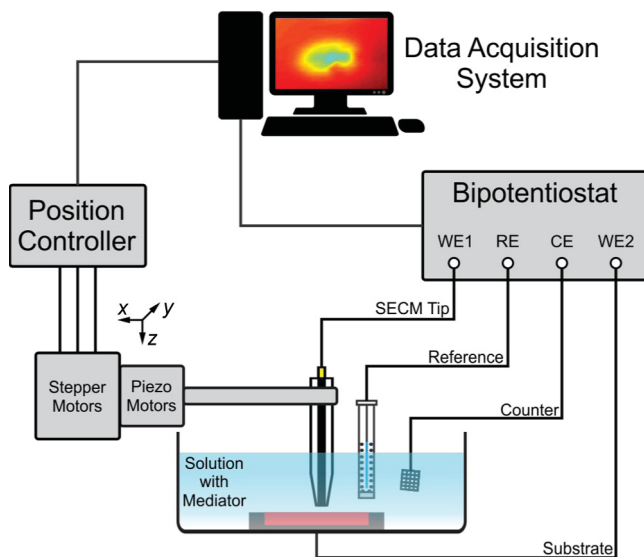


Figure 1.4: Schematic of SECM instrumentation. Reprinted with permission from ref 63. © 2016 American Chemical Society.

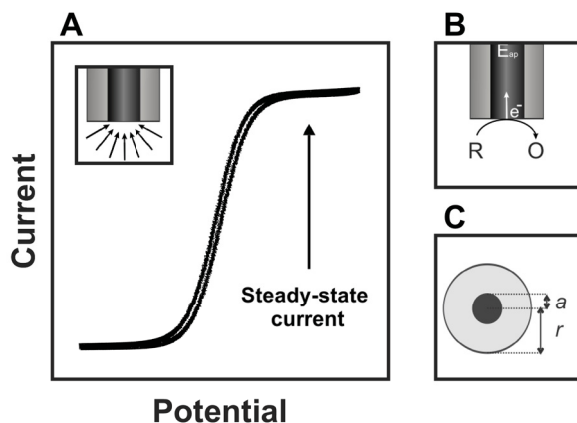


Figure 1.5: **A**: Cyclic voltammogram obtained using a microelectrode. When a substantial overpotential is applied, the current reaches steady state due to hemispherical mass transport. **B**: Oxidation occurring at an electrode. R and O are the reduced and oxidized form of the redox mediator, respectively. **C**: Definition of $RG = \frac{r}{a}$.

and does not yield steady-state behaviours. In the following discussion, the electrode reaction is assumed to be an oxidation under steady-state conditions, as seen in Figure 1.5B. An analytical approximation exists for the steady-state current at a disk microelectrode in bulk solution.^{68,69}

$$i_{\infty} = 4zD_{\text{R}}aFC_{\text{R}}^*\beta(RG) \quad (1.1)$$

Where z is the stoichiometric coefficient of the electron, D_{R} is the diffusion coefficient of R, F is Faraday's constant, C_{R}^* is the concentration of R in bulk solution and β is a geometric electrode coefficient. The β -coefficient is dependent on the $RG (= \frac{r}{a})$, Figure 1.5C. Several expressions for β have been reported.⁷⁰ One example is Equation 1.2, reported in 2006.⁷¹

$$\beta(RG) = 1 + 0.639 \left(1 - \frac{2}{\pi} \arccos \left(\frac{1}{RG} \right) \right) - 0.186 \left[1 - \frac{2}{\pi} \arccos \left(\frac{1}{RG} \right)^2 \right] \quad (1.2)$$

1.4 SECM Feedback Mode

In SECM feedback mode, i is measured as a function of tip-to-substrate distance (d , distance from microelectrode to surface of interest), electrode geometry and the substrates electrochemical activity. The relationship between i and d is dependent on a . Consequently, i and d are normalized to Ni ($= \frac{i}{i_\infty}$) and L ($= \frac{d}{a}$). When a microelectrode is moved towards a surface, the current changes according to the electrochemical activity of the surface. By recording the current with decreasing L , an approach curve is obtained. The electrochemical activity is described by a first-order heterogeneous rate constant for the regeneration of R by the surface (k , Figure 1.6A). Three scenarios of surface activity exit and are shown in Figure 1.6B; negative feedback (blue), $k = 0$; intermediate kinetics (black), k is finite and > 0 ; positive feedback (red), $k = \infty$.

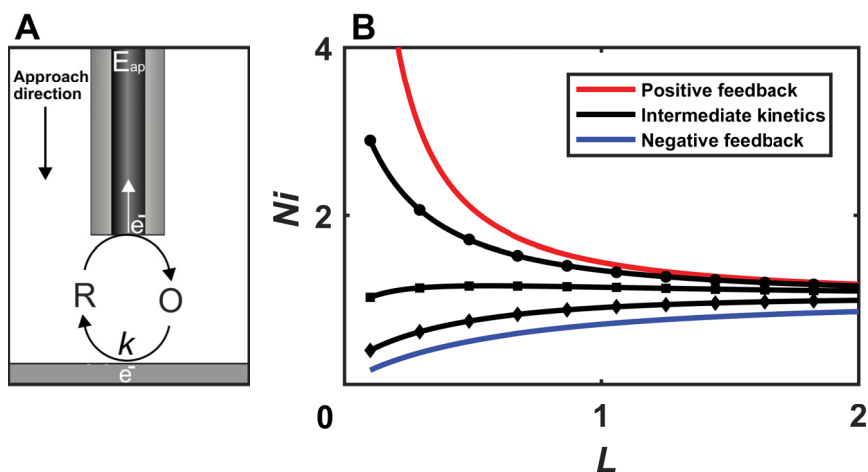


Figure 1.6: **A**: Microelectrode approaching a surface and electrochemical reactions for an SECM feedback approach curve. **B**: Approach curves plotted with the feedback approximations (Equation 1.3, 1.4 and 1.6) for positive feedback (red line), intermediate kinetics (black line, $\kappa = 5$ (circles), 1 (square), 0.2 (diamonds)) and negative feedback (blue line) from top to bottom, respectively.

1.4.1 Negative Feedback

When an electrode is approached to an insulating surface (*e.g.* glass and plastics) the current decreases, resulting in negative feedback. This is owed to hindered mass transport to the electrode and the inability of the surface to regenerate R. The newest analytical approximation, for an infinite surface, was reported in 2007.⁷² The accuracy ($Ni_{\text{approximated}} - Ni_{\text{simulated}}$) is ± 0.01 for all L and $RG < 200$ (Equation 1.3).

$$Ni^{\text{ins}}(L, RG) \approx \left[\frac{2.08}{RG^{0.358}} \left(L - \frac{0.145}{RG} \right) + 1.585 \right] \times \left[\frac{2.08}{RG^{0.358}} (L + 0.0023RG) + 1.57 + \frac{\ln(RG)}{L} + \frac{2}{\pi RG} \ln \left(1 + \frac{\pi RG}{2L} \right) \right]^{-1} \quad (1.3)$$

Equation 1.3 is used to extract electrode parameters like a and/or RG or characterize surfaces as insulators from experimental data.

1.4.2 Positive Feedback

When a microelectrode is approached to a conducting surface that is substantially larger than its electroactive area, the current increases due to the regeneration of R at the surface. This effect arises from the thermodynamical driving force of equalizing the O-to-R ratio throughout the solution. An analytical approximation for an infinite substrate was reported in 2006⁷¹ (Equation 1.4). The accuracy ($\frac{Ni_{\text{approximated}} - Ni_{\text{simulated}}}{Ni_{\text{simulated}}}$) is ± 0.02 for all L and RG .

$$Ni^{\text{con}}(L, RG) \approx \alpha(RG) + \frac{\pi}{4 \arctan(L) \beta(RG)} + \left(1 - \alpha(RG) - \frac{1}{2\beta(RG)} \right) \frac{2}{\pi} \arctan(L) \quad (1.4)$$

Where α is another geometric factor dependent on the RG (Equation 1.5).

$$\alpha(RG) \approx \ln(2) + \ln(2) \left(1 - \frac{2}{\pi} \arccos \left(\frac{1}{RG} \right) \right) - \ln(2) \left[1 - \left(\frac{2}{\pi} \arccos \left(\frac{1}{RG} \right) \right)^2 \right] \quad (1.5)$$

1.4.3 Intermediate Kinetics

When a surface displays intermediate ability to regenerate R, k can be quantified as κ , $= \frac{ka}{D}$. The most recent analytical approximation for irreversible kinetics at an infinite surface was reported in 2008 (Equation 1.6).⁷³

$$Ni(L, RG, \kappa) \approx Ni^{\text{con}} \left(L + \frac{1}{\kappa}, RG \right) + \frac{Ni^{\text{ins}}(L, RG) - 1}{(1 + 2.47 RG^{0.31} L \kappa)(1 + L^{0.006 RG + 0.113} \kappa^{-0.0236 RG + 0.91})} \quad (1.6)$$

This equation is valid for $RG \leq 20$, $L \geq 0.1$ and any κ . The accuracy ($Ni_{\text{approximated}} - Ni_{\text{simulated}}$ for $\kappa \leq 1$ and $\frac{Ni_{\text{approximated}} - Ni_{\text{simulated}}}{Ni_{\text{simulated}}}$ for $\kappa > 1$) is ± 0.025 . Equation 1.6 is used to extract kinetic information from a broad range of samples, ranging from immobilized enzymes⁷⁴ to solar cell materials.⁷⁵

1.5 Finite Element Modeling

Finite element modeling (FEM) provides numerical solutions for complex physical scenarios in engineering and physical sciences, including heat transfer, fluid flow and electrochemistry.^{76,77} When working at the μm -scale, the diffusion field of R to the microelectrode is no longer linear, making FEM an indispensable tool as analytical solutions are unavailable for most scenarios. In FEM, partial differential equations are discretized into sets of linear equations, which are easier to solve. The equations are then solved in an iterative fashion.

Linear diffusion will be described for simplicity. The first step in building a simulation model is to discretize time and space to Δt and Δx , respectively. The quality of the simu-

lation increases with the number of finite elements (Δt and Δx). A concentration profile is calculated from Fick's second law of mass transport, which relates concentration, flux, space and time.

$$-\frac{\partial C_{\text{R}}(x, t)}{\partial t} = \frac{\partial f(x, t)}{\partial x} \quad (1.7)$$

$$\lim_{t \rightarrow \infty} -\frac{\Delta C_{\text{R}}(x, t)}{\Delta t} = \lim_{x \rightarrow \infty} \frac{\Delta f(x, t)}{\Delta x} \quad (1.8)$$

Where C_{R} is the concentration of R, x is the spatial dimension perpendicular to the electrode surface, t is time and f is flux. The boundary condition for the reaction at the electrode is set such that all R is immediately consumed.

$$C_{\text{R}}|_{x=0} = 0 \quad (1.9)$$

The current is then calculated from the flux of R arriving at the electrode ($x = 0$) during a time step.

$$i(t) = \lim_{t \rightarrow \infty} -zAF\Delta x \left(\frac{\Delta C_{\text{R}}}{\Delta t} \right)_{x=0} \quad (1.10)$$

Where A is the electroactive area of the electrode, C_{R} the concentration of R, t is time. For substrates displaying irreversible kinetics at the surface (Figure 1.6A), the conversion rate at the substrate is defined as k .

$$\left. \frac{\partial C_{\text{O}}}{\partial t} \right|_{\text{substrate}} = kC_{\text{O}} \quad (1.11)$$

When building an SECM model, the simulated space is discretized in three dimensions. Currents are calculated in an iterative fashion, until they stabilize to steady-state currents (Figure 1.7B). If the simulated scenario has an axis of symmetry, and 2D-axisymmetrical

(2Da) simplification is commonly applied, which calculates the dimensions z and R_z (radius of space in the simulation) instead of x, y, z . A 2Da model is substantially less computationally demanding. The difference between a 3D and 2Da should be small as all currents are normalized to bulk solution before kinetic extraction.

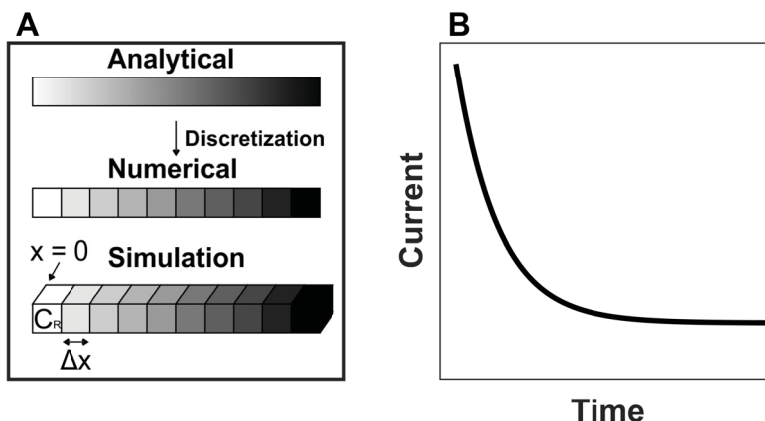


Figure 1.7: **A:** Discretization of the concentration profile. **B:** Current plateau arising as the simulation progresses.

1.6 Studies of Multidrug Resistance by SECM

The crux of studying multidrug resistance by SECM is the transport of species through the cell membrane. One example is the export of the menadione-GSH conjugate from yeast cells.⁷⁸ This conjugate is formed spontaneously when yeast cells are treated with menadione. Conjugation to GSH is the first step of the detoxification process. Subsequently, thiodione is actively exported out of the cells. The concentration of thiodione can be found through direct electrochemical detection, and its concentration over time was used to produce a thiodione efflux model. In this model, the efflux was set to be at least one order of magnitude higher than the menadione uptake. The flux of thiodione was estimated to be about 5×10^{-20} mol s^{-1} . Similarly, hepatocytes (Hep G2 cells) were investigated,⁷⁹ and found an efflux of 10^{-6} mol cell $^{-1}$ s^{-1} . At a later time, the conversion of menadione to thiodione was studied

in the HeLa cell line (Figure 1.8).⁸⁰ MK571 was used to inhibit MRP1 to show that the detoxification process was hindered.

The response of living cells towards different redox mediators has been studied by SECM.^{81,82} The Ding group has reported several studies of the effect of toxic heavy metal exposure on cell membrane permeability by extracting permeability coefficients from approach curves.⁸³⁻⁸⁷ The oxidation of FcMeOH near cells gives higher currents than for negative feedback. Cells appear to have reductive capabilities towards FcMeOH⁺. One of the main reductive components in cells is GSH, and several studies have described its reduction of FcMeOH⁺.^{88,89} In order to evaluate the use of FcMeOH and GSH to measure MRP1 efflux, the relationship between exposure to FcMeOH and GSH redox state was studied with flow cytometry and CMFDA staining.⁹⁰ The study concluded that exposure to FcMeOH resulted in a temporary increase in CMFDA fluorescence for the HeLa cell line. The study proposed that the intracellular GSH concentrations increased temporary for the HeLaR cell line, resulting in an increased GSH efflux that could be detected in SECM feedback mode.

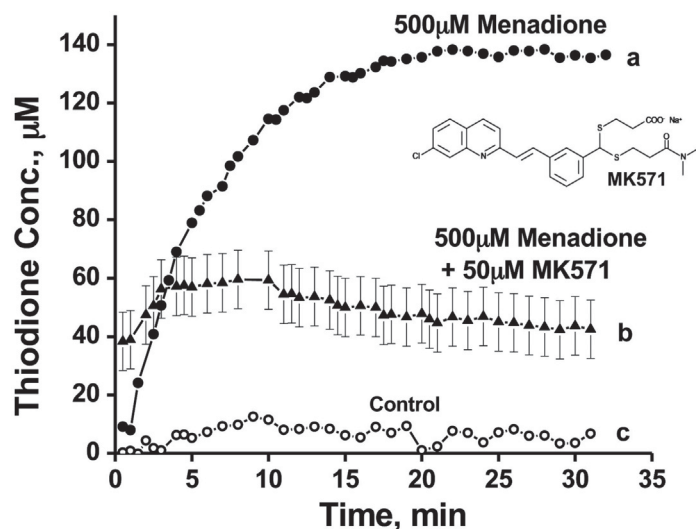


Figure 1.8: (a) Thiodione efflux from a monolayer of HeLa cells in the absence of MRP1 blocker MK571. (b) Thiodione concentration in the presence of 50 μM of MK571 and 500 μM menadione. (c) Control experiment in the presence of MK571 blocker. All the experimental conditions were the same except the control current was recorded without any menadione in the solution. The figure is reprinted with permission from citation [80].

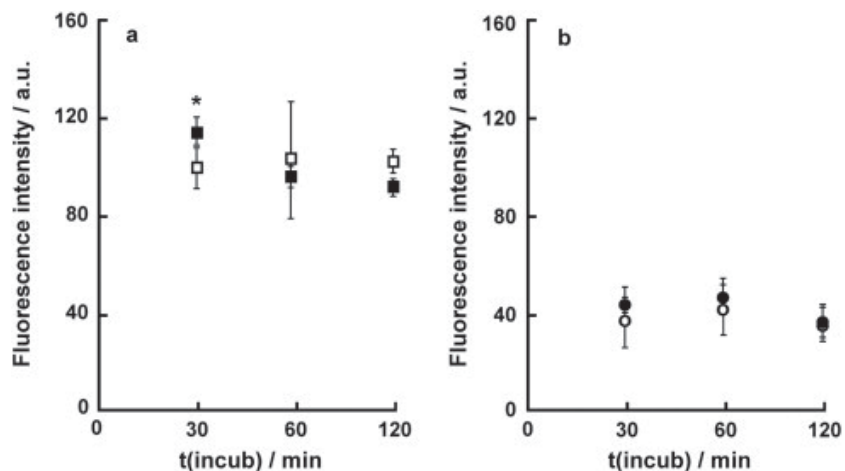


Figure 1.9: Influence of FcMeOH incubation time on CMFDA fluorescence intensity. HeLa (a) and HeLa-R (b) HeLa cells were exposed to 1 mM FcMeOH in DMEM- for 30, 60 and 120 min (■,●) and compared to those only incubated in DMEM- (□,○). Flow cytometry fluorescence measurements of CMFDA (2.5 μ M) added to the medium after 15, 45 or 105 min of incubation. The asterisks correspond to a significant difference ($n = 3$; error bars representing the confidence interval of CL 95%) between indicated groups. © 2011, with permission from Elsevier. [90]

In 2013, SECM feedback mode was used to study the reduction of FcMeOH⁺ by HeLa and HeLaR cells⁹¹ with the latter being the MRP1-overexpressing variant. In this study, a FcMeOH/Ru(NH₃)₆Cl₃ (Ruhex) dual mediator system was used to study MRP1 transport activity of GSH. First, a Ruhex current map was used to obtain a topography profile (Figure 1.10D). This topography profile was then combined with the FcMeOH map to extract κ , representing MRP1 transport activity (Figure 1.10D and F). The MRP1 activity profiles were compared between the cell lines, and the HeLaR cell line was found to have a 2.4 times higher κ maximum. A more recent studies with the same method found no difference between the HeLa and HeLa-R cell line, although a different HeLaR cell line was used.⁹² This study, however, found that the activity factor increased upon treatment with doxorubicin.

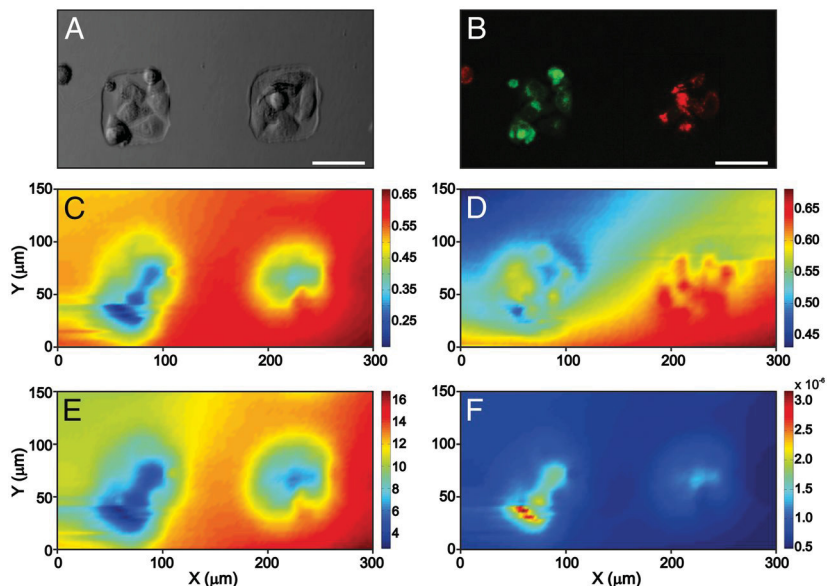


Figure 1.10: SECM imaging and decoupling of feedback response for a HeLa and HeLa-R cell coculture substrate. (A) Optical micrograph of a coculture pattern containing seven HeLa-R cells (Left) and six HeLa cells (Right). (B) Fluorescence micrograph of the sample shown in A, with HeLa-R cells stained green and HeLa cells stained red. (C and D) Normalized SECM currents recorded with the same sample at 12 μm above the substrate in 1 mM $[\text{Ru}(\text{NH}_3)_6]^{3+}$ (C) and 1 mM FcMeOH (D). (E) Extracted normalized tip-to-substrate distance profile. (F) Profile of the extracted apparent heterogeneous rate constant (cm s^{-1}) for the sample shown in A. (Scale bar: 50 μm .). The figure is reprinted with permission from citation [91].

1.7 Project Aims

This thesis extends SECM studies to a new cell type. It explores the effects of cell size, cell curvature and tip-to-substrate distance on accuracy in the previously developed feedback method, using simulated reference data. The feedback method is then used to assess the MRP1-mediated transport activity of GSH in stable cell lines with different MRP1 expression levels. This approach focuses on developing a robust method for quantifying MRP1 transport activity in order to classify degrees of multidrug resistance in cancer patient samples. Furthermore, such a platform can study the action of MRP1 inhibitors on living cells, which remains challenging today.

In Chapter 2, reference data will be simulated to investigate the single-point κ and L -fitting, used to assess MRP1 transport activity. The fitting process will first be assessed over flat substrates showing infinite behaviour as a reference point. Subsequently, curved finite substrates representing living cells will be studied. Once the conditions where κ can be accurately extracted has been established, the feedback method will be applied in live cell SECM studies.

In Chapter 3, the feedback method will be used to assess MRP1 transport activity of GSH in the HEK293 and HEKMRP1 cell lines. HEKMRP1 is transfected with a pcDNA3.1(-) expression vector in the Cole group to overexpress MRP1.⁹³ Using a transfected cell line would be advantageous to a resistant cell line obtained through a drug challenge, which can have other cellular mechanisms altered, *e.g* reduced drug uptake.^{2,3} The MRP1 transfection should yield a large difference in MRP1 expression, resulting in contrast between the cell lines MRP1 transport activity. The overexpression will first be verified by western blotting. The intracellular concentration of GSH will be quantified before the effects of MRP1 overexpression on GSH efflux will be studied, which could be dependent on GSH concentration. Then, cells will be patterned and imaged to investigate the MRP1 transport activity towards glutathione.^{91,92,94}

Chapter 2

Evaluating the Performance of a Dual Redox Mediator Approach in SECM Feedback Mode: Fitting Over Flat and Curved Substrates

2.1 Contributions

Chapter 2 was written by SS with the exception of the experimental sections on meshing and simulation geometries, which was written by LS. Simulations were carried out by LS. SS designed the experiments and treated all data.

Kinetic parameters in SECM feedback mode are typically extracted from fitting approach curves. Although such scans can provide kinetic information, they offer limited spatial resolution. The fitting of kinetic parameters requires knowledge of the tip-to-substrate distance. Chapter 2 validates the use of previously reported analytical approximations to calculate the tip-to-substrate distance from negative feedback currents. It has also been shown that it is

possible to extract kinetic parameters from a single point. This single-point fitting allows for the extraction of kinetic parameters from SECM line scans and images therefore taking full advantage of the technique's spatial resolution. The accuracy of single-point fitting methods was evaluated for curved finite substrates.

2.2 Introduction

The feedback mode of SECM is used to characterize substrate reactivity, extract microelectrode geometries (most commonly RG) and to determine the tip-to-substrate distance. To fit approach curves, a zero tip-to-substrate distance (L_0) is required. The lack of accuracy in L_0 greatly affects the ability to fit approach curves that are kinetically limited.⁹⁵ To circumvent this problem, four solutions exist.

1) The microelectrode can be forced to contact the substrate. Upon contact, an inflection in the approach curve is observed (Figure 2.1A). This inflection is then assumed to be L_0 . Often times, no single inflection point can be ascribed, compromising κ -fitting.

2) The error in tip-to-substrate distance (Err L , Figure 2.1B) can be defined as an adjustable fitting parameter, $Ni(d_z/a + \text{Err } L_0, \kappa, RG)$ (Figure 2.1C). Where d_z is the z-position (vertical) of the electrode and Err L_0 is the error in L_0 . This method has been suggested for a limited κ -range.⁹⁵

3) The use of an external controller based on shearforce,⁹⁶⁻⁹⁸ impedance,^{99,100} AC-SECM^{101,102} (alternating current), IC-SECM¹⁰³ (intermittent contact) and SECM-AFM¹⁰⁴⁻¹⁰⁶ (atomic-force microscopy) is known to keep track of L . Existing methods can certainly circumvent problems arising from varying topography, but require further instrumentation and can complicate experimental procedures.

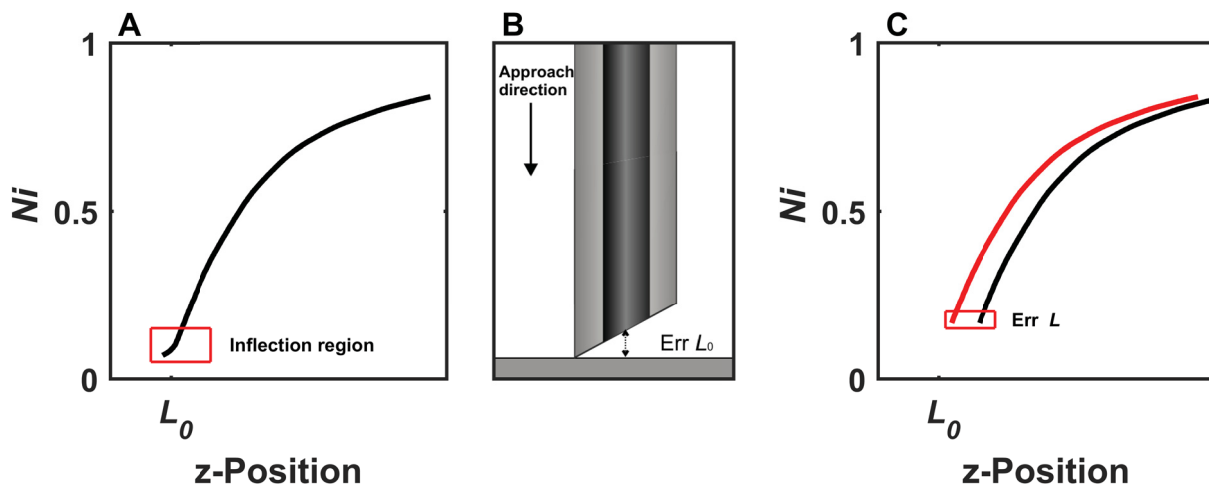


Figure 2.1: **A**: Approach curve example where the tip touches the substrate. **B**: Visual interpretation of $Err L_0$. **C**: Translation of an approach curve from fitting for $Err L_0$.

4) Normalized negative feedback currents are only dependent on L and RG . Since RG can easily be estimated from optical microscopy, L can be evaluated from experimental currents by comparison with simulated data or by fitting to the analytical approximations.⁷²

If the negative feedback current at a single point is enough to calculate L , then making contact with the substrate is unnecessary in many cases. This approach prevents damage to the electrode/substrate and removes the ambiguity associated with selecting L_0 from the inflection region (Figure 2.1A). For example, in live cell SECM experiments the cells are usually adhered to a flat plastic substrate. Since plastic substrates are electrically insulating, approach curves over such substrates give rise to negative feedback behaviour.

A redox mediator is considered to be irreversible when the reverse electron transfer reaction cannot occur, for instance, due to decomposition or dimerization (Figure 2.2A). For an irreversible redox mediator, negative feedback is observed, even over a conductor. Consequently, using a non-interfering dual-mediator system—one reversible and one irreversible redox mediator—can be used to fit approach curves without any other knowledge of L .¹⁰⁷

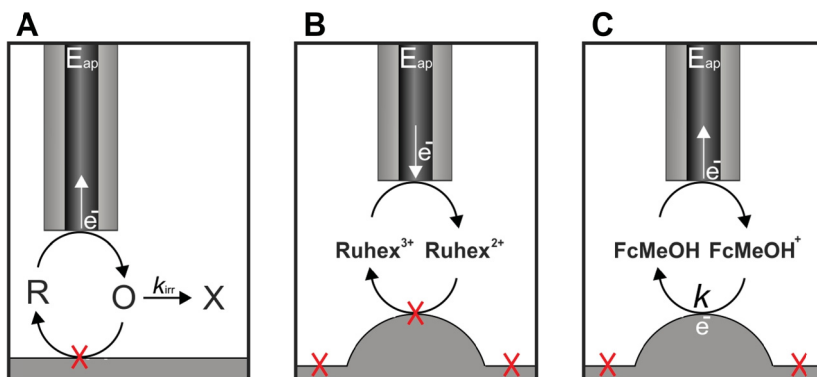


Figure 2.2: **A**: Negative feedback behaviour by an irreversible redox mediator towards a conductor. **B**: Negative feedback behaviour of the cell membrane towards Ruhex. **C**: Intermediate kinetics behaviour of the cell membrane towards FcMeOH.

This is especially critical for biological SECM studies, where its not always possible to obtain L by bringing the microelectrode in contact with a biological sample. For instance, crashing a microelectrode into a cell leads to electrode fouling, requiring the electrode to be repolished.

A negative feedback response is observed over cells while probing cell impermeable redox mediators that are not regenerated, for instance, $\text{Ru}(\text{NH}_3)_6\text{Cl}_3$ (Ruhex)⁸¹ and $\text{K}_4\text{Ru}(\text{CN})_6$ ⁸² (Figure 2.2B). These highly charged redox mediators do not cross the hydrophobic lipid bilayer, and lead to negative feedback behaviour representative of cell topography.¹⁰⁸ A dual-mediator system of FcMeOH/Ruhex has been used to fit surface kinetics/topography from current maps over living cells via the analytical approximations⁹² (Figure 2.2B-C). The negative feedback response of Ruhex was used to find a topography profile. The intermediate kinetics response of FcMeOH was used to fit for κ . Performing current mapping rather than approach curves increases the area of fitting κ , but the relative L between each point in the map is lost and only a single point is used to fit topography and surface kinetics. The accuracy of using the analytical approximations to fit L and κ to a single point is yet to be studied.

Analytical feedback approximations are used as a basis to further theoretical development of the feedback theory of ring microelectrodes,¹⁰⁹ extraction of enzymatic kinetic parameters,¹¹⁰ and porous films parameters.^{111,112} Better understanding of the fundamental equations can extend the range of these applications. Chapter 2 discusses the limits of the L and κ -fitting, for flat and curved substrates (*e.g.* living cells). Importantly, method accuracy will be evaluated when fitting entire approach curves, single-point fitting from approach curves, and SECM images. Reference data will be simulated using numerical finite element modeling.

2.3 Experimental

FEM was carried out using © COMSOL multiphysics version 5.3a for an oxidation occurring at the electrode surface.



Concentration profiles were simulated using ‘Transport of Diluted Species’ physics for C_{R} and C_{O} , the concentrations of R and O, respectively. Mass transport to the electrode was calculated according to Fick’s laws and D_{R} was chosen to be $6.7 \times 10^{-10} \text{ m}^2 \text{ s}^{-1}$, in line with that of FeMeOH in water at 25 °C.¹¹³

A dense mesh of triangular (2Da) or tetrahedral (3D) elements was introduced to the model geometry. This was designed to be densest in the region where significant concentration gradients would form; for the microelectrode, this is the electroactive surface; for the sample, this is in regions where a topographical or reactive feature was present.

The 2Da model was used to simulate approach curves over curved substrates of varying size and reactivity (Figure 2.3A). A hemispherical region of electrolyte with a radius of $100a$ was simulated in total. A triangular mesh was introduced to this domain with a maximum

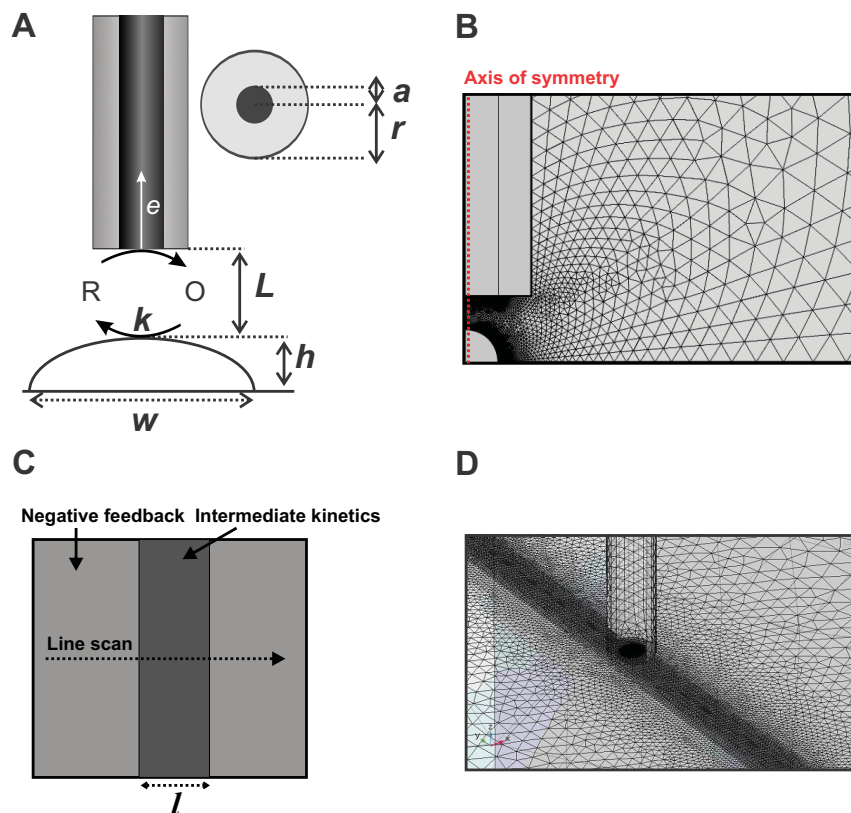


Figure 2.3: **A**: Scheme of parameters and geometries for the 2Da approach curve simulations. **B**: Mesh distribution example for the 2Da approach curve simulations. **C**: Scheme of parameters and geometries for the 3D approach line scan simulations. **D**: Mesh distribution example for the 3D line scan simulations.

element growth rate of 1.2. Further refinement was performed by applying an arithmetic distribution to the two surfaces where reactions take place (the electroactive area of the microelectrode and the substrate/electrolyte interface), using 75 elements and a ratio of 1. These settings resulted in a new optimal mesh being generated for each set of parameters (L , κ , W and H); in general, each of these meshes contained in excess of 7500 finite elements total (Figure 2.3B).

The 3D model was used to simulate line scans over conductive features embedded in an insulator for a flat substrate with no topographical features (Figure 2.3C). Electrode movement in the X and Y directions removed the previous axis of symmetry and required a switch

from the 2Da model used previously. A tetrahedral mesh was introduced to this domain with a maximum element growth rate of 1.4. Further refinement was performed by applying a maximum element size of $0.075a$ and $0.075l$ to the electroactive area of the microelectrode and reactive line respectively. A maximum growth rate of 1.1 was applied to the remainder of the substrate/electrolyte interface. These settings resulted in a new optimal mesh being generated for each set of parameters (x -position, l); in general, each of these meshes contained in excess of 125 000 finite elements total (Figure 2.3D).

All simulation parameters are reported in Table 2.1 and the ranges were linearly sampled. Simulation parameters are given the label ‘true’ to indicate that they are defined values.

Table 2.1: Table over simulation parameters. The number of points in a range is given in parentheses. All simulations were carried out with a microelectrode with a radius of $5 \mu\text{m}$.

Model	Experiment	$\log \kappa_{\text{true}}$	L_{true}	RG	H	W
2Da	AC Flat	$[-5,5]$ (200)	$[0.1,10]$ (200)	2,4,10,20	0	0
		$\kappa = 0$	$[0.1,10]$ (990)	2,4,10,20	0	0
	AC Curved	$[-2,2]$ (60)	$[0.1,2]$ (39)	2	$[0.2,3]$ (8)	$[0.2,3]$ (8)
		$\kappa = 0$	$[0.1,2]$ (39)	2	$[0.2,3]$ (8)	$[0.2,3]$ (8)
		$\kappa = 0$	$[0.1,10]$ (100)	2	$[0.2,2]$ (10)	1
Model	Experiment	κ_{true}	L_{true}	RG	l	
3D	Line scan	1	0.5	2	0, $0.5a$, $1a$, $2a$, $5a$, $10a$	

2.4 Single-Point L -Fitting over Flat Substrates

The first step in the investigation of using dual-mediator systems to deconvolute κ and L is to assess the fitting of L from negative feedback approach curves (Figure 2.4A). An approach

curve can be described as an $n \times 2$ matrix.

$$AC = [Ni_j \quad L_{j,\text{true}}] = \begin{bmatrix} Ni_1 & L_{1,\text{true}} \\ \vdots & \vdots \\ Ni_n & L_{n,\text{true}} \end{bmatrix} \quad (2.2)$$

Where n is the number of points and column 1 and 2 are Ni and L_{true} , respectively. A least-squares fit (LSF) to the analytical approximations⁷² of a negative feedback approach curve can be used to fit for an effective tip-to-substrate distance (L_{eff}) for each point.

Single-point fitting

$$\text{for } j = 1, 2, \dots, n \quad (2.3)$$

$$Ni_j^{\text{ins}}(L, RG) \xrightarrow{\text{LSF}} L_{j,\text{eff}}$$

The fitted L_{eff} is an $n \times 1$ vector, which represents the error in the equation for negligible error in the simulations. The error in tip-to-substrate distance ($\text{Err } L$) is defined as follows.

$$\text{Err } L = L_{\text{eff}} - L_{\text{true}} \quad (2.4)$$

The single-point topography fitting from negative feedback approach curves over flat substrates is shown in Figure 2.4. Figure 2.4**B** shows how L_{eff} (black, solid line) deviates from L_{true} (red, dashed line). Figure 2.4**C-F** shows $\text{Err } L$ as a function of L_{true} . $\text{Err } L$ is greatly dependent on L_{true} . At high L_{true} , $\left(\frac{dNi}{dL}\right)$ moves towards 0, making this region unsuited for topography fitting experimentally. For $L_{\text{true}} \leq 2$, $|\text{Err}| < 0.1$ as $\left(\frac{dNi}{dL}\right)$ is a lot higher in this region and is more suited for fitting L_{eff} . Closer to the surface ($L_{\text{true}} = [0.1, 0.5]$), the accuracy is excellent ($|\text{Err } L| < 0.022$) and L_{true} can be accurately found and used to position the electrode or calibrate the tip-to-substrate distance. The accuracy as a function of RG and L_{true} -range is reported in Table 2.3 (appendix).

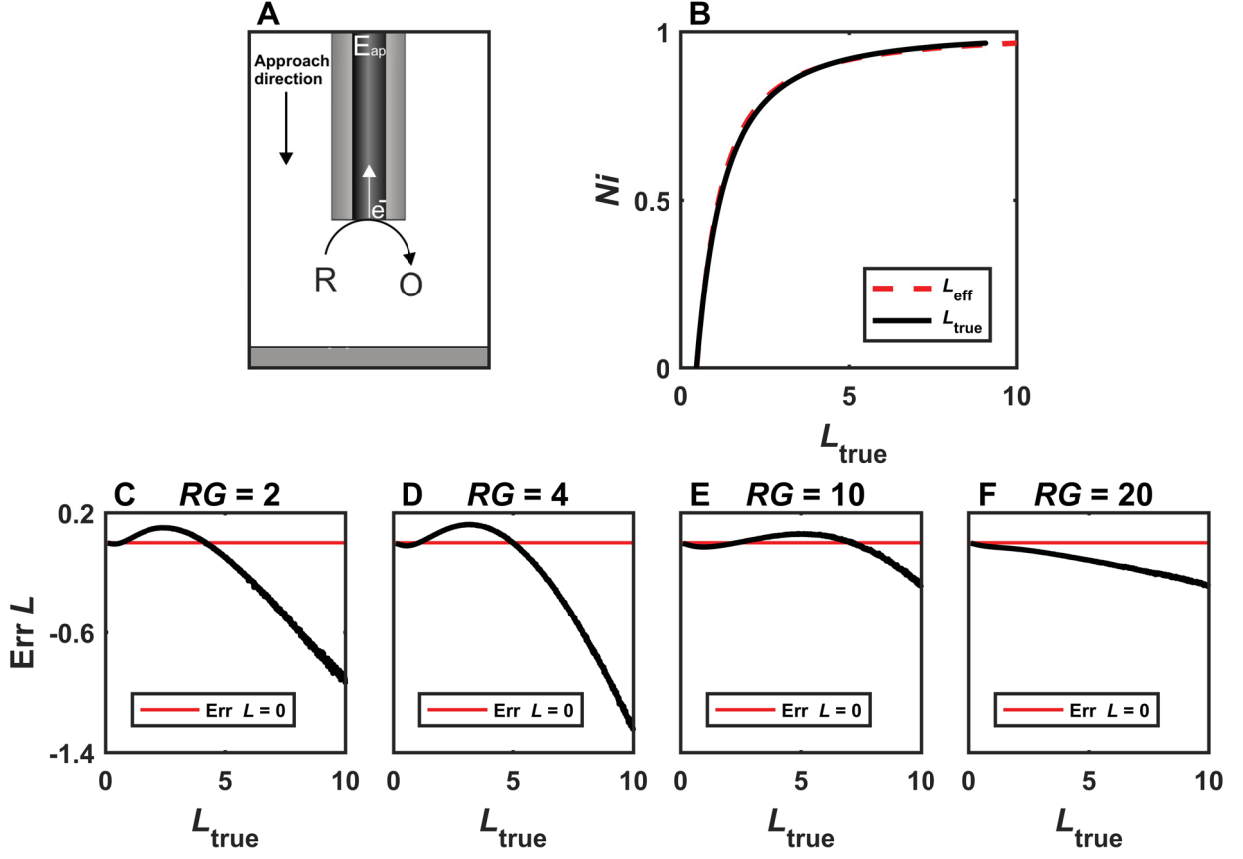


Figure 2.4: **A**: Scheme of a negative feedback approach curve over a flat substrate. **B**: Plot of a negative feedback approach curve ($RG = 2$) versus L_{eff} and L_{true} , showing the effect of single-point L -fitting on curve shape. **C-F**: Plots of $\text{Err } L$ versus L_{true} for $RG = 2, 4, 10, 20$, respectively

2.5 κ -Fitting over Flat Substrates

To evaluate when κ can be accurately fitted, $\text{Err } \kappa$ is defined.

$$\text{Err } \kappa = \log \frac{\kappa_{\text{eff}}}{\kappa_{\text{true}}} \quad (2.5)$$

Where κ_{true} is the simulations value and κ_{eff} is the fitted value. In this work, the $\text{Err } \kappa$ threshold is set to $\pm 20\%$ to be consistent with previous studies,⁹⁵ which corresponds approximately to $|\text{Err } \kappa| < 0.08$. κ_{eff} can be fitted in two ways. The first is when the

negative feedback approach curve is not available, L_{true} is assumed to be known. This fitting procedure consists of fitting the set of $L_{j,\text{true}}$ and $Ni_{j,\text{true}}$ to obtain a single κ_{eff} .

Single-mediator method

$$Ni_j(L_{\text{true}}, \kappa, RG) \xrightarrow{LSF} \kappa_{\text{eff}} \quad (2.6)$$

The other possibility is to use L_{eff} (found in Section 2.3) for the fitting, which is when the negative feedback curve is available.

Dual-mediator method

$$Ni_j(L_{\text{eff}}, \kappa, RG) \xrightarrow{LSF} \kappa_{\text{eff}} \quad (2.7)$$

Figure 2.5A shows a scheme of an intermediate kinetics approach curve. Figure 2.5B shows selected simulated approach curves (black, markers) and their curves fitted with the least-squares method (black, solid lines). Positive (red, solid line) and negative (blue, solid line) feedback curves are drawn for reference. A current plateau arises when κ_{true} becomes large or small (Figure 2.5C). Accurate κ -fitting is not expected in the plateau region due to the small $\left(\frac{dNi}{d\kappa_{\text{true}}}\right)$. To find the accuracy range, the minimum and maximum Err κ are plotted as a function of κ_{true} (Figure 2.5D-G) for both the single and dual-mediator method. These results reveal an interesting quality about the analytical approximations. The dual-mediator method increases the range from which $\log \kappa_{\text{eff}}$ can be accurately found from about $[-2, 2]$ to $[-4.5, 2]$ ($RG = 2$). For higher RG s, this range does not consistently increase but is shifted towards lower κ_{true} . All accuracy ranges are reported in the appendix (Table 2.4). Fitting an approach curve for $L_{\text{true}} = [0.1-10]$ does not substantially increase the range from which κ_{eff} can accurately be fitted over $L_{\text{true}} = [0.1, 5]$ and $[0.1, 2]$ (Table 2.4). Therefore, the dual-mediator method has been shown to be successful and outperforms the single mediator system for low κ_{true} and $RG = 2$, albeit lowered ability to fit for high κ_{true} .

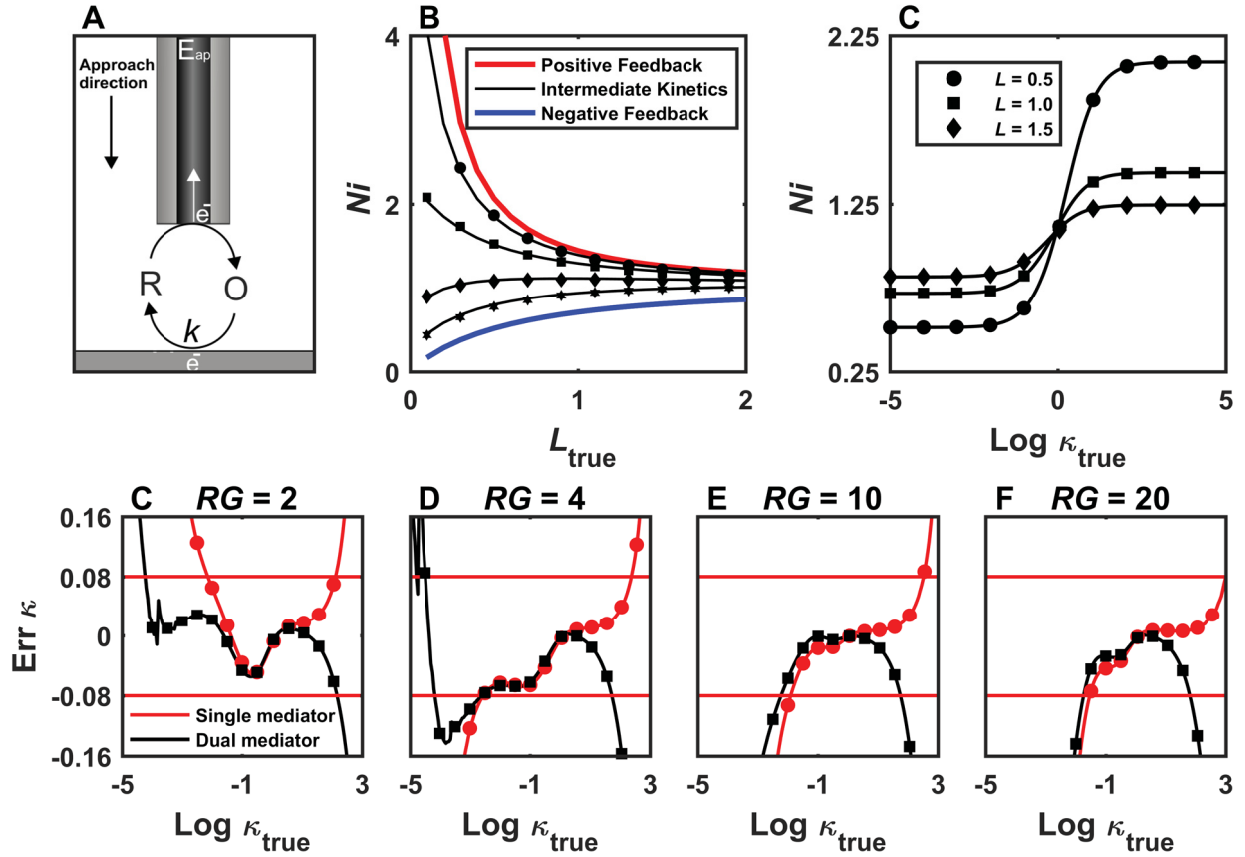


Figure 2.5: **A:** Scheme of an intermediate kinetics approach curves over a flat substrate. **B:** Plot of simulated approach curves—circles: $\kappa_{true} = 10$, squares: $\kappa_{true} = 2.82$, diamonds: $\kappa_{true} = 0.79$, stars: $\kappa_{true} = 0.32$ —and their curves fitted for κ_{eff} (black solid lines). Red and blue curves represent positive and negative feedback response calculated with their respective analytical approximations.^{71,72} **C:** Plot of Ni versus $\log \kappa_{true}$ at constant height of $L_{true} = 0.5, 1.0, 1.5$ for the simulated approach curves in B. **D-H:** Plots of $Err \kappa$ as a function of κ_{true} and RG .

2.6 Single-Point κ -Fitting over Flat Substrates

Being able to fit for κ_{eff} from a single point could dramatically increase the area of kinetic extraction or reduce acquisition time. When L_{true} is known, κ_{eff} can be calculated.

Single-point, Single-mediator method

$$\text{for } j = 1, 2, \dots, n \quad (2.8)$$

$$Ni_j(L_{\text{true}}, \kappa, RG) \xrightarrow{LSF} \kappa_{j,\text{eff}}$$

The other possibility is to fit with L_{eff} , which is when the negative feedback curve is available.

Single-point, Dual-mediator method

$$\text{for } j = 1, 2, \dots, n \quad (2.9)$$

$$Ni_j(L_{\text{eff}}, \kappa, RG) \xrightarrow{LSF} \kappa_{j,\text{eff}}$$

The threshold of $|\text{Err } \kappa| \leq 0.08$ is applied to evaluate the single-point fitting. Figure 2.6 shows logic plots where red represents an error above the limit and blue an error below. Single-point fitting works for low L_{true} (below ≈ 2). The range $L_{\text{true}} = [0.1, 1]$ is used to compare the different methods and RG s. The black inset box in Figure 2.6 shows the region of accurate κ -fitting. The dual-mediator methods outperforms the single-mediator method for $RG = 2, 4$, but not $RG = 10, 20$. The dual-mediator method shifts the accurate region towards lower κ_{true} . In conclusion, κ_{eff} can be accurately fitted with one point close to the substrate. One of the implications of this work is that kinetic extraction from current maps is possible, substantiating previously reported experimental work.^{91,92} However, the effect of deviations from infinite flat substrates on κ -fitting is next to be investigated.

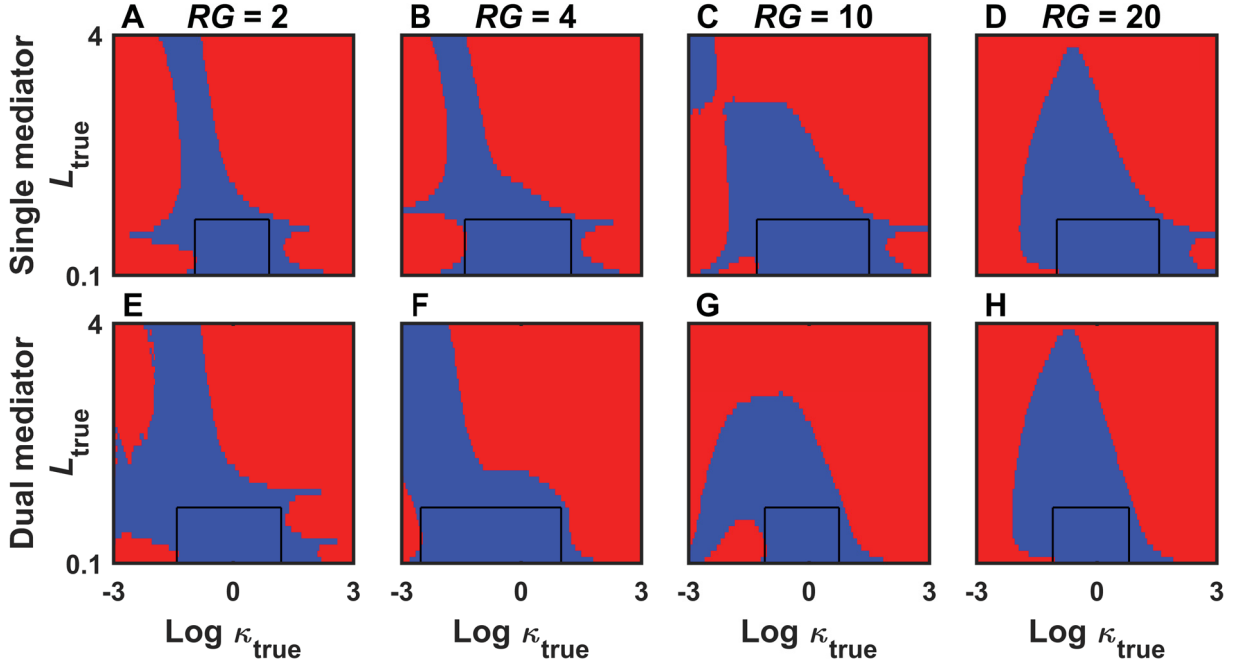


Figure 2.6: Error plots for the single-point κ -fitting from simulated intermediate kinetics approach curves over a flat substrate. Red denotes $|\text{Err } \kappa| > 0.08$ and blue denotes $|\text{Err } \kappa| \leq 0.08$. **A-D**: Single mediator method (fitted with L_{true}) **E-H**: Dual-mediator method (fitted with L_{eff}). Inset boxes represents the range where $|\text{Err } \kappa| \leq 0.08$ for $L_{\text{true}} = [0.1, 1]$.

Table 2.2: Comparison between the single and dual-mediator systems for the single-point κ -fitting in the range $L_{\text{true}} = [0.1, 1]$. The range from which κ_{eff} can be fitted with $|\text{Err } \kappa| \leq 0.08$ is reported as $[\min(\log \kappa_{\text{true}}), \max(\log \kappa_{\text{true}})]$

Method	$RG = 2$	$RG = 4$	$RG = 10$	$RG = 20$
Single mediator	[-0.95,0.90]	[-1.40,1.25]	[-1.30 1.50]	[-1.00 1.55]
Dual mediator	[-1.40,1.20]	[-2.50,0.75]	[-1.10,0.75]	[-1.10,0.80]

2.7 Applying the Single-Point κ -Fitting to Line Scans

Current mapping is frequently used to locate and study regions of reactivity. Typically, these experiments are accompanied by approach curve experiments for kinetic extraction. This section demonstrates that κ -fitting is applicable to current images and line scans (obtained in the x - y plane). When studying localized processes, the regions used for kinetic extraction must be larger than a certain size in order to fit to the analytical approximations. This is because such approximations have been developed for infinite substrates. When the reactive

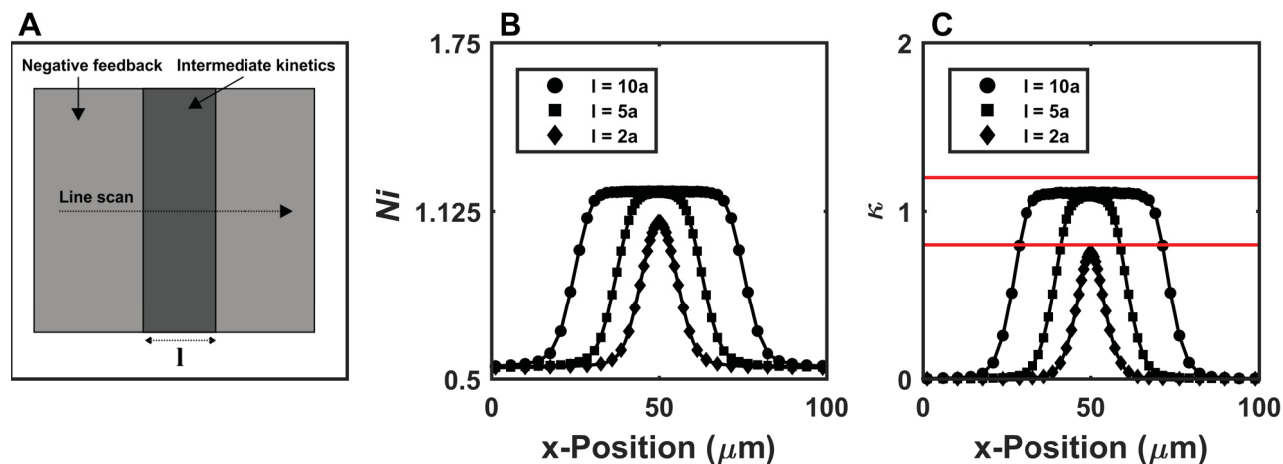


Figure 2.7: **A**: Scheme of a line scan with varying linewidth over a line displaying intermediate kinetics. **B**: Linescan currents for $L_{\text{true}} = 0.5$, $\kappa_{\text{true}} = 1$ and $l = 10a, 5a, 2a$. **C**: Single-point κ -fitting for the line scans in **B**. The current at x-position $200 \mu\text{m}$ was used to fit for L_{eff} .

region used for kinetic extraction is too small, but the geometry is known, it is possible to obtain kinetic information through numerical simulations.¹¹⁴ Poor fits are expected if the substrate is not large enough, and no widespread fitting quality parameter is applied.

Current plateaus in SECM experiments can help identify if infinite substrate behaviour is observed in the scan direction. Current plateaus arise when moving the electrode further towards the center of a reactive region does not cause a current change. The region before the edge of the reactive region no longer contributes to the current, and the reactive region behaves as an infinite substrate. If the surrounding region displays negative feedback behaviour, this region can be used to fit for L_{eff} , which allows for κ -fitting. If this is not the case, the dual-mediator method or another method for finding the tip-to-substrate distance is necessary.

A series of line scans over a line feature of intermediate kinetics were simulated to illustrate that single-point fitting can be applied to line scans and current maps (Figure 2.7A).

The line width of the reactive region (l) was varied to find the width where the current plateaus. Example lines scans are shown in Figure 2.7B. The current reaches a plateau for $l \geq 5a$. Single-point fitting of the line scans found κ_{eff} within the error of $|\text{Err} > 0.08|$ (Figure 2.7C). The x-position of $200 \mu\text{m}$ was used to fit for L_{true} . Single-point κ -fitting has been shown to be accurate for kinetic fitting of line scans while simultaneously determining if the reactive region behaves as an infinite substrate. This method could also function as a slope correction, as κ should be independent of slope (for constant accuracy).

2.8 Single-Point L -Fitting over Curved Substrates

For curved substrates, L_{true} is defined as the normalized distance between the electrode and the ellipse co-vertex (Figure 2.3A). Figure 2.8A shows a scheme of a negative feedback approach curve over a curved substrate. Figure 2.8C shows how height, H , affects the approach curve shape for width, $W, = 1$. The change in curvature causes substantial deviations in L_{eff} (Figure 2.8D). When L_{true} increases, the currents converge towards the bulk value and $\text{Err } L = \text{Err } L_{\text{flat}} + H$. It is therefore most useful to look at topography extraction at low L_{true} , where $\left(\frac{dN_i}{dL}\right)$ is largest.

Figure 2.8D-G shows how $\text{Err } L$ changes close to the surface ($L_{\text{true}} = [0.1, 2]$) for different H and W . Although the errors can be low at $L_{\text{true}} = 0.1$, the maximum $\text{Err } L$ for each approach curve is > 0.23 . This means that accurate L_{eff} is unavailable for the simulated geometries. Larger substrate geometries should be simulated to find the limit of accuracy in future works. For negative feedback, the current is only dependent on mass transport to the electrode. For intermediate kinetics, the regenerated species need to move back to the electrode as well, meaning that curvature is not expected to affect negative feedback and intermediate kinetics behaviour in the same way. Consequently, inaccurate L -fitting does not necessarily imply inaccurate κ -fitting.

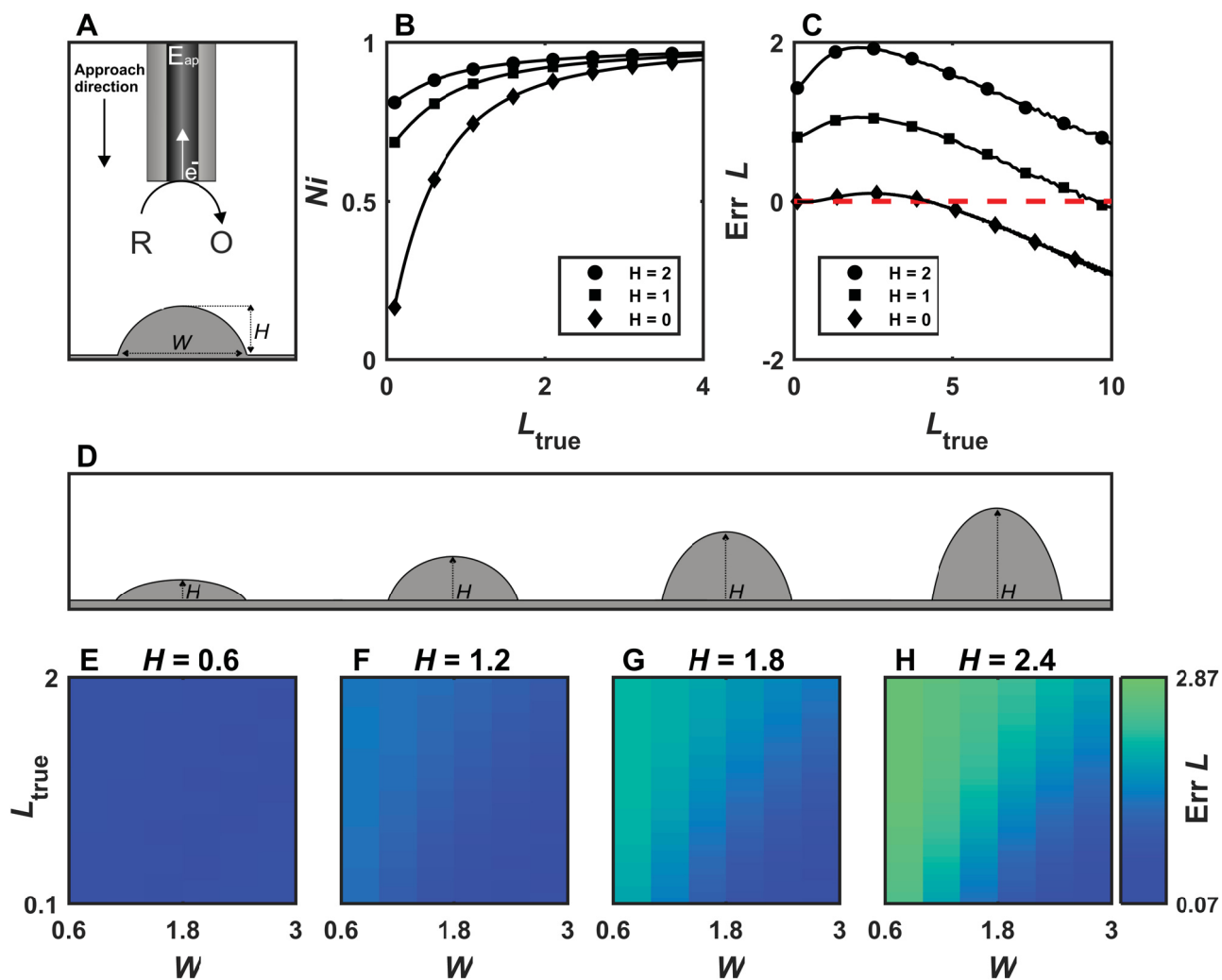


Figure 2.8: **A:** Scheme of a negative feedback approach curve over a curved substrate. **B:** Plot of concentric negative feedback approach curves over curved substrates ($W = 1$, $a = 5 \mu\text{m}$, $RG = 2$). **C:** Plot of $Err L$ versus L_{true} for the L -fitting from the curves in **A**. **D:** Change in H . **E-H:** Plots of $Err L$ versus W for the L -fitting for all curved substrates.

2.9 κ -Fitting over Curved Substrates

Fitting approach curves over curved substrates with dual-mediator method improves the accuracy compared to the single mediator method (Figure 2.9). The accuracy decreases with height and increases with width. The fitting is most successful for L_{true} and $W \geq 3$. This size corresponds roughly to a HEK293 cell. The regions of accuracy for this case are summarized in Table 2.5, in the appendix.

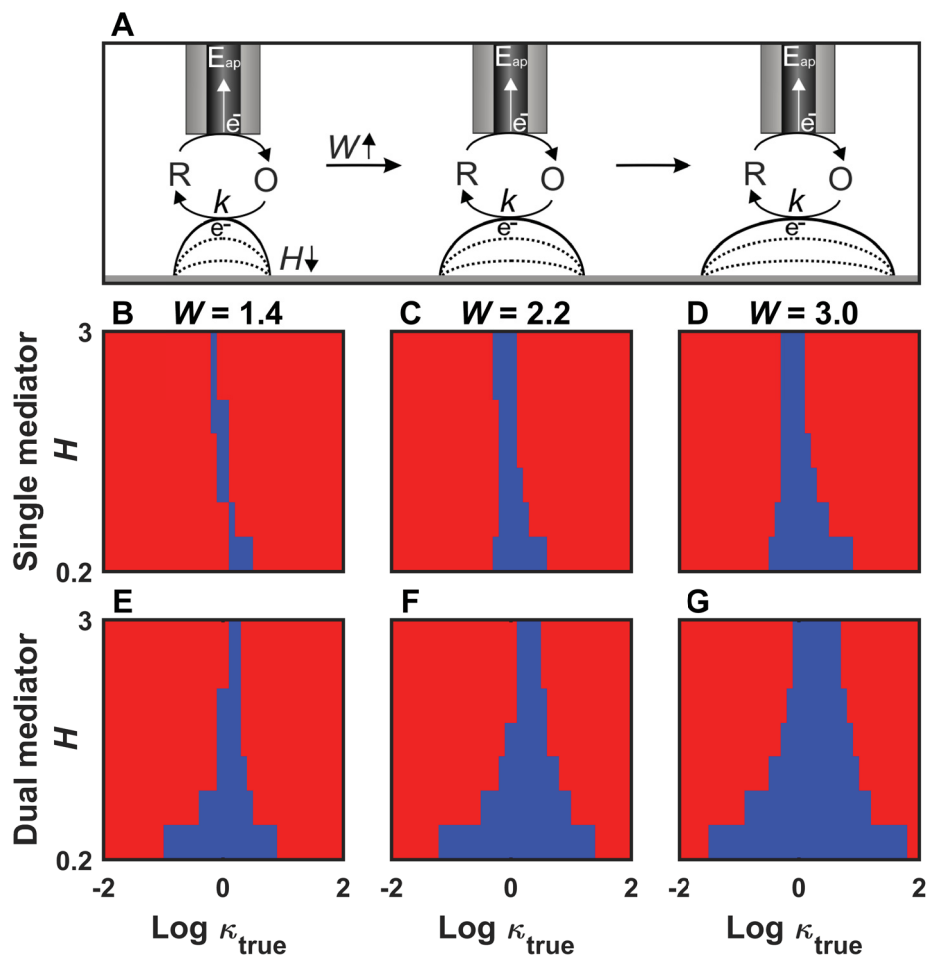


Figure 2.9: **A**: Scheme over intermediate kinetics approach curves over the simulated geometries. **B-G**: Logic plots of κ -fitting of simulated approach curves over curved substrates ($L_{\text{true}} = [0.1, 1]$). Red indicates that $|\text{Err } \kappa| > 0.08$ and blue denotes $|\text{Err } \kappa| \leq 0.08$. **B-D**: Single mediator method (fitted with L_{true}) **E-G**: Dual-mediator method (fitted with L_{eff})

2.10 Single-Point κ -Fitting over Curved Substrates

Accurate single-point κ -fitting is not possible for the curved substrate case (Figure 2.10). The best accuracy is achieved for small H and large W , as seen in Figure 2.10J. In future works, dimensions will be increased to find the accuracy range. Fitting with L_{true} , gives more accurate satisfying results (Figure 2.12, appendix).

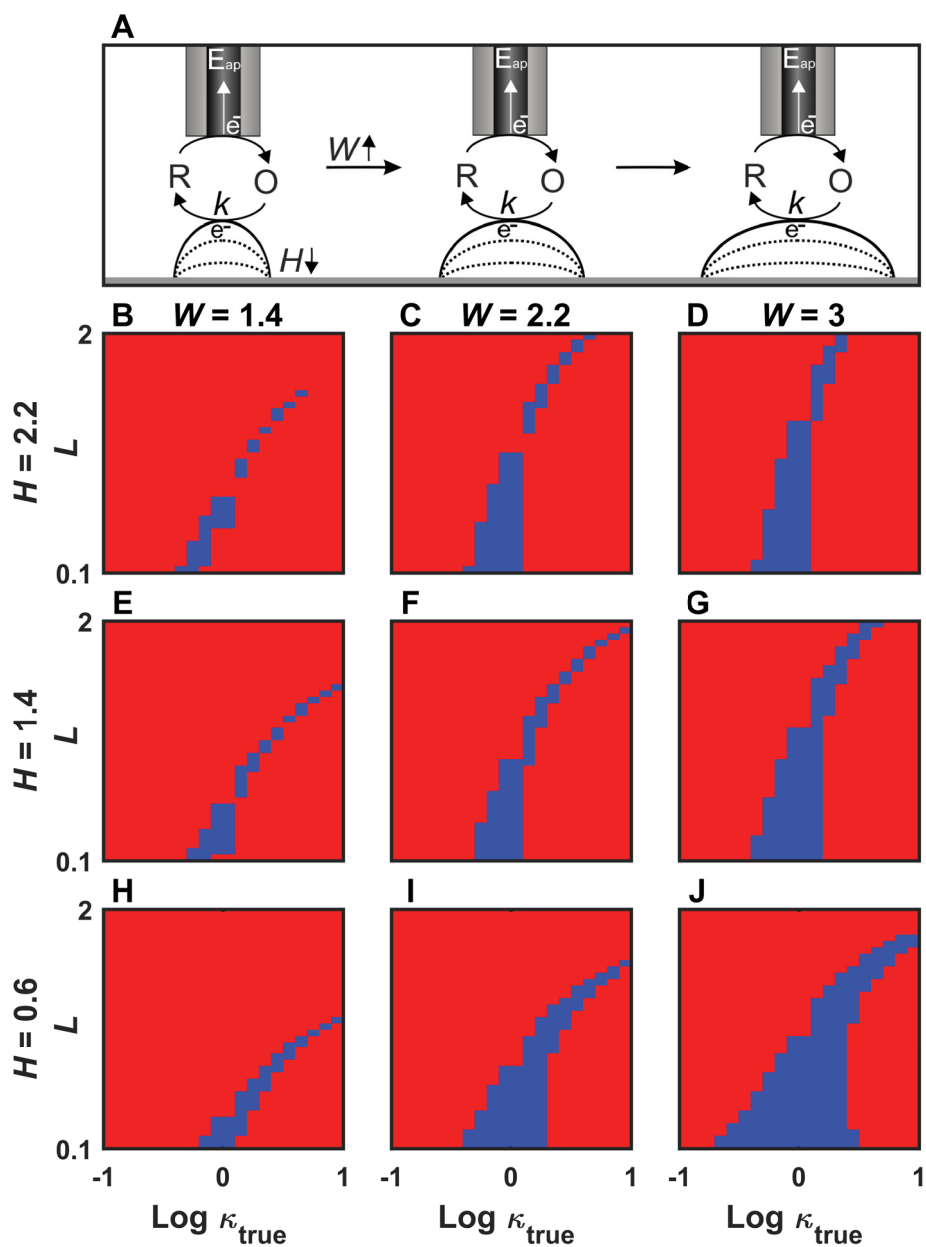


Figure 2.10: **A**: Scheme over approach curves over curved substrates displaying intermediate kinetics. **B-J**: Logic plots for the single-point κ -fitting (with L_{true}) of simulated approach curves over curved substrates ($L_{\text{true}} = [0.1, 1]$). Red indicates that $|\text{Err } \kappa| > 0.08$ and blue denotes $|\text{Err } \kappa| \leq 0.08$.

2.11 Evaluation of Extraction Methods and Simulations

Analytical approximations are used by a great majority of experimentalist. To compare the discrepancy between the simulated approach curves reported herein and the reported accuracy of the analytical approximations, error parameters are defined. The current error ($\text{Err } Ni$) is defined in line with previous studies.⁷³

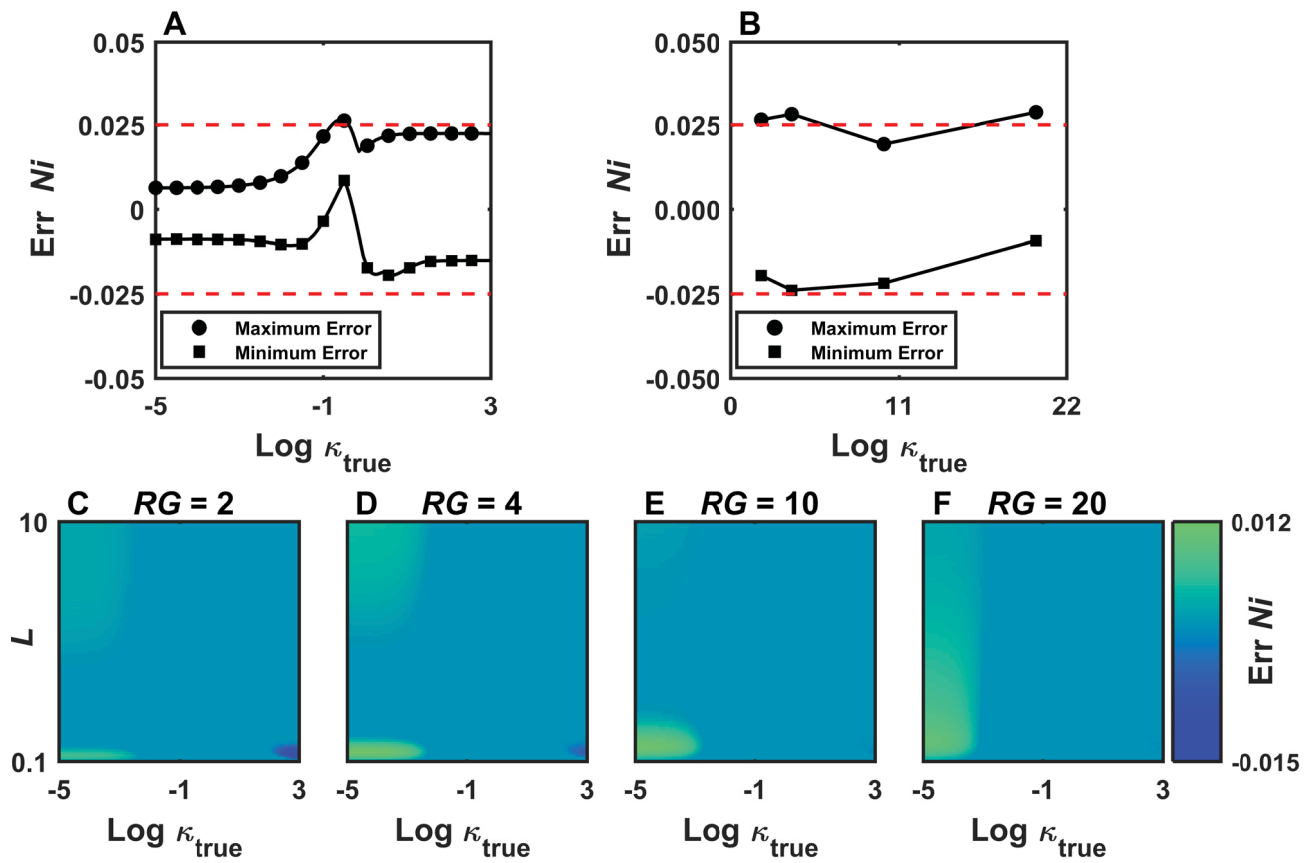


Figure 2.11: **A**: Plot of $\max(\text{Err } Ni)$ and $\min(\text{Err } Ni)$ versus κ_{true} for simulated approach curves ($L_{\text{true}} = [0.1, 10]$ and $RG = 2$). **B**: Plot of $\max(\text{Err } Ni)$ and $\min(\text{Err } Ni)$ versus RG for four sets of approach curves ($L_{\text{true}} = [0.1, 10]$, $\text{log } \kappa_{\text{true}} = [-5, 3]$) **C-F**: Evaluation of the single-point κ and L -fitting (Figure 2.6). The current errors were calculated with Equation 2.10.

$$\begin{aligned}
\text{Err } Ni &= Ni_{\text{app}} - Ni_{\text{sim}} && \text{For } \kappa \leq 1 \\
\text{Err } Ni &= \frac{Ni_{\text{app}} - Ni_{\text{sim}}}{Ni_{\text{sim}}} && \text{For } \kappa > 1
\end{aligned} \tag{2.10}$$

Where Ni_{app} is the normalized current calculated with the analytical approximations and Ni_{sim} is the normalized simulated current. The relative error becomes large for low κ_{true} and the absolute error becomes large for high κ_{true} . By discontinuously defining the current error, its value represents the quality of the fit across all κ . It is possible to compare the simulations to published simulations by defining the current errors as previously done in literature.⁷³ $\text{Err } Ni$ should be below 0.025 for the intermediate kinetics case. Figure 2.11A shows the minimum and maximum $\text{Err } Ni$ for 200 approach curves ($L_{\text{true}} = [0.1, 10]$ and $RG = 2$). Figure 2.11B shows the maximum and minimum $\text{Err } Ni$ for the approach curve sets ($L_{\text{true}} = [0.1, 10]$ and $\log \kappa_{\text{true}} = [-5, 5]$) for each RG . $|\text{Err } Ni| < 0.029$ for all approach curves, a reasonable agreement with literature error ranges,⁷³ albeit slightly higher than the reported value of 0.025.⁷³ Only a few points for each curve as shown in Figure 2.11A exceed this limit, which means that only a fraction of the points in a fraction of the approach curves are above the reported error. Unfortunately, the κ -region affected is where $\left(\frac{dNi}{d\kappa_{\text{true}}}\right)$ is largest and is most suited for κ -fitting. The exact reason for this discrepancy is difficult to identify, but it is probably an artifact of simulation differences; most likely, sampling density. To determine if the κ -fitting is working optimally, the κ_{eff} and L_{eff} was inserted into the analytical approximations, as shown in Figure 2.11C-F. The $|\text{Err } Ni| < 0.01$ for most regions, which means that the fitting method works as intended. It does not work well for the extremal κ_{true} , which is expected because of the current plateau in these cases (Figure 2.5C).

2.12 Conclusions

In Chapter 2, it was shown that when fitting entire approach curves (or a single point) to extract κ over a flat substrate of intermediate kinetic behaviour, the range of accurate extraction is increased by simultaneously fitting with the experimental negative feedback currents for low RGs (2 and 4). The opposite is true for high RGs . This dual-mediator method shifts the accurate κ -range towards lower κ . Technically, the dual-mediator fitting can be done by fitting negative feedback approach curves for L_{eff} at each point. This found L is subsequently put into the analytical approximations for intermediate kinetics. This eliminates the need to find the tip-to-substrate distance experimentally and removes ambiguity in κ -fitting. This method also avoids microelectrode-substrate contact and eliminates the electrode size error in κ -fitting, which can affect the L -normalization. In fact, fitting experimental approach curves is not always straight forward and error in a might be one of the contributors to this.

The dual-mediator method requires a preferential mediator response from a surface, negative feedback, and intermediate kinetics. Selecting an irreversible redox mediator (e.g. anthracene¹⁰⁷) or a redox mediator where the reverse reaction is unfavored will result in negative feedback behaviour. Moreover, the cell membrane shows preferential response to different redox mediators and Ruhex can be used as a negative feedback mediator. It is also possible to use the dual-mediator method for studying patterned enzymes by adding an extra mediator that does not interact with the surface. It has also been shown that an approach curve (or a single point) can be fitted over curved substrates of intermediate kinetics with comparable dimensions to the electrode, albeit with a drastically shortened κ -ranges.

2.13 Appendix

2.13.1 Single-Point L -Fitting over Flat Substrates

Table 2.3: Overview of Err L for different ranges of L_{true} for single-point L -fitting from simulated negative feedback approach curves over flat substrates.

Range	$RG = 2$	$RG = 4$	$RG = 10$	$RG = 20$
0.1-10	[-0.9468,0.1005]	[-1.2573,0.1227]	[-0.2888,0.0611]	[-0.2891,-0.0029]
0.1-5	[-0.0981,0.1005]	[-0.0201,0.1227]	[-0.0282,0.0611]	[-0.1166,-0.0029]
0.1-2	[-0.0079,0.0930]	[-0.0201,0.0729]	[-0.0282,-0.0036]	[-0.0414,-0.0029]
0.1-1	[-0.0079,0.0249]	[-0.0201,-0.0041]	[-0.0282,-0.0036]	[-0.0276,-0.0029]
0.1-0.5	[-0.0079,-0.0024]	[-0.0196,-0.0041]	[-0.0211,-0.0036]	[-0.0172,-0.0029]

2.13.2 κ -Fitting over Flat Substrates

Table 2.4: Overview of $|\text{Err } \kappa| < 0.08$ for different ranges of L_{true} for fitting intermediate kinetics approach curves over flat substrates when the experimental negative feedback curve is available (dual-mediator method) and when it is not (single-mediator method).

L_{true}	Method	$RG = 2$	$RG = 4$	$RG = 10$	$RG = 20$
0.1-10	Dual mediator	[-4.30,2.15]	[-2.60,1.70]	[-2.20,1.70]	[-1.70,1.75]
	Single mediator	[-2.10,2.10]	[-2.50,2.35]	[-1.90,2.50]	[-1.50,3.30]
0.1-5	Dual mediator	[-4.15,2.15]	[-2.75,1.70]	[-2.50,1.70]	[-1.85,1.75]
	Single mediator	[-1.80,2.10]	[-2.70,2.35]	[-2.05,2.50]	[-1.65,3.30]
0.1-2	Dual mediator	[-3.55,2.15]	[-2.65,1.70]	[-2.75,1.70]	[-2.05,1.80]
	Single mediator	[-2.00,2.10]	[-2.00,2.35]	[-2.10,2.50]	[-1.85,3.30]

2.13.3 κ -Fitting over Curved Substrates

Table 2.5: Overview of ranges of $|\text{Err } \kappa| < 0.08$ as function of H for fitting approach curves over curved intermediate kinetics substrates for $L_{\text{true}} = [0.1, 1]$ and $W \geq 3$

H -range	Single mediator	Dual mediator
[0,0.6]	[-0.5,0.9]	[-1.5,1.8]
[0,1.0]	[-0.4,0.5]	[-0.9,1.2]
[0,1.4]	[-0.3,0.3]	[-0.5,1.0]
[0,1.8]	[-0.3,0.2]	[-0.3,0.9]
[0,2.2]	[-0.3,0.1]	[-0.2,0.8]
[0,3.0]	[-0.3,0.1]	[-0.1,0.7]

2.13.4 Single-Point κ -Fitting over Curved Substrates

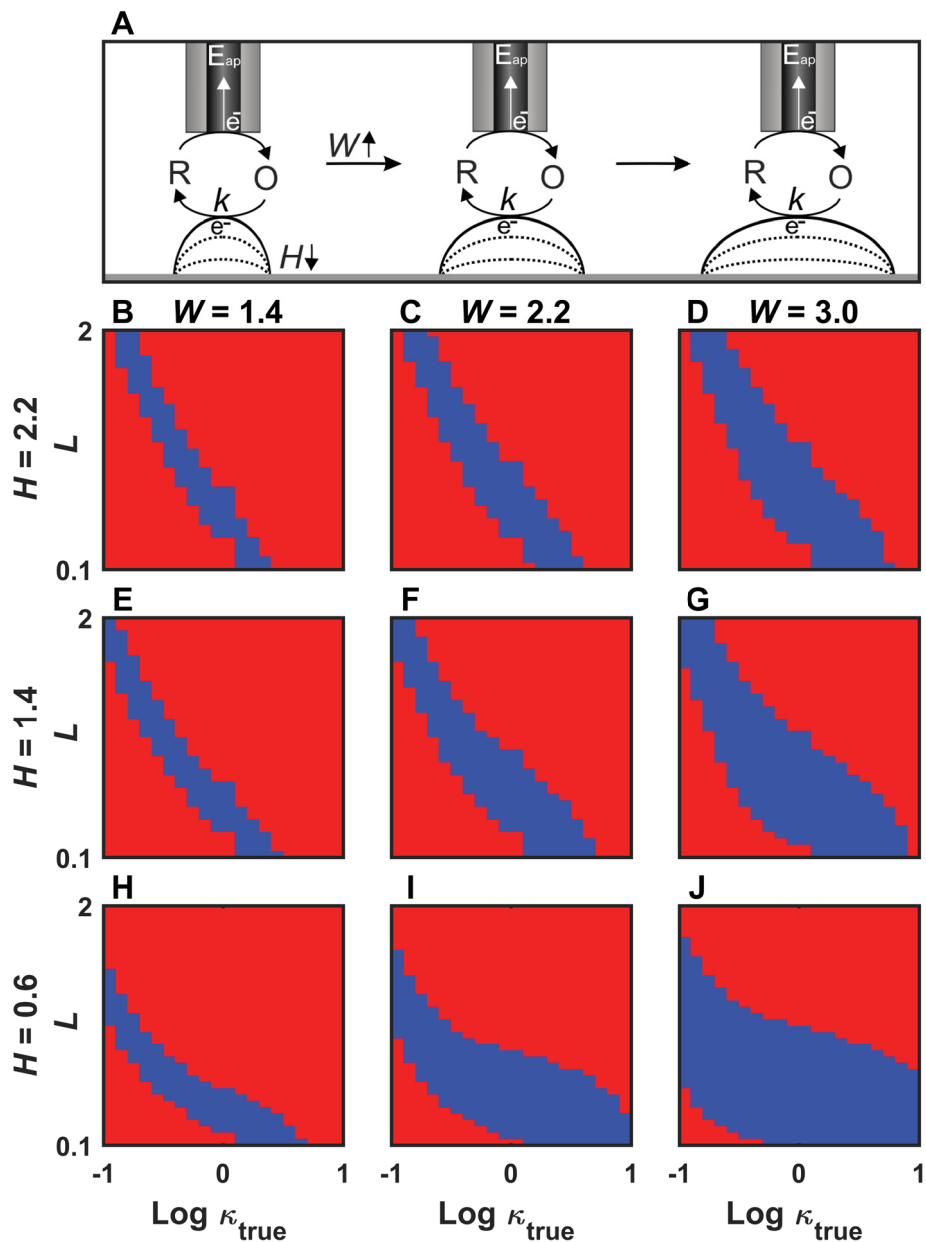


Figure 2.12: **A**: Scheme over intermediate kinetics approach curves over curved substrates. **B-J**: Logic plots for the single-point κ -fitting (with L_{true}) of simulated approach curves over curved substrates ($L_{true} = [0.1, 1]$). Red indicates that $|\text{Err } \kappa| > 0.08$ and blue denotes $|\text{Err } \kappa| \leq 0.08$.

This page is intentionally left blank

Chapter 3

Quantifying MRP1 Transport

Activity of HEK293 and HEKMRP1

Cells

3.1 Contributions

Chapter 3 was written by SS. Zeonor substrates were fabricated by MG. Experimental data was acquired by SS, with the exception of the data presented in Figure 3.5C, which was acquired by NP and SS. Data was treated by SS.

Extraction of kinetic parameters using SECM in feedback mode remains challenging for living cells. Chapter 2 discussed the use of analytical approximations and a dual-mediator method (one for negative feedback and one for intermediate kinetics) to deconvolute topography and surface kinetics, using simulated reference data. In Chapter 3, the FcMeOH/Ruhex dual-mediator method is applied experimentally to assess MRP1 activity in HEK293 and HEKMRP1 cells. The previously reported methodology was successfully reproduced.^{91,92} A crucial discrepancy in the relationship between surface reactivity and tip-to-substrate dis-

tance was identified. A new method was then suggested, which aims towards mitigating topography effects. No contrast between the HEK293 and HEKMRP1 cells was observed.

3.2 Introduction

The effects of protein expression is usually studied by introducing the respective gene into a model cell line. The resulting cell line will have new properties, depending on the functions of the protein. MRP1 overexpressing cell lines, for instance, are multidrug resistant.^{9,11,26} In Chapter 3, the HEKMRP1 and HEK293 cell lines serve as positive and negative controls, respectively, where HEKMRP1 is the MRP1 overexpressing variant of the parental cell line, HEK293. High MRP1 expression in the HEKMRP1 cell line should be ideal for maximizing contrast in MRP1 activity. Common methods for studying protein expression include immunostaining methods like western blotting,^{115,116} immunofluorescence and flow cytometry, and mRNA expression by PCR.

The overexpression of MRP1 can bring about different cellular changes, including changed levels of GSH.⁵⁶ As GSH is transported out of the cell by MRP1, its intracellular concentration is important for its efflux rate and its quantification is required for a simulation model development.⁸⁰ The goal of such a model would consist of attempting to fit a rate constant for the GSH efflux. Assessing the intracellular GSH concentration is therefore critical.

The GSH reductase recycling assay—reported in 1969 by Tietze¹¹⁷—serves as one of the most used and trusted methods for GSH quantification.¹¹⁸ Since glutathione reductase naturally reduces glutathione disulfide, this method finds the total GSH concentration, the sum of GSH and GSH disulfide. The HEK293 and HEKMRP1 cell lines grow at different rates and have a different sizes. Therefore, the GSH quantification needs to be normalized to independent factor. Typical options are cell number and protein content.¹¹⁹ Normalizing to cell

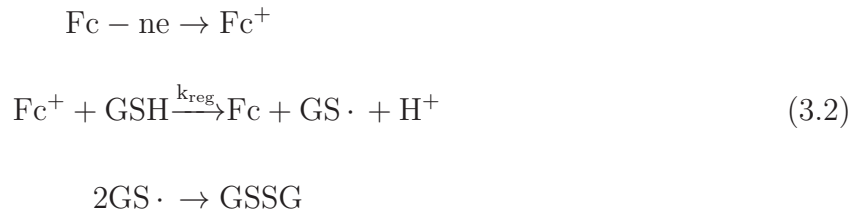
number would be nonideal for different cell lines as their size typically varies. Normalizing to protein content is a commonly used method in experimental biology/biochemistry. Two common methods for quantifying protein in cell lysates are the bicinchoninic acid (BCA)¹²⁰ and the Bradford assay.¹²¹ The problem with these assays is that the response factor for the standard is different than that of the lysate.^{122–124} As a consequence, quantitative protein quantification is difficult and was chosen to be done by dilution series to give relative protein quantification.

In Chapter 3, the MRP1 overexpression will be verified by Western blotting and the effects of MRP1 overexpression on intracellular glutathione levels will be quantified. The dual-mediator feedback method discussed in Chapter 1 and 2 will be applied to assess the MRP1 activity of the HEKMRP1 and HEK293 cell lines. The previously reported dual-mediator method using FcMeOH/Ruhex will be used.^{91,92} Chapter 2 predicts that κ can be accurately fitted over a cell. Experimentally, many adverse effects can influence the results such as electrode fouling effects, presence of interfering redox species and deviation from heterogeneous behaviour. An alternate approach includes comparison to numerical simulations or calibration curves rooted in the EC' -mechanism.

The EC' mechanism is the denotation of the reversible electron transfer at an electrode followed by an irreversible chemical redox process by the formed species in solution, which regenerates R. E is a heterogeneous electron transfer at the electrode surface, C is a chemical reaction undergone by the formed species, and $'$ denotes that this procedure is catalytic (regenerates the reactant at the electrode).



X and Y is a different redox couple in solution. It has been proposed that glutathione is oxidized by ferrocenium derivatives according to the EC' mechanism.⁸⁹



Where Fc is a ferrocene derivatives, GSSG is glutathione disulfide and k_{reg} is the second order homogeneous rate constant for the regeneration of Fc. SECM has been used to find k_{reg} .^{125,126} However, it is not clear how to relate GSH concentration to current at a microelectrode.

3.3 Experimental

All materials were obtained from Sigma-Aldrich used without further purification. Data treatment was done in MATLAB R 2016b®.

3.3.1 Western Blotting

A confluent 75 cm² flask was cooled down on ice before the cells were washed twice with ice cold phosphate-buffered saline (PBS). Then, 400 μL of ice cold RIPA buffer was added and the cells were detached by scraping. The cell suspension was transferred to a tube and agitated for 30 min on ice before it was centrifuged (20 min, 14462g). The protein concentration of the lysate was determined via the Bradford method,¹²¹ using bovine serum albumin (BSA) as standard.

The samples were mixed with Laemmli buffer (Bio-Rad) and boiled for 5 min before 15 μg of protein was loaded (Mini-PROTEAN TGX Precast Gel 7.5%, Bio-Rad). The SDS-PAGE was run at 200 V for 45 min with a Mini-PROTEAN Tetra Cell (Bio-Rad) on with

a precision plus protein dual-color standards ladder (Bio-Rad). The gel was equilibrated for 5 min in transfer buffer before the proteins were transferred to a 0.45 μm nitrocellulose membrane (1 hr, 100 V, Bio-Rad).

The membrane was washed 3 times (5 min) with tris buffered saline with 0.1% Tween (TBST) before it was incubated for 1 hr at room temperature (rt) in blocking solution (3.3% BSA in TBST). The membrane was washed 3 times (5 min) with TBST and cut in half below the 75 kD standard. The top part of the membrane was incubated at overnight in blocking solution at 4 °C with 1:50 Anti-MRP1 antibody [MRPm5] (Abcam, ab24102). The bottom membrane was incubated overnight in blocking solution at 4 °C with 1:500 GAPDH mouse monoclonal antibody (ThermoFisher, 398600). Both membranes were washed 3 times (5 min) with TBST before they were incubated for 1 hr at rt in blocking solution with 1:10000 Goat Anti-Mouse IgG Fc (HRP) (abcam, 97265). The membranes were developed with a Clarity Western ECL Substrate kit (Bio-Rad) and imaged with a ChemiDoc MP System (Bio-Rad). Image treatment was achieved with Image Lab 6.0 (Bio-Rad).

3.3.2 GSH Quantification

Cells ($1.5 \times 10^5 - 5 \times 10^5$) were seeded 2-3 days before GSH quantification in a 6 well plate (CELL+, SARSTEDT). The cells were washed twice with PBS before 500 μL Trypsin/EDTA (2.5 g/L and 1 g/L, respectively) was added. The cells were incubated at rt for 0.5-2 min and then 1000 μL DMEM⁺ was added. The cell suspensions were titrated before they were centrifuged (5 min, 400g), washed twice with PBS and resuspended in 3% 5-sulfosalicylic acid in water (18.2 M Ω). After 3 minutes of vortexing and centrifugation (16000g, 2 min), the supernate was immediately used for the GSH assay.

A solution of 1.68 mM 5,5-dithiobis(2-nitrobenzoic acid) was mixed (50/50) with 3.3 units/mL glutathione reductase). The resulting solution (120 μm) was added to a 96-well plate. The

well plate was tapped for 30 s before 60 μL of 0.8 mM β -nicotinamide adenine dinucleotide 2-phosphate was added. The plate was equilibrated at 30 $^{\circ}\text{C}$ for 2 min before the absorbance was read at 412 nm for 2 min with 30 s intervals. The slopes from linear regression of absorbance versus time were plotted versus sample concentration to give dilution curves. The relative GSH levels were found as the ratio of the slopes of the dilution curves; the slopes of HEKMRP1 were divided by the slopes for HEK293. A calibration curve was generated to ensure that all found slopes were within the linear range.

The precipitated proteins were dissolved in 1000 μL PBS and 10 μL 5 M NaOH (ThermoFisher). The relative protein contents were found using the BCA assay¹²⁰ and normalizing the slopes of dilution series.

3.3.3 SECM Approach Curves Over Cell Layer

Zeonor 1060R slides (2.3 cm in diameter and 0.5 mm in thickness) were fabricated and uniformly treated with oxygen plasma as described previously.⁹² HEK293 cells (3.5×10^5) were seeded on Zeonor slides 2 days before the SECM experiments. The Zeonor slides were then washed with PBS 2 times before it was mounted in the electrochemical cell and 2 mL of imaging solution was added (0.5 mM $\text{Ru}(\text{NH}_3)_6\text{Cl}_3$, 0.5 mM FcMeOH, and 25 mM HEPES in DMEM⁻). The electrode was first positioned over the cells through negative feedback of ruhex reduction. Then, the electrode was retracted 350 μm ($L \approx 100$) in the z-direction, and a 10 s chronoamperometry measurement was performed for FcMeOH at 350 mV. The electrode was then moved down 350 μm and an approach curves was preformed at 350 mV at 0.5 $\mu\text{m s}^{-1}$ (12 μm in total). Another approach curve was performed for ruhex at -350 mV by retracting the electrode 12 μm at an approach speed of 0.5 $\mu\text{m s}^{-1}$. The electrode was again retracted 350 μm in the z-direction, and a 10 s chronoamperometry measurement was performed for Ruhex at -350 mV. This procedure was repeated eight times at different locations.

3.3.4 Electrochemical Measurements

Electrochemical measurements were carried out in PBS, unless otherwise noted. Electrode sizes, materials and geometries are reported in their respective captions. In-house fabricated Ag/AgCl reference electrodes were used. SECM measurements were performed on an ELP 3 instrument (HEKA, Germany). In the cases where the electrode was positioned close to the surface, the tip-to-substrate distance was found by two methods. The electrode was either crashed into the substrate to find an inflection point approximating L_0 , or the probe was moved until the current reached 60% or 75% of that in bulk solution and L was calculated during the experiment.

3.4 Effects of MRP1 Overexpression

High MRP1 expression in the HEKMRP1 cell line is ideal for maximizing contrast in MRP1 activity. The overexpression of MRP1 was verified by western blotting (Figure 3.1A). Although MRP1 is expressed to some extent in most tissue, no detectable amount of MRP1 was found in the HEK293 cell line. The relative intracellular GSH concentration of HEKMRP1 to HEK293 was found to be 0.43 ± 0.06 (95% CL, $n = 9$) normalized to relative protein amount. Figure 3.1B shows an example of a dilution curve for the GSH assay. The dilution curves show high linearity and the calibration curve (Figure 3.1C) shows a linear range between 0.23 and 0.0096 min^{-1} . All values used in the GSH quantification fall within this range. For the quantification of GSH, the HEKMRP1 lysates were about double the concentration than HEK293 to avoid any systematic error arising from the high difference in GSH concentration.

Higher inherent efflux of GSH is expected in the HEKMRP1 cell line. If the efflux rate of GSH is dependent on its intracellular concentration, lowered GSH levels in the HEKMRP1 cell line can reduce contrast between the cell lines for the inherent GSH efflux. Contrast between the cell lines can be increased by treatment with the cardiovascular drug, verapamil.³³

This drug preferentially causes GSH efflux by MRP1. Higher extracellular concentration can make its electrochemical detection easier.

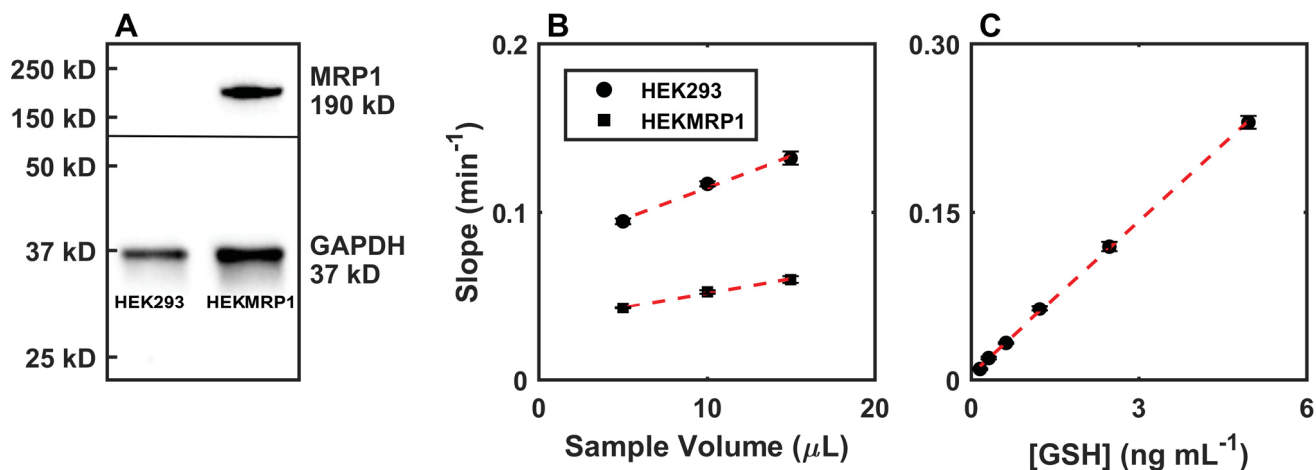


Figure 3.1: **A**: Western blot showing the MRP1 overexpression of the HEKMRP1 cell line relative to the parental cell line, HEK293. **B**: Example of dilution curves for the GSH quantification for HEK293 (circle, $R^2 = 0.988$) and HEKMRP1 (Square, $R^2 = 0.993$). The slope—calculated from linear regression of absorbance (412 nm) versus time in a GSH enzymatic recycling assay—is plotted versus volume of cell lysate. **C**: Calibration curve of the GSH assay ($R^2 = 1.000$), which shows a linear slope range between 0.23 and 0.0096 min^{-1}

3.5 Applying the Feedback Method

To assess the MRP1 activity of the two cell lines with the feedback method, SECM maps were acquired with the FcMeOH/Ruhex dual-mediator method. The data processing is exemplified with an image acquired $\approx 20 \mu\text{m}$ over a HEKMRP1 cell. From the Ruhex current map (Figure 3.2A), single-point topography fitting was used to obtain a topography profile (Figure 3.2B). This topography profile was then used together with the FcMeOH current map (Figure 3.2C) to fit for κ_{eff} (Figure 3.2D). The SECM imaging and kinetic extraction was deemed successful.

During SECM imaging of the HEK cell lines, it was found that the cell topography varied enough that a fixed imaging height could not be used. Instead, the imaging height was determined for each case with ruhex line scans. Similarly, κ_{eff} was found to vary substantially as well. Figure 3.3 shows two example maps with high variance in the fitted κ_{eff} , 0.11 and 0.39. The width of the cells were around $20 \mu\text{m}$ ($W \approx 6$), which falls within the accurate range, assuming that the fitting error does not increase with increased width. The minimum L_{eff} in the images, corresponding to the cell apex, varied substantially too, $L_{\text{eff}} = 1.26, 0.14$, respectively. For infinite substrate behaviour, the absolute difference in L_{eff} corresponds to $\approx 3.9 \mu\text{m}$. It is thought that differences in topography affect κ_{eff} . Consequently, the κ - L -relationship needs to be evaluated further.

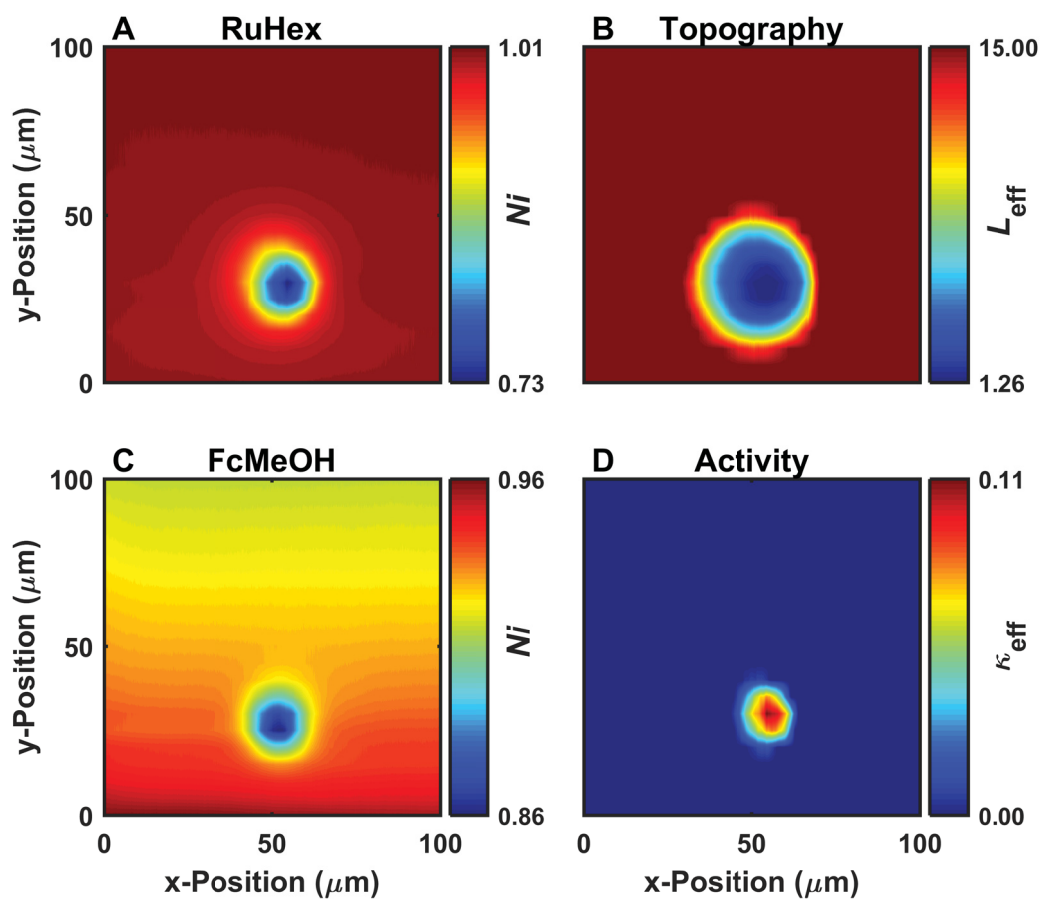


Figure 3.2: Parameter extraction from SECM current maps over a HEKMRP1 cell at a constant height of $20 \mu\text{m}$. The dimensions were $100 \times 100 \mu\text{m}$, with an imaging time of less than 6 min per map. The imaging solution consisted of 1 mM FcMeOH and $\text{Ru}(\text{NH}_3)_6\text{Cl}_3$ (ruhcx) in DMEM^- . A carbon fiber microelectrode was used ($a = 3.5 \mu\text{m}$, $RG = 2.8$). **A**: Normalized ruhcx current map (acquired at $-350 \text{ mV Vs. Ag/AgCl}$). **B**: Topography profile extracted by fitting each point in **A** to the negative feedback analytical approximations.⁷² **C**: Normalized FcMeOH current map (acquired at $300 \text{ mV Vs. Ag/AgCl}$). **D**: Extracted activity profile from the topography profile in **B** and FcMeOH current map in **C**.

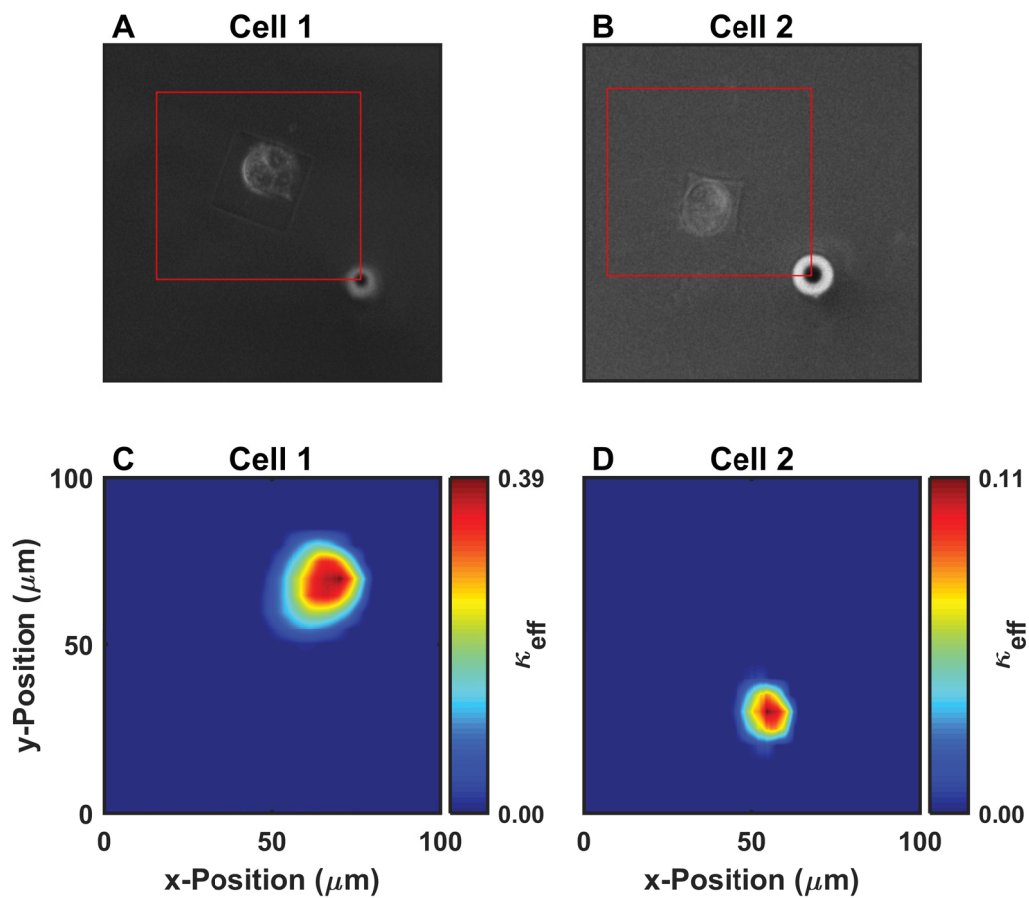


Figure 3.3: **A-B**: Optical micrographs of imaged HEKMRP1 cells. The red inset denotes $100 \times 100 \mu\text{m}$ **C-D**: Extracted activity profiles from SECM current maps of FcMeOH and ruhex. A carbon fiber microelectrode was used ($a = 3.5 \mu\text{m}$, $RG = 2.8$).

3.6 Evaluating the Feedback Method

To reduce the effect of varying topography in the assessment of the κ - L -relationship, a series of approach curves were recorded with the dual-mediator system over a layer of HEK293 cells (Figure 3.4A). A clear current difference is observed, showing the noninsulating behaviour of the HEK293 cells towards FcMeOH⁺. Figure 3.4B shows L_{eff} , found by the single-point fitting of the ruhex approach curve, plotted versus recorded electrode position during the experiment. The high linearity indicates accurate L -fitting. The approach curve sets were subjected to the single-point κ -fitting (Figure 3.4C). The experimental variance of κ_{eff} with L_{eff} greatly exceeds the expected error for the flat substrate case in Chapter 2. In the case of an ideal topography normalization, a plot of k_{eff} versus L_{eff} would yield a straight line with no slope and $R^2 = 0$. The clear deviation of this behaviour indicates that the irregular topography of the HEK cell lines cannot be accurately accounted for. One of the possible

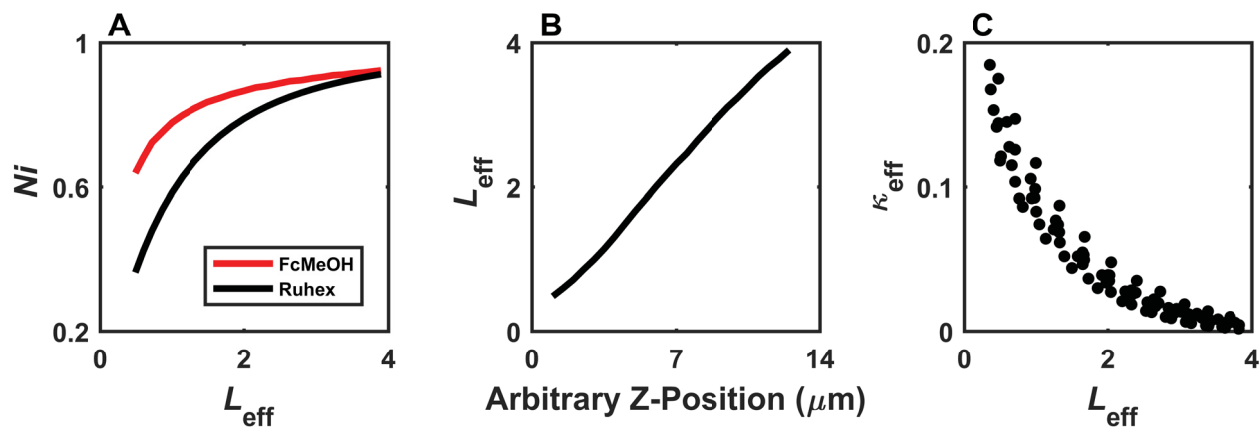


Figure 3.4: **A**: Example approach curves for the oxidation of 0.5 mM FcMeOH (red, dashed line) and the reduction of 0.5 mM ruhex (black, solid line) over a layer of HEK293 cells. A carbon fiber electrode with $a = 3.5 \mu\text{m}$ and $RG = 5$ was used. The applied potentials were 300 mV and -350 mV against Ag/AgCl, respectively. **B**: Plot of L_{eff} versus arbitrary z-position, linear regression yielded $R^2 = 0.996$. L_{eff} was found by single-point fitting of the ruhex approach curve in **A** to the negative feedback analytical approximations.⁷² **C**: Plot of κ_{eff} versus L_{eff} , for eight sets of approach curves. κ_{eff} was calculated with the single-point fitting to the first order heterogeneous kinetics analytical approximation,⁷³ using the respective L_{eff} .

explanations for the high variance of κ_{eff} could be the cell permeability of FcMeOH, which gives a similar effect on approach curve shape.⁸³ A new approach is therefore needed.

3.7 The EC' Model for GSH Detection with FcMeOH

Alternatively, the regeneration of FcMeOH can be viewed as an EC' mechanism as previously described in Section 3.2. GSH efflux would give rise to a detectable concentration of GSH in the extracellular environment. Previous studies of cellular flux have directly recorded

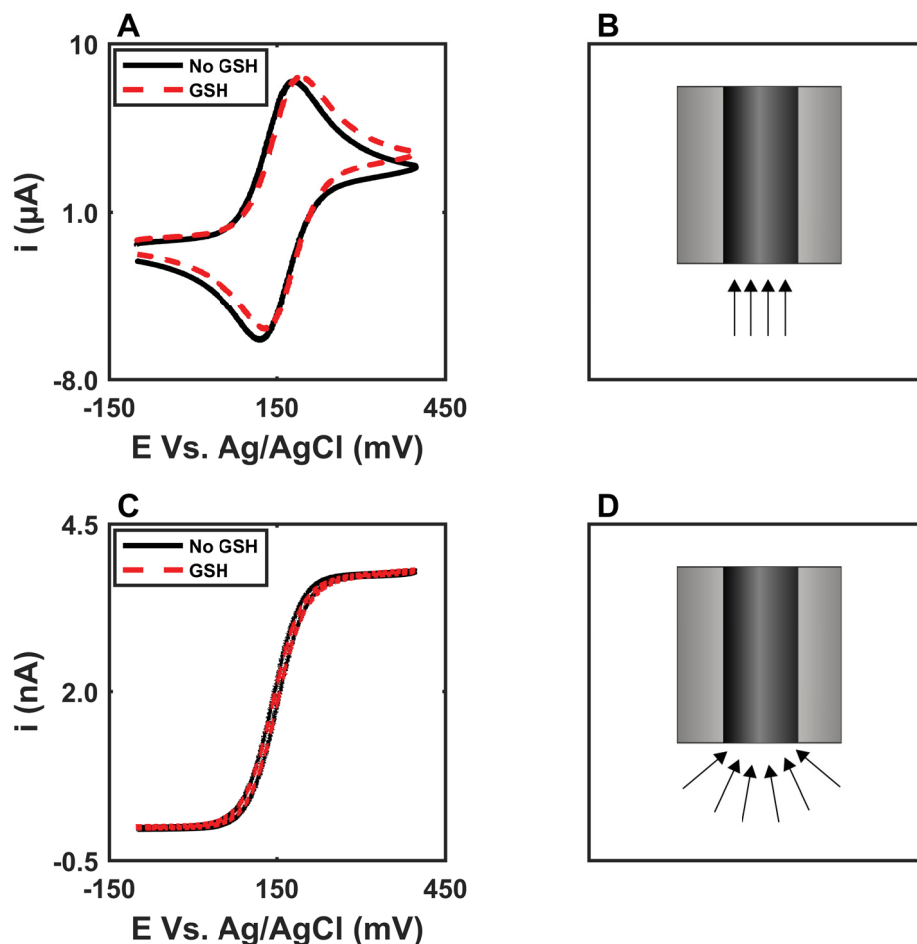


Figure 3.5: **A:** Macro (2 mm glassy carbon electrode) CV of 1 mM FcMeOH with (red, dashed line) and without (black, solid line) 3 mM GSH. The scan rate was 25 mV/s. **B:** Scheme of linear mass transport. **C:** Micro (Pt, $a = 12.5 \mu\text{m}$) CV of 1 mM FcMeOH with (red, dashed line) and without (black, solid line) 5 mM GSH. **D:** Scheme of hemispherical mass transport. The scan rates were 25 mV/s and the first cycle is shown.

the redox mediator concentration far enough from the cells to avoid topography contributions.^{78–80} To assess if this approach is feasible for the EC' -model, Cyclic voltammetry (CV) measurements were recorded of FcMeOH in bulk solution with a macro- and micro-electrode. A substantial increase in peak current is observed on the macro scale when the solution is spiked with GSH (Figure 3.5A). On the contrary, no increase in steady state current is observed on the microscale (Figure 3.5C). As mass transport is substantially faster to an electrode of this size (Figure 3.5B and D), the regeneration process seems to be overshadowed. This approach is therefore not possible.

When a microelectrode is moved close to a surface, mass transport is hindered (negative feedback). Reducing mass transport could enhance the relative current increase, occurring when the solution is spiked with GSH. Inconsistent results were found for high GSH concentrations (not shown). However, for a lower concentration of both GSH and FcMeOH,

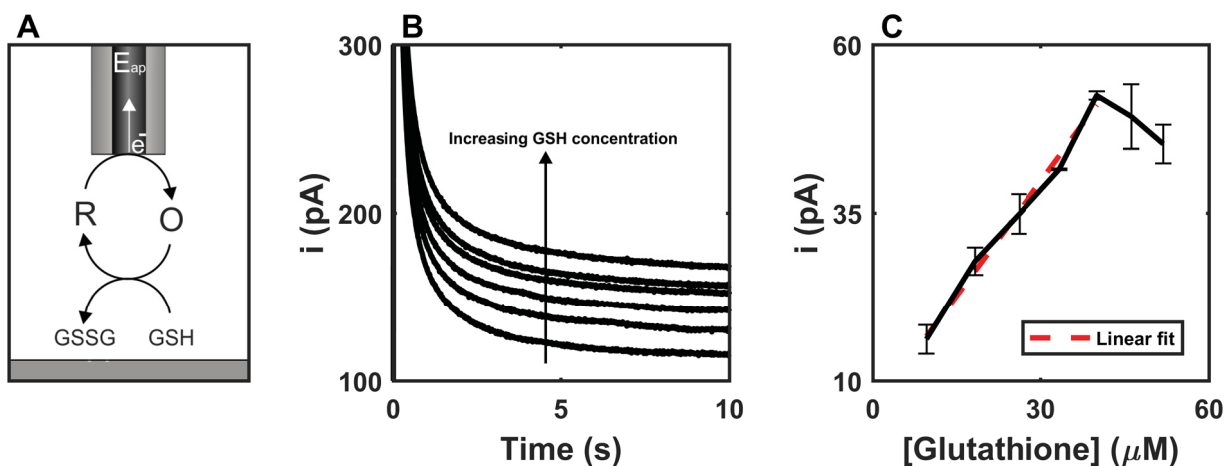


Figure 3.6: **A**: Scheme of the EC' mechanism. **B**: Chronoamperograms of $50 \mu\text{M}$ FcMeOH continuously spiked with GSH. A platinum electrode was used ($a = 12.5 \mu\text{m}$, $RG = 3$) and positioned at a height of $\approx 10.4 \mu\text{m}$ over the Zeonor substrate. **C**: Plot of steady state currents from the chronoamperograms in **B** versus GSH concentration and linear fit (red, dashed line) to the linear region ($R^2 = 0.989$).

a linear region was found with chronoamperometry (Figure 3.6). When the solutions were not degassed, large concentrations of GSH caused substantial electrode fouling (Figure 3.9). This could also be the reason for the lack of current increase in Figure 3.5.

3.8 Regeneration of Other Ferrocene Derivatives

The regeneration by GSH is observed for other ferrocene derivatives (Figure 3.7). FcCOOH for instance, has an even higher capability than FcMeOH to be regenerated by GSH (Fig-

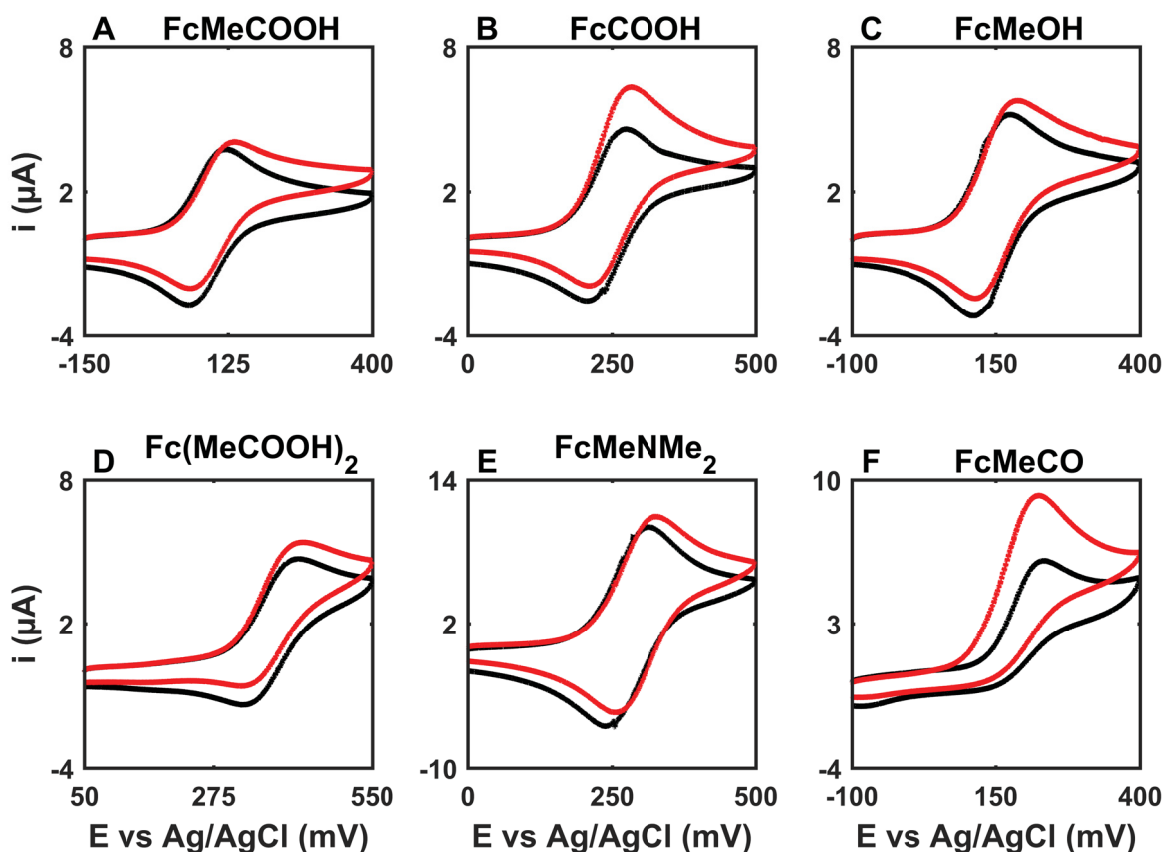


Figure 3.7: Cyclic voltammograms of different redox mediators at 1 mM concentration before and after being spiked with GSH to 1 mM. The electrode was a 2 mm glassy carbon electrode. **A:** Ferroceneacetic acid. **B:** Ferrocenecarboxylic acid. **C:** Ferrocene methanol. **D:** 1,1'-Ferrocenedicarboxylic acid. **E:** (Dimethylaminomethyl)ferrocene. **F:** Ferrocenecarboxylic acid

ure 3.7B). Using a ferrocene derivative that is cell impermeable would be advantageous as no current contribution would arise from flux through the cell membrane. Charged redox mediators typically have drastically reduced cell membrane permeability. FcCOOH, Fc(COOH)₂, FcMeNMe₂ and FcMeCOOH are examples of redox mediators which would be expected to be cell impermeable. FcCOOH was not used due to its light sensitivity, which prevents FcMeOH oxidation and causes precipitation on the electrode surface (Figure 3.8, appendix). Fc(COOH)₂, FcMeNMe₂ did not shows ideal behaviour on the micro scale (not shown). FcMeCOOH, however, was included in the application of the chronoamperometry method.

3.9 Applying the Chronoamperometry Method

While applying the feedback method to a layer of HEK293, it was found that the cell layer behaves approximately as a flat substrate and gives a negative feedback response. The best way of dealing with varying topography would be to position the electrode at a constant height over a layer of cells. The cell layer will not be completely flat, but it should be more reproducible than trying to position it over a single cell; lateral diffusion from around the cell contributes to the normal flux of species. To asses if the chronoamperometry method can be used to assess MRP1-mediated GSH efflux, a response factor is defined.

$$R_f = \frac{Ni_{Fc}}{Ni_{Ru}} \quad (3.3)$$

Where Ni_{Fc} and Ni_{Ru} are normalized ferrocene derivative and Ruhex currents close to the surface, respectively. This new parameter is hard to interpret quantitatively because of the normalization; however, it should serve as a guide to see if there is contrast between the cell HEK293 and HEKMRP1 cell lines.

The morphology of a cell can change drastically during the course of an SECM experiment because of cell stress (Figure 3.10). By performing chronoamperometry instead of imaging, experimental time is reduced from about 12 min to 1-2 min per measurement. Also, the drastically reduced acquisition time reduces fouling effects.

The chronoamperometry method was applied to layers of HEK293 and HEKMRP1 cells. The results can be found in Table 3.1. Three redox mediators were tested, FcMeOH, FcMeCOOH, and Fc(MeOH)₂. No increase in R_f was found for the HEKMRP1 cells. Interestingly, R_f is similar for the two cell lines, although slightly higher for the HEK293 cells. This might be due to other reducing compounds on or in vicinity of the cells, which are present in higher concentrations in the HEK293 cells. For instance, reducing proteins in the cell membrane.

Table 3.1: R_f found by performing chronoamperometry measurements over layers of HEK293 and HEKMRP1 layers at a height of $\approx 6 \mu\text{m}$. A carbon fiber electrode was used ($a \approx 3.5$ and $RGs = 4-6$). The uncertainty is reported as confidence intervals at 95% CL

Mediator	Concentration	HEK293	HEKMRP1
Fc(MeOH) ₂	0.5 mM	1.077 (± 0.001 , $n = 9$)	1.069 (± 0.001 , $n = 14$)
FcMeCOOH	0.5 mM	1.065 (± 0.001 , $n = 17$)	1.062 (± 0.001 , $n = 9$)
FcMeOH	0.5 mM	1.155 (± 0.001 , $n = 20$)	1.154 (± 0.001 , $n = 20$)
FcMeCOOH	25 μM	1.119 (± 0.001 , $n = 17$)	1.097 (± 0.001 , $n = 23$)

3.10 Conclusions

The feedback method was successfully applied to the HEK cell lines. Due to the high variance found in κ_{eff} , approach curve experiments were carried out to shed further light on the κ - L -relationship. It was found that the feedback method is not able to account for the varying topography of the HEK cell lines. A new method based on the EC'-mechanism was

developed, which did not find any higher response from the positive versus the negative control. The exact contributions to the regeneration of ferrocene derivatives remains unclear. Other species originating from the cell or produced oxygen species might be contributors. Other methods such as AC-SECM, SECM-AFM, IC-SECM, and shearforce could also circumvent the topography issue.

Although contrast is seen in the calcein-AM activity assay,⁹³ it is not clear if this is the case for GSH. The Tietze method used to find intracellular GSH concentrations can also be used to quantify the extracellular concentration,⁶² which would represent the inherent GSH efflux. A better approach could be to treat the cells with verapamil, which depletes GSH through MRP1-mediated efflux. GSH depletion would give a much higher extracellular concentration than observed inherently, making it's detection easier.

3.11 Appendix

3.11.1 Light Sensitivity of FcCOOH

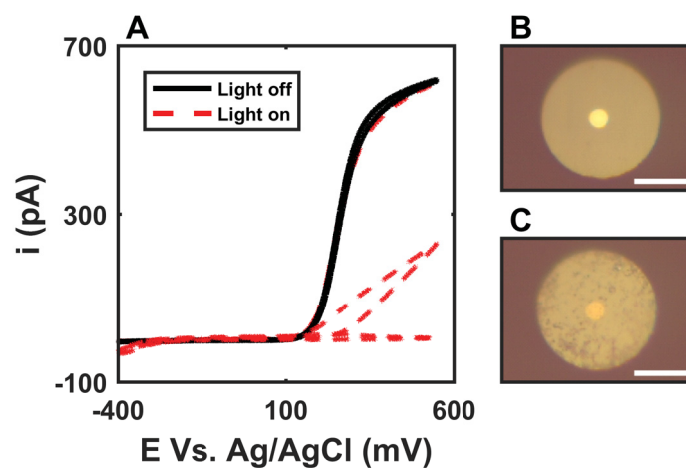


Figure 3.8: **A**: Cycle 1-3 of CVs of 1 mM FcCOOH with (red, dashed line) and without (black, solid line) light on. A carbon fiber microelectrode was used ($a = 3.5 \mu\text{m}$, $RG = 6$). The scan rate was 25 mV/s. **B-C**: Optical micrographs of the carbon fiber microelectrode before and after the CVs, respectively. Substantial electrode fouling is observed after the CVs.

3.11.2 Electrode Fouling in the Presence of GSH

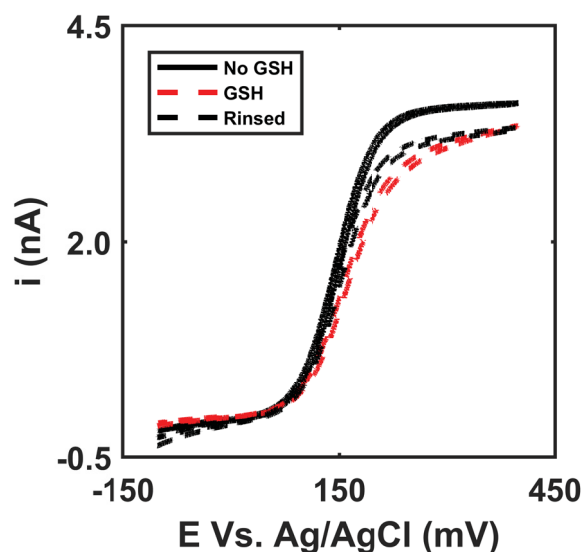


Figure 3.9: Cycle 1 of CVs of 1 mM FcMeOH without (black, solid line) and with 5 mM GSH (red, dashed line). The electrode was rinsed and placed in a new solution of FcMeOH without GSH, to ensure that the current drop is a result of electrode fouling (black, dashed line). A platinum microelectrode was used ($a = 12.5 \mu\text{m}$, $RG = 3$). The scan rate was 20 mV/s.

3.11.3 Current Stability in SECM Imaging

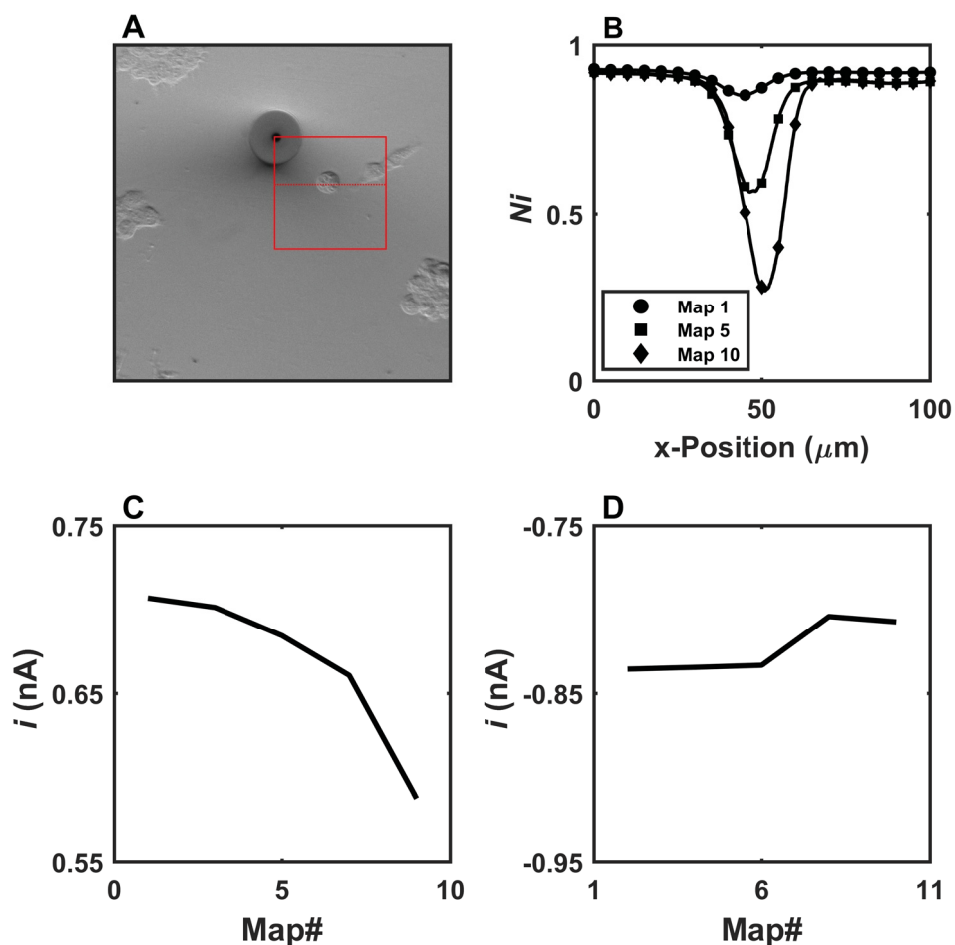


Figure 3.10: **A:** Optical micrograph of a HEK293 cell that was continuously imaged with SECM. The SECM imaging area was $100 \times 100 \mu\text{m}$ and the imaging time was less than 6 min per image. Current maps were continuously recorded over the cell alternating between FcMeCOOH (350mV vs Ag/AgCl) and ruhex (-350 mV) as redox mediator (10 maps in total). **B:** Lines scans from the ruhex maps. **C,D:** Change in steady-state currents in bulk solution for FcMeCOOH and ruhex, respectively.

3.11.4 Western Blotting Solutions

RIPA buffer: 150 mM NaCl, 0.1% SDS (Bio-Rad), 1% Sodium deoxycholate, 1% Triton X-100 (Bio-Rad), 25 mM Tris-HCl 0.5 M pH 6.8 (Bio-Rad), 1% Halt Protease and Phosphatase Inhibitor Cocktail, EDTA-free (ThermoFisher).

Transfer buffer: 50 mM tris (Bio-Rad), 40 mM glycine (MP Biomedicals), 0.04% SDS (Bio-Rad), 20% MeOH

Running buffer: 25 mM Tris (Bio-Rad), 0.2 M Glycine (MP Biomedicals), 0.1% SDS (Bio-Rad)

TBST buffer: 10% 10x Tris Buffered Saline (TBS, Bio-Rad) 1 mL Tween 20 (Bio-Rad)

Chapter 4

Conclusions and Future Work

4.1 Summary and Contributions to Original Knowledge

In Chapter 2, the previously reported single-point κ and L -fitting methods were validated. Such methods improved electrode positioning, increase the spatial resolution of κ -fitting and alleviate the need to find L by external means. It has been shown that when the substrate shows negative feedback, L can be fitted from a single point with the negative feedback analytical approximation. This implies that in many cases, crashing the electrode is unnecessary when positioning the electrode because L can simply be calculated. Secondly, if a reactive feature is surrounded by a surface displaying negative feedback, κ can accurately be fitted to the analytical approximations in the horizontal plane. The tip-to-substrate distance can be calculated on either side of the reactive feature, which can then be extrapolated to back out the entire L -profile. Once this L -profile is known, the current in the reactive region can be used to fit κ . This method aims towards taking full advantage of the spatial resolution available with SECM. Simultaneously, it can be assessed if the reactive feature is large enough to display infinite substrate behaviour.

More generally, it was shown through numerical simulations that the single-point κ -fitting is possible without any knowledge of L with a dual-mediator system, where one redox mediator shows negative feedback behaviour regardless of surface kinetic. This is possible when the surface preferentially does not regenerate one redox mediator or when the negative feedback redox mediator behaves irreversibly (*e.g.* anthracene¹⁰⁷).

In Chapter 3, it was shown that the HEK293 and HEKMRP1 cell lines can be patterned and imaged with SCEM. The FcMeOH/Ruhex system in SECM feedback mode was applied to assess MRP1 transport activity of GSH in the HEK293 and HEKMRP1 cell lines. Surprisingly, a high variance in κ and L was found when imaging single/small clusters of cells. When the κ - L -relationship was further investigated by approach curve experiments, issues with the topography normalization was found. A new method rooted the EC' -mechanism was developed; yet, no contrast was found between the HEKMRP1 and HEK293 cells. Other contributors to the regeneration of the ferrocene derivatives could be reducing sugars, reactive oxygen species in the extracellular environment, and/or uneven cell density.

4.2 Future Works

In Chapter 2, the simulation data had small associated errors and were not subject to interferences observed in physical experiments. Examples of experimental interferences include electrode fouling effects, presence of interfering redox active species, and electrode position errors. The effects on accuracy of the studied method is uncertain and needs to be evaluated experimentally. Recently, we published a study where surface reactivity was spatially controlled by depositing a SiO₂ layer over a conducting gold surface.¹²⁷ These substrates can be fabricated with high precision and a variety of different feature shapes and sizes. (Figure 4.1). The κ -fitting of approach curves and line scans can be compared over these substrates. Conductors with a large surface area relative to the electrode typically show pos-

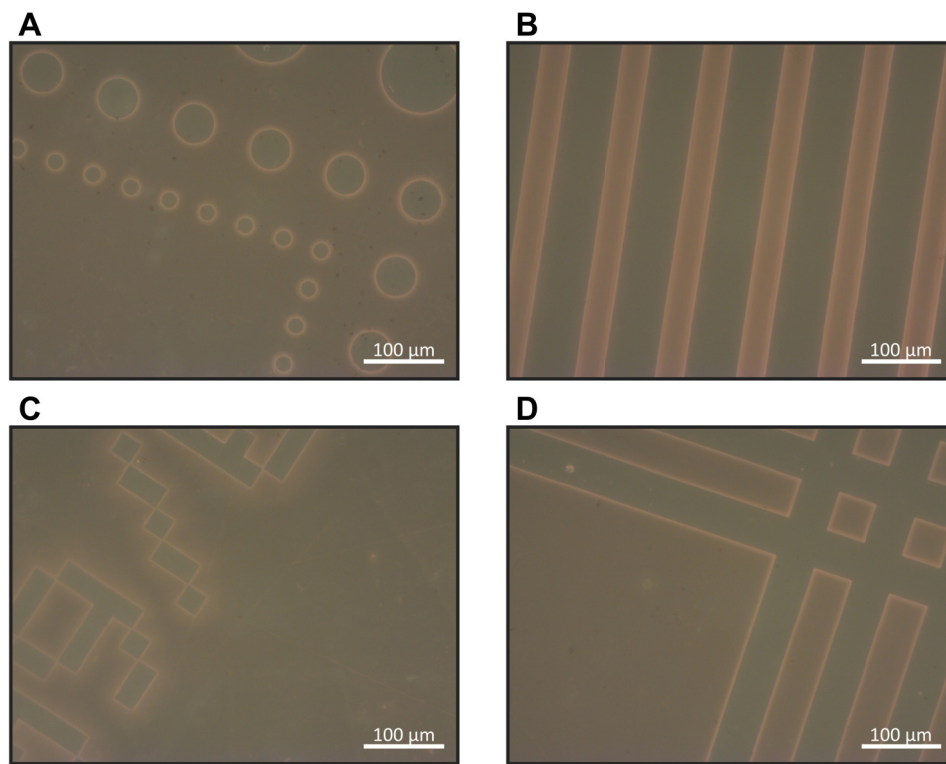


Figure 4.1: Optical micrographs of a Au/SiO₂ substrate. **A**: Circles. **B**: Lines. **C**: Numbers. **D**: Intersecting lines.

itive feedback behaviour. If the kinetics of the substrates is too large, it can be dampened by a self-assembled thiol monolayer.¹²⁸ Since a conductor behaves as a bipolar electrode, the rate of regeneration at its surface is dependent on the exposed surface area.¹²⁹ Exposing only one gold feature could dampen the electrochemical activity without chemically blocking it. This can be done by punching μm -sized holes in a PDMS membrane,¹³⁰ which covers the remaining features.

As seen in Chapter 3, the irregular topography of cells can make quantitative measurements challenging. These challenges could also be met by using constant distance measurements such as shearforce^{96–98} or AFM¹⁰⁶ instead of the FcMeOH/Ruhex system. These methods

keep the microelectrode at a constant distance from the cell and increased current should be observed with higher extracellular GSH concentrations. The lack of contrast could also be due to low inherent transport activity of GSH by MRP1,^{33,38,60} despite the substantially lowered intracellular concentration of GSH in the HEKMRP1 cell line. Quantification of extracellular glutathione levels could shed further light on the inherent GSH efflux, which is possible with the GSH reductase recycling assay.^{62,117} Treating cells with verapamil causes MRP1-mediated GSH efflux. Inducing GSH efflux with verapamil is a promising method for better electrochemical detection due to the higher GSH concentrations. Inhibition of MRP1 has been shown to decrease this efflux.³³ Quantifying the GSH flux can be used to study the inhibition process. Cellular efflux has been shown to fit a constant flux model⁷⁸⁻⁸⁰ (Figure 4.2A and B), as represented by Equation 4.1.

$$C(x, t) = \frac{2f}{D} \left[\left(\frac{Dt}{\pi} \right)^{0.5} \exp \left(\frac{-x^2}{4Dt} \right) - \frac{x}{2} \operatorname{erfc} \left(\frac{x}{2(Dt)^{0.5}} \right) \right] \quad (4.1)$$

Where C is concentration of species of interest, x is distance from surface, f is flux from surface, D is diffusion coefficient, t is time and erfc is the complementary error function.

$$\operatorname{erfc} = 1 - \frac{2}{\pi^{0.5}} \int_0^x e^{-y^2} dy \quad (4.2)$$

The degree of inhibition is described by the Hill equation.^{131,132}

$$f = f_{\max} \frac{1}{1 + \left(\frac{IC_{50}}{[I]} \right)^n} \quad (4.3)$$

Where f_{\max} is the flux with no inhibition, IC_{50} is the concentration of inhibitor causing a 50% reduce in flux, $[I]$ is the inhibitor concentration and n is the Hill coefficient.

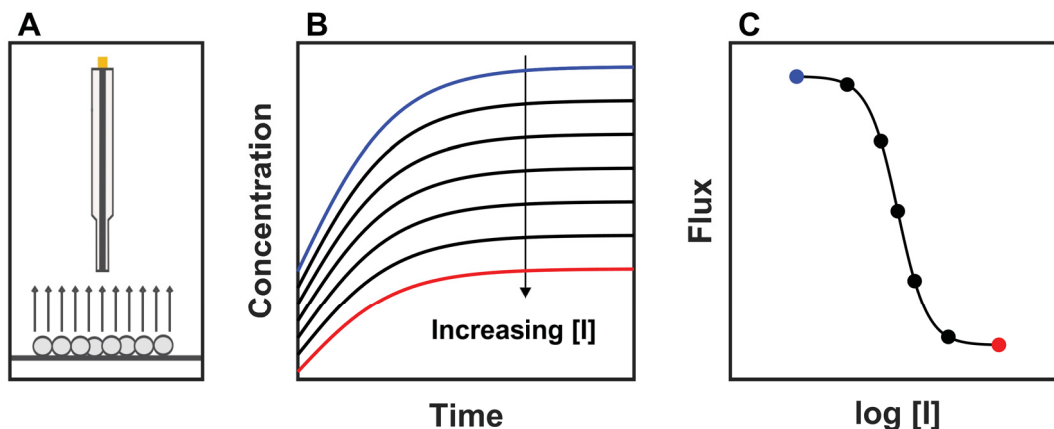


Figure 4.2: **A**: Scheme of linear, constant mass transport from a cell monolayer. **B**: Current versus time plots for the detection of a constant flux from a cell. **C**: Dose-response curve for the inhibition of cellular efflux.

Treating cells with different inhibitor concentrations—called a dose-response curve (Figure 4.2C)—can be used to extract IC_{50} , a common parameter in biology.

Numerous studies of the electrochemical detection of glutathione have been reported.¹³³ For instance, catechols have been used instead of FcMeOH to quantify GSH.^{134,135} There are many methods for the direct GSH detection: mercury¹³⁶ and mercury amalgam,¹³⁷ gold,¹³⁸ and modified carbon electrodes (*e.g.* ferrocene derivatives^{139–141}). Although there are examples of GSH detection with microelectrodes,¹⁴² macroelectrodes are typically used. If the surface of a microelectrode can be modified for GSH detection, the increased mass transport observed on the micro scale should improve the sensitivity. Alternatively, surface confinement of ferrocene moieties at the microelectrode surface will mitigate the effect of mediator permeability in cells and reductive components in the plasma membrane.

Quantitative SECM remains challenging for substrates that are not ‘ideal’, that is, they are not flat, infinite, or perfectly aligned with the electrode. Analytical approximations that simplify data treatment of kinetic extraction^{71–73} are not always accurate in such cases.¹⁴³ Many methods have been used to tackle SECM studies over non-ideal substrates. SECM

instruments usually have built-in methods for slope correction and certain stages can correct electrode-substrate misalignment. For integrated slope correction, the electrode is moved incrementally in the respective dimension that is being corrected for during the scan. No analytical approach exists for kinetic extraction over substrates that do not show non-infinite behaviour or steep curvature, relative to the probe size. Therefore, comparison to numerical simulations is necessary in such cases.^{114,144} However, it is possible to establish the conditions in which the analytical approximations can still be used, as shown in this thesis. Although there are many constant-distance modes in SECM, they are not used for quantitative kinetic extraction because the absolute tip-to-substrate distance is not always known.⁹⁷ It was also shown that dual-mediator systems that deconvolute negative and intermediate kinetic behaviour are a promising way of tackling the challenges of quantitative SECM.^{91,92} Using dual-mediator systems in conjunction with constant distance instrumentation can be a powerful tool in quantitative Bio-SECM studies where substantial curvature makes kinetic extraction difficult.

References

- (1) Szakács, G.; Paterson, J. K.; Ludwig, J. A.; Booth-Genthe, C.; Gottesman, M. M. Targeting multidrug resistance in cancer. *Nature Reviews Drug Discovery* **2006**, *5*, 219.
- (2) Taniguchi, K.; Wada, M.; Kohno, K.; Nakamura, T.; Kawabe, T.; Kawakami, M.; Kagotani, K.; Okumura, K.; Akiyama, S.-i.; Kuwano, M. A Human Canalicular Multispecific Organic Anion Transporter (cMOAT) Gene Is Overexpressed in Cisplatin-resistant Human Cancer Cell Lines with Decreased Drug Accumulation. *Cancer Research* **1996**, *56*, 4124–4129.
- (3) Galluzzi, L.; Senovilla, L.; Vitale, I.; Michels, J.; Martins, I.; Kepp, O.; Castedo, M.; Kroemer, G. Molecular mechanisms of cisplatin resistance. *Oncogene* **2012**, *31*, 1869.
- (4) Masuda, H.; Ozols, R. F.; Lai, G.-M.; Fojo, A.; Rothenberg, M.; Hamilton, T. C. Increased DNA Repair as a Mechanism of Acquired Resistance to cis-Diamminedichloroplatinum(II) in Human Ovarian Cancer Cell Lines. *Cancer Research* **1988**, *48*, 5713–5716.
- (5) Keppler, D. In *Drug Transporters*, Fromm, M. F., Kim, R. B., Eds.; Springer Berlin Heidelberg: 2011, pp 299–323.
- (6) Zhou, S.-F.; Wang, L.-L.; Di, Y. M.; Xue, C. C.; Duan, W.; Li, C. G.; Li, Y. Substrates and inhibitors of human multidrug resistance associated proteins and the implications in drug development. *Current Medicinal Chemistry* **2008**, *15*, 1981–2039.
- (7) Endicott, J. A.; Ling, V. The biochemistry of P-glycoprotein-mediated multidrug resistance. *Annual Review of Biochemistry* **1989**, *58*, 137–171.
- (8) Austin Doyle, L.; Ross, D. D. Multidrug resistance mediated by the breast cancer resistance protein BCRP (ABCG2). *Oncogene* **2003**, *22*, 7340.
- (9) Borst, P.; Evers, R.; Koel, M.; Wijnholds, J. A Family of Drug Transporters: the Multidrug Resistance-Associated Proteins. *Journal of the National Cancer Institute* **2000**, *92*, 1295–1302.

- (10) Cole, S. P. C.; Bhardwaj, G.; Gerlach, J. H.; Mackie, J. E.; Grant, C. E.; Almquist, K. C.; Stewart, A. J.; Kurz, E. U.; Duncan, A.; Deeley, R. G. Overexpression of a transporter gene in a multidrug-resistant human lung cancer cell line. *Science* **1992**, *258*, 1650–1654.
- (11) Cole, S. P. Targeting Multidrug Resistance Protein 1 (MRP1, *ABCC1*): Past, Present, and Future. *Annual Review of Pharmacology and Toxicology* **2014**, *54*, 95–117.
- (12) Cole, S. P. C. Multidrug Resistance Protein 1 (MRP1, *ABCC1*), a “Multitasking” ATP-binding Cassette (ABC) Transporter. *Journal of Biological Chemistry* **2014**, *289*, 30880–30888.
- (13) Johnson, Z. L.; Chen, J. Structural Basis of Substrate Recognition by the Multidrug Resistance Protein MRP1. *Cell* **2017**, *168*, 1075–1085.e9.
- (14) Wijnholds, J.; Evers, R.; van Leusden, M. R.; Mol, C. A. A. M.; Zaman, G. J. R.; Mayer, U.; Beijnen, J. H.; Valk, M. V. D.; Krimpenfort, P.; Borst, P. Increased sensitivity to anticancer drugs and decreased inflammatory response in mice lacking the multidrug resistance-associated protein. *Nature Medicine* **1997**, *3*, 1275–1279.
- (15) Wu, G.; Fang, Y.-Z.; Yang, S.; Lupton, J. R.; Turner, N. D. Glutathione Metabolism and Its Implications for Health. *The Journal of Nutrition* **2004**, *134*, 489–492.
- (16) Nickerson, W. J.; Falcone, G.; Strauss, G. Studies of Quinone-Thioethers. I. Mechanism of Formation and Properties of Thiodione*. *Biochemistry* **1963**, *2*, 537–543.
- (17) Delalande, O.; Desvaux, H.; Godat, E.; Valleix, A.; Junot, C.; Labarre, J.; Boulard, Y. Cadmium—glutathione solution structures provide new insights into heavy metal detoxification. *The FEBS Journal* **2010**, *277*, 5086–5096.
- (18) Cole, S. P. C.; Deeley, R. G. Transport of glutathione and glutathione conjugates by MRP1. *Trends in Pharmacological Sciences* **2006**, *27*, 438–446.
- (19) Sauerbrey, A.; Voigt, A.; Wittig, S.; Häfer, R.; Zintl, F. Messenger RNA Analysis of the Multidrug Resistance Related Protein (MRP1) and the Lung Resistance Protein (LRP) in de novo and Relapsed Childhood Acute Lymphoblastic Leukemia. *Leukemia & Lymphoma* **2002**, *43*, 875–879.
- (20) Plasschaert, S. L. A.; de Bont, E. S. J. M.; Boezen, M.; vander Kolk, D. M.; Daenen, S. M. J. G.; Faber, K. N.; Kamps, W. A.; de Vries, E. G. E.; Vellenga, E. Expression of Multidrug Resistance-Associated Proteins Predicts Prognosis in Childhood and Adult Acute Lymphoblastic Leukemia. *Clinical Cancer Research* **2005**, *11*, 8661–8668.

- (21) Kourti, M.; Vavatsi, N.; Gombakis, N.; Sidi, V.; Tzimagiorgis, G.; Papageorgiou, T.; Koliousskas, D.; Athanassiadou, F. Expression of Multidrug Resistance 1 (MDR1), Multidrug Resistance-Related Protein 1 (MRP1), Lung Resistance Protein (LRP), and Breast Cancer Resistance Protein (BCRP) Genes and Clinical Outcome in Childhood Acute Lymphoblastic Leukemia. *International Journal of Hematology* **2007**, *86*, 166–173.
- (22) Gurbuxani, S.; Singh Arya, L.; Raina, V.; Sazawal, S.; Khattar, A.; Magrath, I.; Marie, J.-P.; Bhargava, M. Significance of MDR1, MRP1, GST π and GST μ mRNA expression in acute lymphoblastic leukemia in Indian patients. *Cancer Letters* **2001**, *167*, 73–83.
- (23) Simpson, R. J. Disruption of Cultured Cells by Nitrogen Cavitation. *Cold Spring Harbor Protocols* **2010**, -, pdb-prot5513.
- (24) Doige, C. A.; Sharom, F. J. Transport properties of P-glycoprotein in plasma membrane vesicles from multidrug-resistant Chinese hamster ovary cells. *Biochimica et Biophysica Acta (BBA) - Biomembranes* **1992**, *1109*, 161–171.
- (25) Cornwell, M. M.; Gottesman, M. M.; Pastan, I. H. Increased vinblastine binding to membrane vesicles from multidrug-resistant KB cells. *Journal of Biological Chemistry* **1986**, *261*, 7921–7928.
- (26) Leslie, E. M.; Deeley, R. G.; Cole, S. P. C. Multidrug resistance proteins: role of P-glycoprotein, MRP1, MRP2, and BCRP (ABCG2) in tissue defense. *Toxicology and Applied Pharmacology* **2005**, *204*, 216–237.
- (27) Deeley, R. G.; Cole, S. P. C. Substrate recognition and transport by multidrug resistance protein 1 (ABCC1). *FEBS Letters* **2006**, *580*, 1103–1111.
- (28) Evers, R.; Cnubben, N. H. P.; Wijnholds, J.; van Deemter, L.; van Bladeren, P. J.; Borst, P. Transport of glutathione prostaglandin A conjugates by the multidrug resistance protein 1. *FEBS Letters* **1997**, *419*, 112–116.
- (29) Müller, M.; Meijer, C.; Zaman, G. J.; Borst, P.; Scheper, R. J.; Mulder, N. H.; de Vries, E. G.; Jansen, P. L. Overexpression of the gene encoding the multidrug resistance-associated protein results in increased ATP-dependent glutathione S-conjugate transport. *Proceedings of the National Academy of Sciences of the United States of America* **1994**, *91*, 13033–13037.
- (30) Jedlitschky, G.; Leier, I.; Buchholz, U.; Center, M.; Keppler, D. ATP-dependent Transport of Glutathione S-Conjugates by the Multidrug Resistance-associated Protein. *Cancer Research* **1994**, *54*, 4833–4836.

- (31) Leier, I.; Jedlitschky, G.; Buchholz, U.; Cole, S. P.; Deeley, R. G.; Keppler, D. The MRP gene encodes an ATP-dependent export pump for leukotriene C₄ and structurally related conjugates. *Journal of Biological Chemistry* **1994**, *269*, 27807–27810.
- (32) Loe, D. W.; Almquist, K. C.; Deeley, R. G.; Cole, S. P. C. Multidrug Resistance Protein (MRP)-mediated Transport of Leukotriene C and Chemotherapeutic Agents in Membrane Vesicles: DEMONSTRATION OF GLUTATHIONE-DEPENDENT VINCRISTINE TRANSPORT. *Journal of Biological Chemistry* **1996**, *271*, 9675–9682.
- (33) Loe, D. W.; Deeley, R. G.; Cole, S. P. C. Verapamil stimulates glutathione transport by the 190-kDa multidrug resistance protein 1 (MRP1). *Journal of Pharmacology and Experimental Therapeutics* **2000**, *293*, 530–538.
- (34) Trompier, D.; Chang, X.-B.; Barattin, R.; D'Hardemare, A. d. M.; Di Pietro, A.; Baubichon-Cortay, H. Verapamil and Its Derivative Trigger Apoptosis through Glutathione Extrusion by Multidrug Resistance Protein MRP1. *Cancer Research* **2004**, *64*, 4950 LP –4956.
- (35) Létourneau, I. J.; Slot, A. J.; Deeley, R. G.; Cole, S. P. C. Mutational analysis of a highly conserved proline residue in MRP1, MRP2, and MRP3 reveals a partially conserved function. *Drug Metabolism and Disposition* **2007**, *35*, 1372–1379.
- (36) Jedlitschky, G.; Leier, I.; Buchholz, U.; Barnouin, K.; Kurz, G.; Keppler, D. Transport of Glutathione, Glucuronate, and Sulfate Conjugates by the MRP Gene-encoded Conjugate Export Pump. *Cancer Research* **1996**, *56*, 988–994.
- (37) Qian, Y.-M.; Grant, C. E.; Westlake, C. J.; Zhang, D.-W.; Lander, P. A.; Shepard, R. L.; Dantzig, A. H.; Cole, S. P. C.; Deeley, R. G. Photolabeling of human and murine multidrug resistance protein 1 with the high affinity inhibitor [125I]LY475776 and azidophenacyl-[35S]glutathione. *The Journal of Biological Chemistry* **2002**, *277*, 35225–31.
- (38) Leier, I.; Jedlitschky, G.; Buchholz, U.; Center, M.; Cole, S. P. C.; Deeley, R. G.; Keppler, D. ATP-dependent glutathione disulphide transport mediated by the MRP gene-encoded conjugate export pump. *Biochemical Journal* **1996**, *314*, 433 LP –437.
- (39) Norman, B. H.; Lander, P. A.; Gruber, J. M.; Kroin, J. S.; Cohen, J. D.; Jungheim, L. N.; Starling, J. J.; Law, K. L.; Self, T. D.; Tabas, L. B.; Williams, D. C.; Paul, D. C.; Dantzig, A. H. Cyclohexyl-linked tricyclic isoxazoles are potent and selective modulators of the multidrug resistance protein (MRP1). *Bioorganic & Medicinal Chemistry Letters* **2005**, *15*, 5526–5530.

- (40) Norman, B. H.; Gruber, J. M.; Hollinshead, S. P.; Wilson, J. W.; Starling, J. J.; Law, K. L.; Self, T. D.; Tabas, L. B.; Williams, D. C.; Paul, D. C.; Wagner, M. M.; Dantzig, A. H. Tricyclic isoxazoles are novel inhibitors of the multidrug resistance protein (MRP1). *Bioorganic & Medicinal Chemistry Letters* **2002**, *12*, 883–886.
- (41) Mao, Q.; Qiu, W.; Weigl, K. E.; Lander, P. A.; Tabas, L. B.; Shepard, R. L.; Dantzig, A. H.; Deeley, R. G.; Cole, S. P. C. GSH-dependent Photolabeling of Multidrug Resistance Protein MRP1 (ABCC1) by [125I]LY475776. *Journal of Biological Chemistry* **2002**, *277*, 28690–28699.
- (42) Jones, T. R.; Zamboni, R.; Belley, M.; Champion, E.; Charette, L.; Ford-Hutchinson, A. W.; Frenette, R.; Gauthier, J. Y.; Leger, S.; Masson, P.; . Pharmacology of L-660,711 (MK-571): a novel potent and selective leukotriene D4 receptor antagonist. *Canadian Journal of Physiology and Pharmacology* **1989**, *67*, 17–28.
- (43) Manning, P. J.; Watson, R. M.; Margolskee, D. J.; Williams, V. C.; Schwartz, J. I.; O’byrne, P. M. Inhibition of exercise-induced bronchoconstriction by MK-571, a potent leukotriene D4–receptor antagonist. *New England Journal of Medicine* **1990**, *323*, 1736–1739.
- (44) Kips, J. C.; Joos, G. F.; De Lepeleire, I.; Margolskee, D. J.; Buntinx, A.; Pauwels, R. A.; Van Der Straeten, M. E. MK-571, a Potent Antagonist of Leukotriene D4-induced Bronchoconstriction in the Human. *American Review of Respiratory Disease* **1991**, *144*, 617–621.
- (45) Letschert, K.; Komatsu, M.; Hummel-Eisenbeiss, J.; Keppler, D. Vectorial Transport of the Peptide CCK-8 by Double-Transfected MDCKII Cells Stably Expressing the Organic Anion Transporter OATP1B3 (OATP8) and the Export Pump ABCC2. *Journal of Pharmacology and Experimental Therapeutics* **2005**, *313*, 549 LP –556.
- (46) Büchler, M.; König, J.; Brom, M.; Kartenbeck, J.; Spring, H.; Horie, T.; Keppler, D. cDNA Cloning of the Hepatocyte Canalicular Isoform of the Multidrug Resistance Protein, cMrp, Reveals a Novel Conjugate Export Pump Deficient in Hyperbilirubinemic Mutant Rats. *Journal of Biological Chemistry* **1996**, *271*, 15091–15098.
- (47) Rius, M.; Nies, A. T.; Hummel-Eisenbeiss, J.; Jedlitschky, G.; Keppler, D. Cotransport of reduced glutathione with bile salts by MRP4 (ABCC4) localized to the basolateral hepatocyte membrane. *Hepatology* **2003**, *38*, 374–384.
- (48) Gekeler, V.; Ise, W.; Sanders, K.; Ulrich, W.; Beck, J. The Leukotriene LTD4 Receptor Antagonist Mk571 Specifically Modulates MRP Associated Multidrug Resistance. *Biochemical and Biophysical Research Communications* **1995**, *208*, 345–352.

- (49) Holló, Z.; Homolya, L.; Davis, C.; Sarkadi, B. Calcein accumulation as a fluorometric functional assay of the multidrug transporter. *Biochimica et Biophysica Acta (BBA) - Biomembranes* **1994**, *1191*, 384–388.
- (50) Dogan, A. L.; Legrand, O.; Faussat, A.-M.; Perrot, J.-Y.; Marie, J.-P. Evaluation and comparison of MRP1 activity with three fluorescent dyes and three modulators in leukemic cell lines. *Leukemia Research* **2004**, *28*, 619–622.
- (51) Strouse, J. J.; Ivnitski-Steele, I.; Waller, A.; Young, S. M.; Perez, D.; Evangelisti, A. M.; Ursu, O.; Bologa, C. G.; Carter, M. B.; Salas, V. M.; Tegos, G.; Larson, R. S.; Oprea, T. I.; Edwards, B. S.; Sklar, L. A. Fluorescent substrates for flow cytometric evaluation of efflux inhibition in ABCB1, ABCC1, and ABCG2 transporters. *Analytical Biochemistry* **2013**, *437*, 77–87.
- (52) Grech, K. V.; Davey, R. A.; Davey, M. W. The Relationship Between Modulation of MDR and Glutathione in MRP-Overexpressing Human Leukemia Cells. *Biochemical Pharmacology* **1998**, *55*, 1283–1289.
- (53) Cole, S. P. C. Patterns of cross-resistance in a multidrug-resistant small-cell lung carcinoma cell line. *Cancer Chemotherapy and Pharmacology* **1990**, *26*, 250–256.
- (54) Stride, B. D.; Valdimarsson, G.; Gerlach, J. H.; Wilson, G. M.; Cole, S. P.; Deeley, R. G. Structure and expression of the messenger RNA encoding the murine multidrug resistance protein, an ATP-binding cassette transporter. *Molecular Pharmacology* **1996**, *49*, 962 LP –971.
- (55) Lorico, A.; Rappa, G.; Finch, R. A.; Yang, D.; Flavell, R. A.; Sartorelli, A. C. Disruption of the murine MRP (multidrug resistance protein) gene leads to increased sensitivity to etoposide (VP-16) and increased levels of glutathione. *Cancer Research* **1997**, *57*, 5238–5242.
- (56) Souslova, T.; Averill-Bates, D. A. Multidrug-resistant hela cells overexpressing MRP1 exhibit sensitivity to cell killing by hyperthermia: Interactions with etoposide. *International Journal of Radiation Oncology Biology Physics* **2004**, *60*, 1538–1551.
- (57) Davey, R. A.; Longhurst, T. J.; Davey, M. W.; Belov, L.; Harvie, R. M.; Hancox, D.; Wheeler, H. Drug resistance mechanisms and MRP expression in response to epirubicin treatment in a human leukaemia cell line. *Leukemia Research* **1995**, *19*, 275–282.
- (58) Cullen, K. V.; Davey, R. A.; Davey, M. W.; Cullen, K. V.; Davey, R. A.; Davey, M. W. Verapamil-stimulated glutathione transport by the multidrug resistance-associated protein (MRP1) in leukaemia cells. Drug resistance does not correlate with resistance to Fas-mediated apoptosis. *Biochemical Pharmacology* **2001**, *62*, 417–424.

- (59) Polimeni, M.; Voena, C.; Kopecka, J.; Riganti, C.; Pescarmona, G.; Bosia, A.; Ghigo, D. Modulation of doxorubicin resistance by the glucose-6-phosphate dehydrogenase activity. *Biochemical Journal* **2011**, *439*, 141 LP –149.
- (60) Loe, D. W.; Deeley, R. G.; Cole, S. P. C. Characterization of Vincristine Transport by the Mr 190,000 Multidrug Resistance Protein (MRP): Evidence for Cotransport with Reduced Glutathione. *Cancer Research* **1998**, *4*, 5130–5136.
- (61) Leslie, E. M.; Deeley, R. G.; Cole, S. P. C. Bioflavonoid Stimulation of Glutathione Transport by the 190-kDa Multidrug Resistance Protein 1 (MRP1). *Drug Metabolism and Disposition* **2003**, *31*, 11–15.
- (62) Zaman, G. J.; Lankelma, J.; van Tellingen, O.; Beijnen, J.; Dekker, H.; Paulusma, C.; Oude Elferink, R. P.; Baas, F.; Borst, P. Role of glutathione in the export of compounds from cells by the multidrug-resistance-associated protein. *Proceedings of the National Academy of Sciences of the United States of America* **1995**, *92*, 7690 LP –7694.
- (63) Polcari, D.; Dauphin-Ducharme, P.; Mauzeroll, J. Scanning electrochemical microscopy: a comprehensive review of experimental parameters from 1989 to 2015. *Chemical Reviews* **2016**, *116*, 13234–13278.
- (64) Bard, A. J.; Fan, F. R. F.; Kwak, J.; Lev, O. Scanning Electrochemical Microscopy. Introduction and Principles. *Analytical Chemistry* **1989**, *61*, 132–138.
- (65) Engstrom, R. C.; Pharr, C. M. Scanning electrochemical microscopy. *Analytical Chemistry* **1989**, *61*, 1099A–1104A.
- (66) Bard, A. J.; Faulkner, L. R., *Electrochemical methods : fundamentals and applications*, 2nd ed.; Wiley: New York, 2001.
- (67) Bauermann, L. P.; Schuhmann, W.; Schulte, A. An advanced biological scanning electrochemical microscope (Bio-SECM) for studying individual living cells. *Physical Chemistry Chemical Physics* **2004**, *6*, 4003–4008.
- (68) Zhao, G.; Giolando, D. M.; Kirchoff, J. R. Chemical vapor deposition fabrication and characterization of silica-coated carbon fiber ultramicroelectrodes. *Analytical Chemistry* **1995**, *67*, 2592–2598.
- (69) Fang, Y.; Leddy, J. Cyclic voltammetric responses for inlaid microdisks with shields of thickness comparable to the electrode radius: a simulation of reversible electrode kinetics. *Analytical Chemistry* **1995**, *67*, 1259–1270.

- (70) Lefrou, C.; Renaud, C. Analytical Expressions for Quantitative Scanning Electrochemical Microscopy (SECM). *ChemPhysChem* **2010**, *11*, 547–556.
- (71) Lefrou, C. A unified new analytical approximation for positive feedback currents with a microdisk SECM tip. *Journal of Electroanalytical Chemistry* **2006**, *592*, 103–112.
- (72) Cornut, R.; Lefrou, C. A unified new analytical approximation for negative feedback currents with a microdisk SECM tip. *Journal of Electroanalytical Chemistry* **2007**, *608*, 59–66.
- (73) Cornut, R.; Lefrou, C. New analytical approximation of feedback approach curves with a microdisk SECM tip and irreversible kinetic reaction at the substrate. *Journal of Electroanalytical Chemistry* **2008**, *621*, 178–184.
- (74) Nogala, W.; Szot, K.; Burchardt, M.; Roelfs, F.; Rogalski, J.; Opallo, M.; Wittstock, G. Feedback mode SECM study of laccase and bilirubin oxidase immobilised in a sol-gel processed silicate film. *Analyst* **2010**, *135*, 2051–2058.
- (75) Tefashe, U. M.; Loewenstein, T.; Miura, H.; Schlettwein, D.; Wittstock, G. Scanning electrochemical microscope studies of dye regeneration in indoline (D149)-sensitized ZnO photoelectrochemical cells. *Journal of Electroanalytical Chemistry* **2010**, *650*, 24–30.
- (76) Fish, J.; Belytschko, T., *A First Course in Finite Elements*; Wiley Online Books; John Wiley & Sons, Ltd: 2007.
- (77) Nann, T.; Heinze, J. Simulation in electrochemistry using the finite element method: Part 1: The algorithm. *Electrochemistry Communications* **1999**, *1*, 289–294.
- (78) Mauzeroll, J.; Bard, A. J. Scanning electrochemical microscopy of menadione-glutathione conjugate export from yeast cells. *Proceedings of the National Academy of Sciences of the United States of America* **2004**, *101*, 7862–7867.
- (79) Mauzeroll, J.; Bard, A. J.; Owhadian, O.; Monks, T. J. Menadione metabolism to thiodione in hepatoblastoma by scanning electrochemical microscopy. *Proceedings of the National Academy of Sciences of the United States of America* **2004**, *101*, 17582–17587.
- (80) Koley, D.; Bard, A. J. Inhibition of the MRP1-mediated transport of the menadione-glutathione conjugate (thiodione) in HeLa cells as studied by SECM. *Proceedings of the National Academy of Sciences of the United States of America* **2012**, *109*, 11522–11527.

- (81) Liu, B.; Rotenberg, S. A.; Mirkin, M. V. Scanning electrochemical microscopy of living cells: Different redox activities of nonmetastatic and metastatic human breast cells. *Proceedings of the National Academy of Sciences of the United States of America* **2000**, *97*, 9855 LP –9860.
- (82) Gonsalves, M.; Barker, A. L.; Macpherson, J. V.; Unwin, P. R.; O'Hare, D.; Winlove, C. P. Scanning Electrochemical Microscopy as a Local Probe of Oxygen Permeability in Cartilage. *Biophysical Journal* **2000**, *78*, 1578–1588.
- (83) Li, M. S. M.; Filice, F. P.; Ding, Z. A time course study of cadmium effect on membrane permeability of single human bladder cancer cells using scanning electrochemical microscopy. *Journal of Inorganic Biochemistry* **2014**, *136*, 177–183.
- (84) Zhang, M.-N.; Ding, Z.; Long, Y.-T. Sensing cisplatin-induced permeation of single live human bladder cancer cells by scanning electrochemical microscopy. *Analyst* **2015**, *140*, 6054–6060.
- (85) Filice, F. P.; Li, M. S. M.; Henderson, J. D.; Ding, Z. Mapping Cd²⁺-induced membrane permeability changes of single live cells by means of scanning electrochemical microscopy. *Analytica Chimica Acta* **2016**, *908*, 85–94.
- (86) Li, M. S. M.; Filice, F. P.; Henderson, J. D.; Ding, Z. Probing Cd²⁺-Stressed Live Cell Membrane Permeability with Various Redox Mediators in Scanning Electrochemical Microscopy. *The Journal of Physical Chemistry C* **2016**, *120*, 6094–6103.
- (87) Henderson, J. D.; Filice, F. P.; Li, M. S. M.; Ding, Z. Tracking Live-Cell Response to Hexavalent Chromium Toxicity by using Scanning Electrochemical Microscopy. *ChemElectroChem* **2017**, *4*, 856–863.
- (88) Wring, S. A.; Hart, J. P.; Birch, B. J. Voltammetric behaviour of screen-printed carbon electrodes, chemically modified with selected mediators, and their application as sensors for the determination of reduced glutathione. *Analyst* **1991**, *116*, 123–129.
- (89) Schreyer, S. K.; Mikkelsen, S. R. A Synthetic Cysteine Oxidase Based on a Ferrocene-Cyclodextrin Conjugate. *Bioconjugate Chemistry* **1999**, *10*, 464–469.
- (90) Kuss, S.; Cornut, R.; Beaulieu, I.; Mezour, M. A.; Annabi, B.; Mauzeroll, J. Assessing multidrug resistance protein 1-mediated function in cancer cell multidrug resistance by scanning electrochemical microscopy and flow cytometry. *Bioelectrochemistry* **2011**, *82*, 29–37.
- (91) Kuss, S.; Polcari, D.; Geissler, M.; Brassard, D.; Mauzeroll, J. Assessment of multidrug resistance on cell coculture patterns using scanning electrochemical microscopy. *Proceedings of the National Academy of Sciences of the United States of America* **2013**, *110*, 9249–9254.

- (92) Polcari, D.; Hernández-Castro, J. A.; Li, K.; Geissler, M.; Mauzeroll, J. Determination of the Relationship between Expression and Functional Activity of Multidrug Resistance-Associated Protein 1 using Scanning Electrochemical Microscopy. *Analytical Chemistry* **2017**, *89*, 8988–8994.
- (93) Myette, R. L.; Conseil, G.; Ebert, S. P.; Wetzel, B.; Detty, M. R.; Cole, S. P. C. Chalcogenopyrylium Dyes as Differential Modulators of Organic Anion Transport by Multidrug Resistance Protein 1 (MRP1), MRP2, and MRP4. *Drug Metabolism and Disposition* **2013**, *41*, 1231 LP –1239.
- (94) Beaulieu, I.; Geissler, M.; Mauzeroll, J. Oxygen Plasma Treatment of Polystyrene and Zeonor: Substrates for Adhesion of Patterned Cells. *Langmuir* **2009**, *25*, 7169–7176.
- (95) Cornut, R.; Griveau, S.; Lefrou, C. Accuracy study on fitting procedure of kinetics SECM feedback experiments. *Journal of Electroanalytical Chemistry* **2010**, *650*, 55–61.
- (96) Ballesteros Katemann, B.; Schulte, A.; Schuhmann, W. Constant-Distance Mode Scanning Electrochemical Microscopy (SECM)—Part I: Adaptation of a Non-Optical Shear-Force-Based Positioning Mode for SECM Tips. *Chemistry – A European Journal* **2003**, *9*, 2025–2033.
- (97) Takahashi, Y.; Shiku, H.; Murata, T.; Yasukawa, T.; Matsue, T. Transfected Single-Cell Imaging by Scanning Electrochemical Optical Microscopy with Shear Force Feedback Regulation. *Analytical Chemistry* **2009**, *81*, 9674–9681.
- (98) Lee, Y.; Ding, Z.; Bard, A. J. Combined Scanning Electrochemical/Optical Microscopy with Shear Force and Current Feedback. *Analytical Chemistry* **2002**, *74*, 3634–3643.
- (99) Alpuche-Aviles, M. A.; Wipf, D. O. Impedance Feedback Control for Scanning Electrochemical Microscopy. *Analytical Chemistry* **2001**, *73*, 4873–4881.
- (100) Gabrielli, C.; Huet, F.; Keddam, M.; Rousseau, P.; Vivier, V. Scanning Electrochemical Microscopy Imaging by Means of High-Frequency Impedance Measurements in Feedback Mode. *The Journal of Physical Chemistry B* **2004**, *108*, 11620–11626.
- (101) Etienne, M.; Schulte, A.; Schuhmann, W. High resolution constant-distance mode alternating current scanning electrochemical microscopy (AC-SECM). *Electrochemistry Communications* **2004**, *6*, 288–293.
- (102) Diakowski, P. M.; Baranski, A. S. Positive and negative AC impedance feedback observed above conductive substrates under SECM conditions. *Electrochimica Acta* **2006**, *52*, 854–862.

- (103) McKelvey, K.; Edwards, M. A.; Unwin, P. R. Intermittent Contact-Scanning Electrochemical Microscopy (IC-SECM): A New Approach for Tip Positioning and Simultaneous Imaging of Interfacial Topography and Activity. *Analytical Chemistry* **2010**, *82*, 6334–6337.
- (104) Macpherson, J. V.; Unwin, P. R. Combined Scanning Electrochemical-Atomic Force Microscopy. *Analytical Chemistry* **2000**, *72*, 276–285.
- (105) Kueng, A.; Kranz, C.; Lugstein, A.; Bertagnolli, E.; Mizaikoff, B. Integrated AFM-SECM in Tapping Mode: Simultaneous Topographical and Electrochemical Imaging of Enzyme Activity. *Angewandte Chemie International Edition* **2003**, *42*, 3238–3240.
- (106) Macpherson, J. V.; Unwin, P. R. Noncontact Electrochemical Imaging with Combined Scanning Electrochemical Atomic Force Microscopy. *Analytical Chemistry* **2001**, *73*, 550–557.
- (107) Lhenry, S.; Leroux, Y. R.; Hapiot, P. Chemically Irreversible Redox Mediator for SECM Kinetics Investigations: Determination of the Absolute Tip–Sample Distance. *Analytical Chemistry* **2013**, *85*, 1840–1845.
- (108) Li, M. S. M.; Filice, F. P.; Ding, Z. Determining live cell topography by scanning electrochemical microscopy. *Journal of Electroanalytical Chemistry* **2016**, *779*, 176–186.
- (109) Cornut, R.; Mayoral, M.; Fabre, D.; Mauzeroll, J. Scanning Electrochemical Microscopy Approach Curves for Ring Microelectrodes in Pure Negative and Positive Feedback Mode. *Journal of the Electrochemical Society* **2010**, *157*, F77–F82.
- (110) Cornut, R.; Hapiot, P.; Lefrou, C. Enzyme-mediator kinetics studies with SECM: Numerical results and procedures to determine kinetics constants. *Journal of Electroanalytical Chemistry* **2009**, *633*, 221–227.
- (111) Cornut, R.; Lefrou, C. Studying permeable films with scanning electrochemical microscopy (SECM): Quantitative determination of permeability parameter. *Journal of Electroanalytical Chemistry* **2008**, *623*, 197–203.
- (112) Kuss, C.; Payne, N. A.; Mauzeroll, J. Probing Passivating Porous Films by Scanning Electrochemical Microscopy. *Journal of The Electrochemical Society* **2016**, *163*, H3066–H3071.
- (113) Anicet, N.; Bourdillon, C.; Moiroux, J.; Savéant, J.-M. Electron Transfer in Organized Assemblies of Biomolecules. Step-by-Step Avidin/Biotin Construction and Dynamic Characteristics of a Spatially Ordered Multilayer Enzyme Electrode. *The Journal of Physical Chemistry B* **1998**, *102*, 9844–9849.

- (114) Gateman, S. M.; Stephens, L. I.; Perry, S. C.; Lacasse, R.; Schulz, R.; Mauzeroll, J. The role of titanium in the initiation of localized corrosion of stainless steel 444. *npj Materials Degradation* **2018**, *2*, 5.
- (115) Kurien, B. T.; Scofield, R. H. Western blotting. *Methods* **2006**, *38*, 283–293.
- (116) Towbin, H.; Staehelin, T.; Gordon, J. Electrophoretic transfer of proteins from polyacrylamide gels to nitrocellulose sheets: procedure and some applications. *Proceedings of the National Academy of Sciences of the United States of America* **1979**, *76*, 4350 LP–4354.
- (117) Tietze, F. Enzymic method for quantitative determination of nanogram amounts of total and oxidized glutathione: Applications to mammalian blood and other tissues. *Analytical Biochemistry* **1969**, *27*, 502–522.
- (118) Tipple, T. E.; Rogers, L. K. In *Methods in Molecular Biology (Methods and Protocols)*, Harris, C., Hansen, J. M., Eds.; Humana Press: Totowa, NJ, 2012, pp 315–324.
- (119) Rahman, I.; Kode, A.; Biswas, S. K. Assay for quantitative determination of glutathione and glutathione disulfide levels using enzymatic recycling method. *Nature Protocols* **2007**, *1*, 3159.
- (120) Smith, P. K.; Krohn, R. I.; Hermanson, G. T.; Mallia, A. K.; Gartner, F. H.; Provenzano, M. D.; Fujimoto, E. K.; Goeke, N. M.; Olson, B. J.; Klenk, D. C. Measurement of protein using bicinchoninic acid. *Analytical Biochemistry* **1985**, *150*, 76–85.
- (121) Bradford, M. M. A rapid and sensitive method for the quantitation of microgram quantities of protein utilizing the principle of protein-dye binding. *Analytical Biochemistry* **1976**, *72*, 248–254.
- (122) Read, S. M.; Northcote, D. H. Minimization of variation in the response to different proteins of the Coomassie blue G dye-binding assay for protein. *Analytical Biochemistry* **1981**, *116*, 53–64.
- (123) Stoscheck, C. M. Increased uniformity in the response of the Coomassie blue G protein assay to different proteins. *Analytical Biochemistry* **1990**, *184*, 111–116.
- (124) Fountoulakis, M.; Juranville, J.-F.; Manneberg, M. Comparison of the Coomassie brilliant blue, bicinchoninic acid and Lowry quantitation assays, using non-glycosylated and glycosylated proteins. *Journal of Biochemical and Biophysical Methods* **1992**, *24*, 265–274.
- (125) Calhoun, R. L.; Bard, A. J. Study of the Catalytic Following Reaction by Scanning Electrochemical Microscopy (SECM). *Journal of The Electrochemical Society* **2012**, *159*, F42–F47.

- (126) Cannan, S.; Cervera, J.; Steliaros (née Haskins), R. J.; Bitziou, E.; Whitworth, A. L.; Unwin, P. R. Scanning electrochemical microscopy (SECM) studies of catalytic EC' processes: theory and experiment for feedback, generation/collection and imaging measurements. *Physical Chemistry Chemical Physics* **2011**, *13*, 5403–5412.
- (127) Stephens, L. I.; Payne, N. A.; Skaanvik, S. A.; Polcari, D.; Geissler, M.; Mauzeroll, J. Evaluating the Use of Edge Detection in Extracting Feature Size from Scanning Electrochemical Microscopy Images. *Analytical Chemistry* **2019**, *91*, 3944–3950.
- (128) Liu, B.; Bard, A. J.; Mirkin, M. V.; Creager, S. E. Electron Transfer at Self-Assembled Monolayers Measured by Scanning Electrochemical Microscopy. *Journal of the American Chemical Society* **2004**, *126*, 1485–1492.
- (129) Oleinick, A. I.; Battistel, D.; Daniele, S.; Svir, I.; Amatore, C. Simple and Clear Evidence for Positive Feedback Limitation by Bipolar Behavior during Scanning Electrochemical Microscopy of Unbiased Conductors. *Analytical Chemistry* **2011**, *83*, 4887–4893.
- (130) Mosadegh, B.; Agarwal, M.; Torisawa, Y.-s.; Takayama, S. Simultaneous fabrication of PDMS through-holes for three-dimensional microfluidic applications. *Lab on a Chip* **2010**, *10*, 1983–1986.
- (131) PROCEEDINGS OF THE PHYSIOLOGICAL SOCIETY: January 22, 1910. *The Journal of Physiology* **1910**, *40*, i–vii.
- (132) Neubig, R. R.; Spedding, M.; Kenakin, T.; Christopoulos, A. International Union of Pharmacology Committee on Receptor Nomenclature and Drug Classification. XXXVIII. Update on Terms and Symbols in Quantitative Pharmacology. *Pharmacological Reviews* **2003**, *55*, 597 LP –606.
- (133) Harfield, J. C.; Batchelor-McAuley, C.; Compton, R. G. Electrochemical determination of glutathione: a review. *Analyst* **2012**, *137*, 2285–2296.
- (134) Hugo Seymour, E.; Wilkins, S. J.; Lawrence, N. S.; Compton, R. G. ELECTROCHEMICAL DETECTION OF GLUTATHIONE: AN ELECTROCHEMICALLY INITIATED REACTION PATHWAY. *Analytical Letters* **2002**, *35*, 1387–1399.
- (135) Lawrence, N. S.; Davis, J.; Compton, R. G. Electrochemical detection of thiols in biological media. *Talanta* **2001**, *53*, 1089–1094.
- (136) Bănică, F. G.; Fogg, A. G.; Moreira, J. C. Catalytic cathodic stripping voltammetry at a hanging mercury drop electrode of glutathione in the presence of nickel ion. *Analyst* **1994**, *119*, 2343–2349.

- (137) Yang, C.-S.; Tsai, P.-J.; Chen, W.-Y.; Liu, L.; Kuo, J.-S. Determination of extracellular glutathione in livers of anaesthetized rats by microdialysis with on-line high-performance liquid chromatography. *Journal of Chromatography B: Biomedical Sciences and Applications* **1995**, *667*, 41–48.
- (138) Vandeberg, P. J.; Johnson, D. C. Pulsed electrochemical detection of cysteine, cystine, methionine, and glutathione at gold electrodes following their separation by liquid chromatography. *Analytical Chemistry* **1993**, *65*, 2713–2718.
- (139) Wring, S. A.; Hart, J. P.; Birch, B. J. Voltammetric behaviour of screen-printed carbon electrodes, chemically modified with selected mediators, and their application as sensors for the determination of reduced glutathione. *Analyst* **1991**, *116*, 123–129.
- (140) Raouf, J. B.; Ojani, R.; Karimi-Maleh, H. Electrocatalytic oxidation of glutathione at carbon paste electrode modified with 2,7-bis (ferrocenyl ethyl) fluoren-9-one: application as a voltammetric sensor. *Journal of Applied Electrochemistry* **2009**, *39*, 1169–1175.
- (141) Raouf, J.-B.; Ojani, R.; Baghayeri, M. Simultaneous electrochemical determination of glutathione and tryptophan on a nano-TiO₂/ferrocene carboxylic acid modified carbon paste electrode. *Sensors and Actuators B: Chemical* **2009**, *143*, 261–269.
- (142) Griveau, S.; Gulppi, M.; Pavez, J.; Zagal, J. H.; Bedioui, F. Cobalt Phthalocyanine-Based Molecular Materials for the Electrocatalysis and Electroanalysis of 2-Mercaptoethanol, 2-Mercaptoethanesulfonic Acid, Reduced Glutathione and L-Cysteine. *Electroanalysis* **2003**, *15*, 779–785.
- (143) Cornut, R.; Bhasin, A.; Lhenry, S.; Etienne, M.; Lefrou, C. Accurate and Simplified Consideration of the Probe Geometrical Defaults in Scanning Electrochemical Microscopy: Theoretical and Experimental Investigations. *Analytical Chemistry* **2011**, *83*, 9669–9675.
- (144) Zhu, R.; Qin, Z.; Noël, J. J.; Shoosmith, D. W.; Ding, Z. Analyzing the Influence of Alloying Elements and Impurities on the Localized Reactivity of Titanium Grade-7 by Scanning Electrochemical Microscopy. *Analytical Chemistry* **2008**, *80*, 1437–1447.